ION-IMPLANTED POLYANILINE THIN FILMS FOR RADIATION SENSING APPLICATIONS.

by

MATOME MALOBA

DISSERTATION

Submitted in accordance with the requirements for

the degree of

MASTER OF SCIENCE

in

PHYSICS

at the

UNIVERSITY OF SOUTH AFRICA

SUPERVISOR: PROF. S. J MOLOI

(University of South Africa)

CO-SUPERVISOR: PROF. M MSIMANGA

(Tshwane University of Technology)

(10 April 2019)

DECLARATON

Name and surname: Matome Maloba

Student number: 62231669

Degree: MSc Physics

ION-IMPLANTED POLYANILINE THIN FILMS FOR RADIATION SENSING APPLICATIONS.

I declare that the above dissertation is my own work and that all the sources that I have used or quoted have been indicated and acknowledged by means of complete references. I further declare that I submitted the dissertation to originality checking software and that it falls within the accepted requirements for originality. I further declare that I have not previously submitted this work, or part of it, for examination at UNISA for another qualification or at any other higher education institution.

10/04/2019

……..... ……..

SIGNATURE DATE

ACKNOWLEDGEMENT

- First and foremost, I would like to express my special thanks to Almighty God for His mercy, happy life He gave me and blessings He showered me with from the day I started with this work.
- I would like to express my deep and sincere gratitude to my supervisor, Prof. S. J. Moloi for giving me an opportunity to study and work under his guidance. His hard work, dedication, vision and humanity really inspires me a lot. I would also like to express my special gratitude to my co-supervisor, Prof. M. Msimanga from Tshwane University of Technology for believing in me since from my undergraduate studies at TUT. Thank you for your wisdom, knowledge sharing, mentorship and being patient with me throughout this work.
- I would like to thank UNISA's postgraduate students for helping me with some sample characterization techniques. Furthermore, I would like to thank all staff members at iThemba LABS, particularly Dr. M. Madhuku for helping me with RBS measurements and Mr. Tony Miller for implantation of the samples.
- All thanks to my family and friends for their support, prayers and their contribution towards the completion of this works. Special thanks to Masedi Masekane for helping me with RBS data analysis and Madimetja Masenya for your understanding, support and always ensuring that I met my deadlines.
- The financial assistance of the National Research Foundation (NRF) of South Africa (Grant Number: 105292) towards this research is hereby acknowledged. Opinions expressed and conclusions arrived at, are those of the authors and are not necessarily to be attributed to the NRF.

DEDICATION

This work is dedicated to my family and friends, my mother Anna Maselela Maloba, my father France Poopedi Maloba, my three brothers (Kenny, Masilo and Tshepang), my four sisters (Sebongile, Tebogo, Moloto and Mmamoyahabo) who contributed a lot towards the success of my work and the role they play in my life. I also like to dedicate this dissertation to Madimetja Betty Masenya for her support and for being there for me. In addition, this dissertation is also dedicated to the following late souls: Chrestina Monyemoratho, Richard Monyemoratho, Lina Maloba and Nelly Maloba; may their soul rest in eternal peace.

THANK YOU!!!!!

ABSTRACT

Polyaniline (PANI) thin films were prepared and deposited on an ITO/PET substrate using a spin coater. The prepared films were amorphous in nature, with nanoparticles that were spherical in shape. The size of the nanoparticles was varying from 7.0 to 269 nm with mean particle size of 194.4 nm. The films were then implanted at cryogenic temperature with 50-keV Cu^+ ions to different fluences of $0.5x10^{16}$, $1.0x10^{16}$, $3.0x10^{16}$ and $5.0x10^{16}$ ions/cm^2 to form Cu^+-PANI nanocomposite films. Different characterisation techniques were used to investigate a change in structural, optical and electrical properties of the films due to ion implantation. The results indicated that cryogenic implantation led to infinitesimally changes in the crystal structure of the implanted PANI films. Moreover, the optical band gap and the resistance of the films were found to decrease drastically at low fluence, followed by an infinitesimal decrease at high fluences. The results, in general, indicate that implantation by copper ions to high fluences can be used as an effective tool to tailor properties of the material so that it becomes resistant to change. This stability is suitable for the material to be used for fabrication of the current and future radiation sensors.

ACRONYMS

Ca	:	Circa (approximately)
CB	:	Conduction Band
cps	:	count per second
CPs	:	Conducting Polymers
Cu	:	Copper
EB	:	Emeraldine Base
EDX	:	Energy Dispersive X-ray
E_g	:	Energy Gap
eV	:	electron Volt
ES	:	Emeraldine Salt
F_g	:	Fermi level
FTIR	:	Fourier Transform Infrared Spectroscopy
HOMO	:	Highest Occupied Molecular Orbital
IR	:	Infrared
ITO	:	Indium Tin Oxide
I-V	:	Current-Voltage
LEB	:	Leucoemeraldine Base structure

LED	:	Light Emitting Diode
LUMO	:	Lowest Unoccupied Molecular Orbital
NPs	:	Nanoparticles
PANI	:	Polyaniline
PET	:	Polyethylene terephthalate
PL	:	Photoluminescence
MeV	:	Mega electron Volt
PNB	:	Permigraniline Base
RBS	:	Rutherford Backscattering Spectroscopy
rpm	:	revolution per minute
SEM	:	Scanning Electron Microscopy
SPR	:	Surface Plasmon Resonance
UV-Vis	:	Ultra Violet -Visible
VB	:	Valence Band
XRD	:	X-ray Diffraction

KEYWORDS

Polyaniline, Conducting polymers; Ion implantation; Structural properties; Optical Properties; Electrical Properties; Radiation Sensors.

TABLE OF CONTENTS

LIST OF TABLES

LIST OF FIGURES

CHAPTER 1: LITERATURE REVIEW

1.1. Introduction to radiation detectors

Ionizing radiation has sufficient energy to ionize matter that it interacts with and it cannot be sensed by the human body. Therefore, any excessive exposures to this type of radiation can result in serious health effects. To avoid excessive exposures, it is important to have radiation detection instruments in place to detect and measure the presence of such radiation. Radiation measuring instruments are utilized for a variety of applications in various fields such as nuclear industries and medical fields. For example, in nuclear industries, radiation detectors are mainly used to monitor and control exposures to acceptable levels, while in the medical field, such detectors are mainly used for radiation dose monitoring and imaging applications. The detectors are also used in high energy physics experiments to detect charged particles.

Three types of radiation detection instruments that are widely used are gas-filled radiation detectors, scintillation counters, and semiconductor detectors [1]. Comparing these radiation detectors in terms of their detection media, gas-field radiation detectors make use of a gas or mixture of gases to detect ionizing radiation, while scintillation counters make use of scintillator materials such as sodium iodide doped with thallium NaI(TI). Semiconductor detectors on the other hand, make use of semiconducting materials such as silicon and germanium as detection

media. However, sensing media used by these radiation detectors suffer several drawbacks. For example, when the gas used in gas-filled radiation detectors is contaminated, it tends to degrade the performance of the detector [2]. Scintillation counters mostly use NaI(Tl) and this material which is hygroscopic and may deteriorate due to water absorption if exposed to atmosphere for any length of time [3, 4]. Semiconductor materials are relatively expensive, brittle and are prone to radiation damage [5, 6]. It is therefore, important that suitable material is established/ identified for fabrication of stable and reliable radiation sensors.

1.2. Conducting polymers

Conducting polymers (CPs) are classified as a special class of organic materials with alternating single-double bond conjugation [7]. Examples of the well-known polymers are polythiophene, poly (triarylamine), polypyrrole, polyacetylene and polyaniline [8, 9, 10]. CPs offer special properties of special interest for radiation detection when compared to commonly used sensing media since they are environmentally inert, mechanically flexible and relatively cheap. CPs also have tunable electrical and optical properties [11, 12]. In nature, polymers are poor conductors and are not ordinarily being used for fabrication of electronic devices detectors. To modify their conductivity, polymers are infused with different materials such as ZnO, Bi_2O_3 and metal ions such as copper, silver and gold using various doping methods like in situ growth of nanoparticles (NPs) in a polymer matrix and ion implantation [13].

In situ growth of NPs is a technique whereby inorganic NPs such as metals (e.g. Al, Fe and Ag), metal oxides (ZnO) and non-metal oxides (Bi_2O_3) are incorporated into the polymer matrix [14]. However, the size to which the NPs grow is bit complicated and it is still a challenge to predict the size to which these NPs will grow after being incorporated. Moreover, it is difficult to produce

NPs having approximately the same size in the polymer matrix since the NPs agglomerate due to their specific surface area and volume effects. Therefore, metal-polymer nanocomposites having the same structure are difficult to reproduce with this technique [14]. For example, Intaniwet et al. [15] infused bismuth oxide (Bi_2O_3) NPs into poly(triarylamine) (PTAA) active layer through this technique, to increase the attenuation or the sensitivity of the polymer towards the detection of X-rays due to high-Z of bismuth (Bi). However, the Bi_2O_3 NPs were not uniformly distributed on the surface of the substrate and were agglomerated at the bottom of the polymer layer.

Ion implantation is an alternative doping technique that could overcome the above-mentioned problems. In this technique, a target in the form of a solid polymer is bombarded with an energetic beam of positively charged ions. When the ions interact with the target polymer, they get embedded inside the polymer matrix. As a result, defect levels, carbonization and carbon clusters are created, leading to an alteration of the structural, optical and electrical properties [16, 17]. This technique has unique advantages in that one can control the depth of doping by varying or selecting suitable energy and the dose of the implanting ions. If suitable dopants are selected the implanted polymer can retain its conductivity for a long period of time [16, 17, 18]. In addition, any element in the form of ions can be implanted into the polymer [19, 12].

However, fabrication-structure-property relationships of polymer-based detectors are not as well understood as for other detector types [16, 20]. In addition, the link between the induced defect levels and carbonization and carbon cluster have not been established nor fully understood. Realizing the full potential of these polymer-based detectors requires a deep understanding of the link between induced defect levels, carbonization and carbon clusters. Moreover, the key fabrication-structure-property relationships of the polymer material that yields the desired

properties for detector fabrication need to be identified and understood. The study and understanding of CPs is therefore of significant importance for plastic electronics, and this is a forefront research area where CPs have the potential to replace the present silicon-based technology. Thus, CPs are essential components of not just radiation detection and measurement, but also other applications in photonics, chemical/biosensors, light emitting diodes (LEDs), thin film transistors, corrosion resistance to name a few [21, 22].

1.3. Aim and objectives

1.3.1. Aim

- The aim of this study is to investigate the effects of ion implantation on structural, optical and electrical properties of polyaniline thin films for potential applications in radiation sensing. In achieving this aim, the set objectives involve preparation and characterization of PANI films using different techniques.

1.3.2. Objectives

Material Preparation and Characterization

A spin coater was used to prepare PANI thin films on ITO/PET substrates. The prepared PANI films were doped with Cu^{+} ions through ion implantation. Techniques that were used to characterize PANI films before and after ion implantation are as follows:

- Scanning Electron Microscopy (SEM),
- X-ray Diffraction (XRD),
- Rutherford Backscattering Spectroscopy (RBS),
- Fourier Transform Infrared Spectroscopy (FTIR),

- Raman Spectroscopy,
- UV-Visible spectroscopy (UV-Vis), and
- Photoluminescence spectroscopy (PL).

Device Fabrication and Characterization

Devices were fabricated on undoped-and metal-doped PANI films by using copper as electrodes. The fabricated devices were characterized by:

- Current-Voltage (I-V) technique at room temperature.

1.4. Thesis layout

- Chapter 2 gives an introduction of commonly used radiation detection instruments, polymer-based radiation detectors and overview of the family of conducting polymers. For this study, polyaniline was chosen as a polymer of interest since it possesses special properties of interest when compared to other conducting polymers. Chapter 2 further discusses different oxidation states, properties and various technological applications of polyaniline.
- In this study, polyaniline films were prepared and implanted to different fluences. Thereafter, different characterization techniques were used to investigate the effect of implantation on the properties of the films and chapter 3 gives full description of these experimental techniques.
- Chapter 4 gives a full description on how the polyaniline films were prepared and ion implanted. In chapter 5, all the obtained results are fully presented and discussed.
- Chapter 6 concludes the present study, and it also gives future plans for the study.

1.5. References

[1] Knoll G. F. 2000 *Radiation Detection and Measurement*, 3rd edition. (John Wiley & Sons, Inc.: New York).

[2] Ahmed S. N. 2007 *Physics and Engineering of Radiation Detection*, 1st edition. (Elsevier.: San Diego).

[3] James E. M. 2013 *Physics for Radiation Protection*, 3rd edition. (WILEY-VCH Verlag GmbH & Co. kGa.: Weinheim).

[4] Chen Q. *et al*. 2011 *Annu. Rep. Prog. Chem*. *Sect. C: Phys. Chem.* **107** 298.

[5] Rizzi M. *et al.* 2010 *J. Appl. Sci*. **10 (23)** 3141.

[6] Lutz G. 2007 *Semiconductor Radiation Detectors,* 2nd edition. (Springer Verlag Berlin Heidelberg.: New York).

[7] Molapo K. M. *et al*. 2012 *Int. J. Electrochem. Sci*. **7** 11859.

[8] Hall N. 2003 *Chem. Commun.* **7** 1.

[9] Gupta K. *et al.* 2010 *Synth. Met.* **160** 1566.

[10] Liu Z. *et al.* 2013 *Curr. Org. Chem.* **17 (20)** 2256.

[11] Farag A. M. and Rafea M. A. 2010 *Synth. Met*. **160** 156.

[12] Li B. *et al*. 2010 *J. Polym. Sci. Part B: Polym. Phys.* **48** 2072.

[13] Kango S. *et al*. 2013 *Review, Progress in Polymer Science* **38 (8)** 1232.

[14] Fusheng P. *et al*. 2010 *J. Membrane Sci.* **7** 171.

[15] Intaniwet A. *et al.* 2012 *Nanotechnology* **23** 235502.

[16] Townsend P. 2009 *Luminescence, ion implantation, and nanoparticles, in Ion Beams in Nanoscience and Technology*. (Springer Verlag Berlin Heidelberg.: New York).

[17] Nordlund K. *et al.* 2009 *Nanocluster and nanovoid formation by ion implantation, in Ion Beams in Nanoscience and Technology*. (Springer Verlag Berlin Heidelberg.: New York).

[18] Nakagawa S. and Ohta N. 2010 *Nucl. Instr. Meth. B* **268** 2467.

[19] Resta V. *et al.* 2014 *Nucl. Instr. Meth. B* **331** 168.

[20] Mutiso R. M. and Winey R. M. 2014 *Prog. Polym. Sci*. **40** 63.

[21] Ates M. *et al*. 2012 *Curr. Phys. Chem*. **2 (1)** 224.

[22] Kumar F. *et al*. 2010 *Synth. Met*. **160** 1507.

CHAPTER 2: THEORETICAL OVERVIEW

2.1. Introduction

A radiation detector is an instrument designed specifically to detect and measure ionizing radiation. As mentioned previously, there are three main types of radiation detectors that are commonly used [1], namely; gas-filled radiation detectors, scintillation counters and semiconductor detectors. These radiation detectors function similarly, i.e., they all count single photons or particles at a time. The difference lies in the design and principles of operation [1, 2]. There are two processes that take place when ionizing radiation interacts with a sensing material of the detector. Ionizing radiation can either ionize or excite the sensing medium. Ionization occurs when a neutral atom gains or loses one or more electron (s), whereas excitation occurs when an incident ionizing radiation quanta or particle is absorbed by the sensing medium, atoms of the sensing medium get excited, and when the atoms de-excite photons are emitted. Gas-filled and semiconductor radiation detectors are designed based on the ionization principle, whereas scintillation counters are designed based on the excitation principle.

A typical radiation detection instrument contains three basic components, a detector, amplifier and processor. The detector contains the sensing medium, which absorbs incident radiation energy and converts it into a signal. The amplifier and processor amplify the signal from the detector and measures the size and/or number of signals produced by the detector, respectively. The processor

may also translate the quantity measured into appropriate radiological units such as milli Sievert (mSv) [3, 4]. The aim of this chapter is to discuss types of radiation detectors and briefly discusses the disadvantages of the sensing media used by these radiation detection instruments. In addition, this chapter introduces polymer-based radiation detectors, and briefly discusses the proposed sensing material (i.e. CPs) used by these detectors.

2.2. Types of radiation detectors

2.2.1. Gas-filled radiation detectors

A gas-filled radiation detector uses gas or a mixture of gases as a detection medium. A typical gas-filled radiation detector consists of a closed vessel containing mixture of gases, as shown in Fig. 2.1. Incoming radiation interacts with the gas inside the vessel and creates ion pairs, and the created ion pairs render the gas to be electrically conductive [3]. When a voltage is applied across the electrodes, the created pairs are separated. Negatively charged ions and electrons are attracted to the positively charged anode, while positively charged ions move to the negatively charged cathode. When electrical charges are collected on the electrodes, a small current pulse is measured, amplified and displayed as a signal.

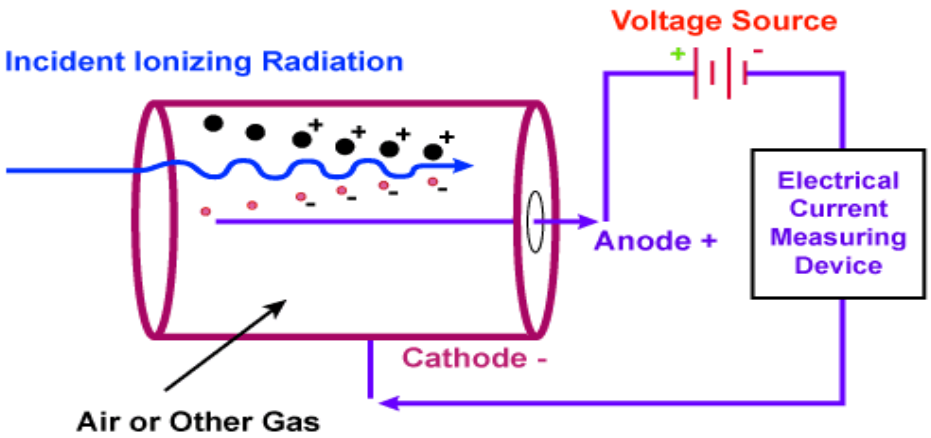

Figure 2.1: Schematic diagram of a typical gas-filled radiation detector [5].

There are six regions at which gas-filled radiation detectors are designed to be operated (Fig. 2.2.), and the collection of ion pairs is a function of the applied voltage [6]. The first region is referred to as recombination region. In this region, the applied voltage is not sufficient enough to collect all the created ion pairs before some can recombine [2]. Since the voltage in this region is too low, there is no gas-filled detector designed to operate in that region. Region 2 is called ionization region. A radiation particle or photon enters the detector volume and ionizes the gas, creating ion pairs. As the voltage across the electrodes is increased, a voltage range is reached whereby all the created ion pairs are collected before recombining [3]. Gas-filled radiation detectors designed to operate in this region are called ionization chambers and these detectors are characterized by complete collection of ion pairs before recombination without gas amplification. The performance of these detectors is affected by temperature, pressure and humidity. In ionization region, the current/pulse is proportional to the ionizing event produced.

Region 3 is called proportional region and is formed when the voltage of the gas-filled detector is increased above ionization region (region2), electrons produced by the primary ionization gain more energy to produce additional ionization as they collide with the gas molecules in the chamber [6]. The number of electrons produced increases exponentially with the applied voltage across the electrodes, because each primary electron is given a momentum to produce small 'avalanche' of electrons [2, 4]. Gas-filled detectors designed to operate in this region are referred to as proportional counters and are characterized by gas multiplication which produces a pulse that is proportional to the initial ionization [2]. These detectors are used to detect both alpha and beta particles and are capable of differentiating the two particles based on the size of the pulse each particle produce, which in turn depends on the energy of the incoming pulse.

When the voltage across the chamber is increased to several hundred volts, the gas multiplication is increased very rapidly, and more electrons produce avalanche. Later on, the electrons begin to interact with each other creating a region of limited proportionality (region 4) [4]. Within the region of limited proportionality, the instrument is unstable, and it is impossible to calibrate it. Hence, there is no gas-filled detector designed to operate in that region.

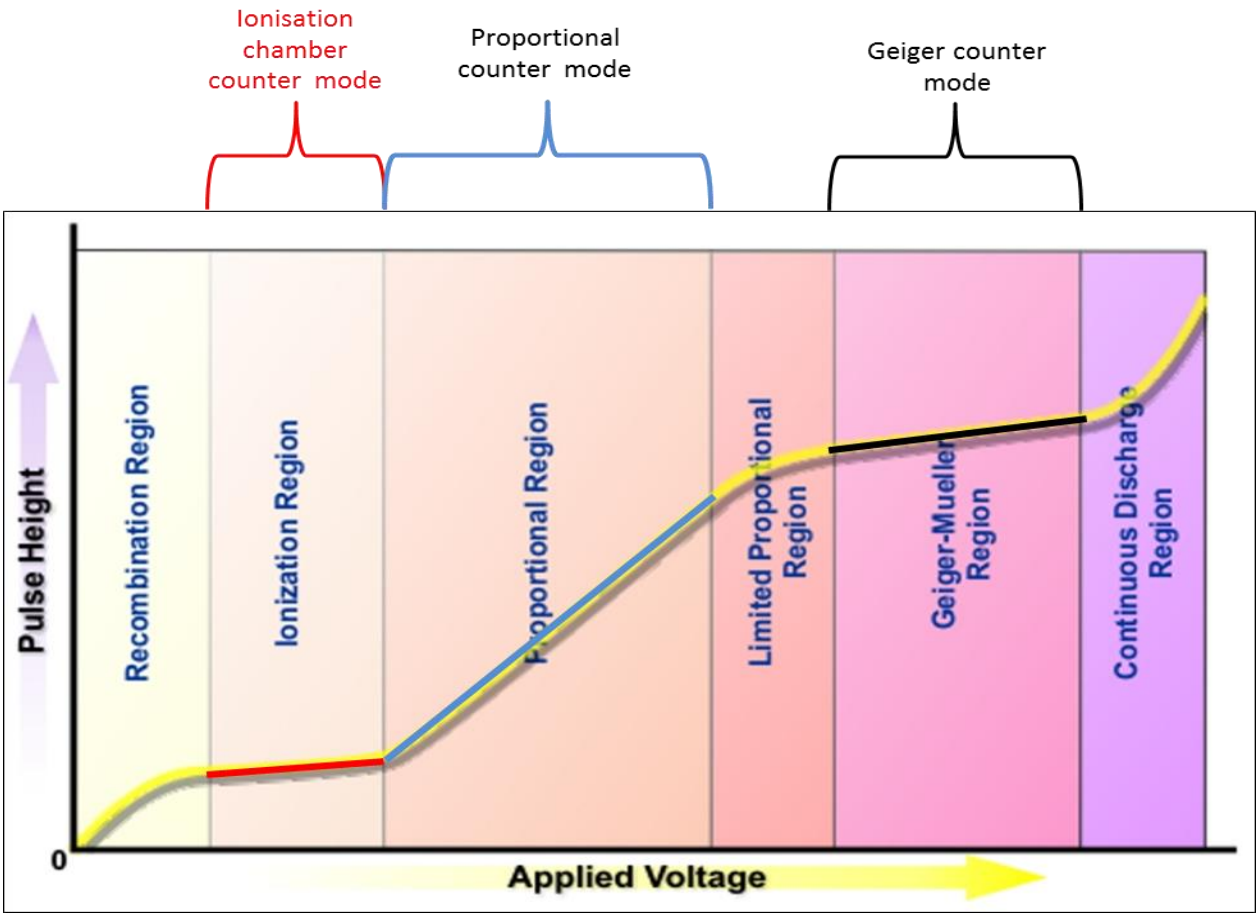

Figure 2.2: Operating regions of gas-filled radiation detectors [7].

Region 5 is called the Geiger-Muller region. In this region, further increase in applied voltage does not lead to an increase in the output pulse amplitude. The avalanche effect creates so many positive ions that move slowly compared to electrons to reach the collecting cathode. As a result, a "shield" of residual positive ions is created around the anode by positive ions. This shield reduces the

external field to be below a point where gas multiplication can take place and the output response reaches a plateau [1, 4]. Gas-filled radiation detectors that are designed to operate in that region are referred to as Geiger-Muller (GM) counters. GM counters are characterized by plateau voltages that create an avalanche of discharge throughout the counter for each ionizing radiation entering the counter [1]. These counters are designed to detect alpha, beta particles or gamma rays. Beyond Geiger-Muller region, a continuous discharge occurs (region 6). In this region, the voltage is too high and the chances of causing arcing and breakdown of the detector gas are high.

As mentioned above, gas-filled radiation detectors utilize a gas or a mixture of gases as a detection medium. The ratio of the gases in the mixture depends on the type of detector and the application. Optimum performance of the instrument is maintained by replenishing the gas with time [3]. In general, the gases used to fill up the gas-filled detectors are not free from contaminants. These contaminants have several vibrational energy levels and therefore, they are able to absorb electrons in a wide range of energy. Some of the most problematic contaminants include electronegative molecules such as oxygen and water vapor [3]. The concentration of these contaminants increases with time due to degassing of the chamber, and if the detector window is very thin, such contaminants find their way into the detector through diffusion from outside. The main effect of these contaminants is that they absorb electrons and results in a degradation of the signal [3].

2.2.2. Scintillation counters

Scintillation counters are radiation detectors that use a scintillator material to detect radiation. A scintillator material gives off light when struck by radiation. That radiation can be either charged particles, neutrons, gamma rays or X-rays. There are three types of scintillator materials that are normally used as detection media. These scintillators are plastic/organic, inorganic and liquid

scintillators. Amongst these, inorganic scintillators are discussed further because they are the most widely used scintillators for radiation detection applications [2]. The energy diagram of a scintillator material is similar to that of semiconductors (to be discussed in section 2.2.3). When a pure scintillator material absorbs energy, electrons get excited from valance band to the conduction band. Upon their de-excitation, light photons are emitted during the process.

The probability of photon emissions during the de-excitation process may not be efficient [3]. To increase the probability of photon emission, impurities or dopants are deliberately introduced into the scintillator materials through a process known as doping. The impurities or dopants are called activators. These activators modify the normal energy band structure of the pure scintillator atom. As a result, energy states are created within the forbidden gap through which electrons de-excite back to valence band [2, 4]. Since the energy gap is less than that of a full energy gap, this transition can now give rise to a visible photon and therefore serves as the basis of scintillation process [6].

When a charged particle interacts with the scintillator material, it creates a large number of ion-pairs. Holes move to activator site and ionize it since the ionization energy of the impurities is less than that of a pure scintillator crystal. In the meantime, the electron is free to move out of the crystal and this movement will continue until that "free electron" comes across the activator that is ionized by the holes [1]. Then the electron can jump into the activator site resulting in the creation of a neutral configuration that can have its own set of excited energy states [3, 4]. If the activator state created is an excited configuration with an allowed transition to the ground state, its de-excitation will occur very quickly and with high probability for photon emission. In a radiation detection instrument, the emitted photons upon electron de-excitation are allowed to interact with the photocathode of a photomultiplier tube (PMT). When the emitted photons interact with the

photocathode of the PMT, electrons are emitted during that process. Emitted electrons are then accelerated along a system of dynodes, producing more electrons. The "multiplied" electron pulse is collected at the electrodes for further signal processing and display, as shown in Fig. 2.3.

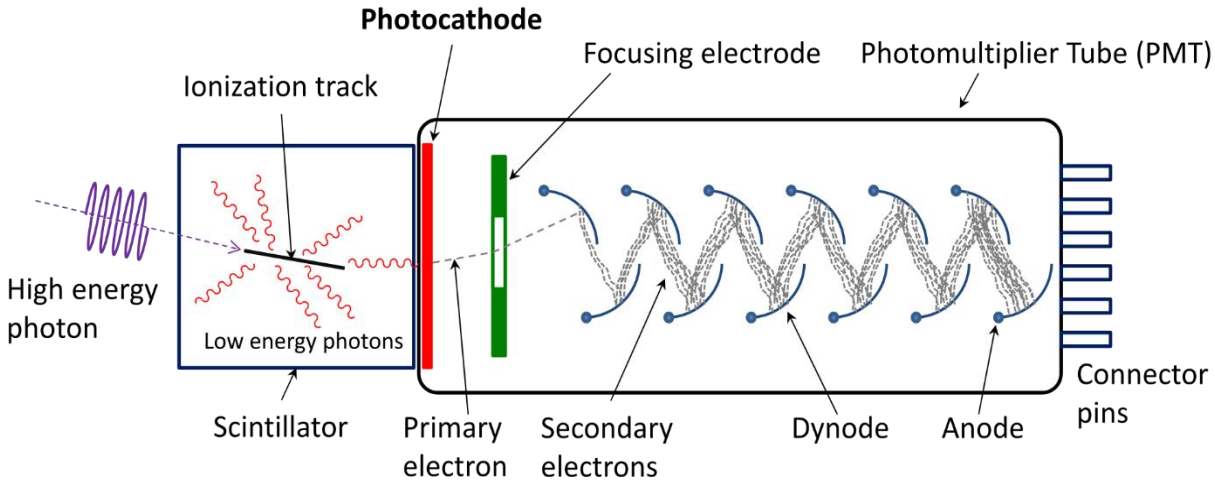

Figure 2.3: Schematic diagram of scintillation counter [8].

NaI (Tl) and bismuth germinate (BGO) are the most commonly used inorganic scintillators for radiation detection. The first use of NaI (Tl) was in 1948 when Robert Hofstadter [9] demonstrated that it produces a large scintillation light output compared to organic scintillators. NaI (Tl) suffers several drawbacks in that it is hygroscopic and may deteriorates due to water absorption if exposed to atmosphere for any length of time. Therefore, it is usually sealed in stainless steel, and this limits the detection of low energy radiation such as alphas and betas. BGO on the other hand, is used to detect gamma rays due to its high density of 7.13 g/cm and a large atomic number of 83 of the bismuth components. Unfortunately, the light yield is reported to be 10 to 20% of that NaI (Tl) [1]. In addition, its relatively high refractive index (2.15) makes efficient collection of the light more difficult than scintillators with lower index values [2]. The light output from BGO decreases with an increase in temperature and this severely limits its usefulness in high temperature applications.

2.2.3. Semiconductor detectors

Semiconductors are materials whose electrical conductivity lies between that of insulator materials and conductors. Semiconductor-based radiation detectors utilize semiconductors as detection media to sense ionizing radiation. Atoms in a semiconductor material are held together by covalent bonding and this covalent bond between atoms creates allowed discrete energy levels that are lumped together in two bands, namely valence band and conduction band [10]. The valence band is composed of electrons that are bound to lattice sites inside the crystal, while conduction band is composed of free electrons.

The two bands are separated by a forbidden gap. When there is no energy to excite the material, valence band is filled with electrons while the conduction band is empty of electrons. When external energy that is more than the bandgap is applied or absorbed, electrons get excited from valence band to the conduction band, leaving holes in the valence band. Electrons and holes are charge carriers that are responsible for conductivity of the material. Another way of increasing free electrons in a semiconductor is through doping, whereby impurities/dopants are deliberately introduced into the lattice structure of the material.

When dopants are introduced into the lattice structure of the semiconductor, the dopants occupy the spaces that were occupied by the atoms of the semiconductor. When the dopant has one or more valence electron than the semiconductor atom, this excess electron does not form electron pair band because there is no adjacent valence electron available [11]. This excess electron increases the conductivity of the semiconductor. The resulting material is called n-type semiconductor and the dopant with excess of one or more valence electron is referred to as donor

atom. An n-type semiconductor is composed of excess electrons as majority charge carriers and holes as minority charge carriers.

When a dopant with one less electron in its valence shell is introduced into the semiconductor material, the resulting material is called p-type semiconductor. P-type semiconductors contain an excess of holes as majority charge carriers and electrons as minority charge carriers. Dopants with one less electron in their valence shell are referred to as acceptor atoms. The presence of holes in the semiconductor material encourages the flow of electrons, resulting with an increase in conductivity of the material. When utilized as radiation detectors, semiconductors make use of the change in conductivity of the p-n junction when exposed to radiation as described below [11].

Semiconductors become useful as radiation detectors when n and p-type semiconductors are in contact creating a junction that offers special properties of interest [10, 11, 12]. At the junction, electrons from n-type semiconductor diffuse into the p-type semiconductor and the acceptor holes diffuse from p-type semiconductor into the n-type semiconductor. When an n-type material loses electron, it acquires a positive potential with respect to p-type material and it tends to prevent further diffusion of holes and electrons because of the potential difference at the junction, resulting in a charge depleted region. A depleted region is a region occurring due to electrons-holes recombination and this region creates a region of space charge, which opposes further migration of holes and electrons [13, 14]. The creation of depleted region makes it possible to use the diode junction for radiation detection [10, 11, 13]. The depletion region acts as a sensitive region of the semiconductor detectors [8, 9]. When ionizing radiation enters this region, it ionizes the atoms within the region and creates free electrons and holes (Fig. 2.4). When an electric field is applied,

the created electron-hole pairs move within the volume and the resulting motion gives rise to electrical signals that can be detected and measured.

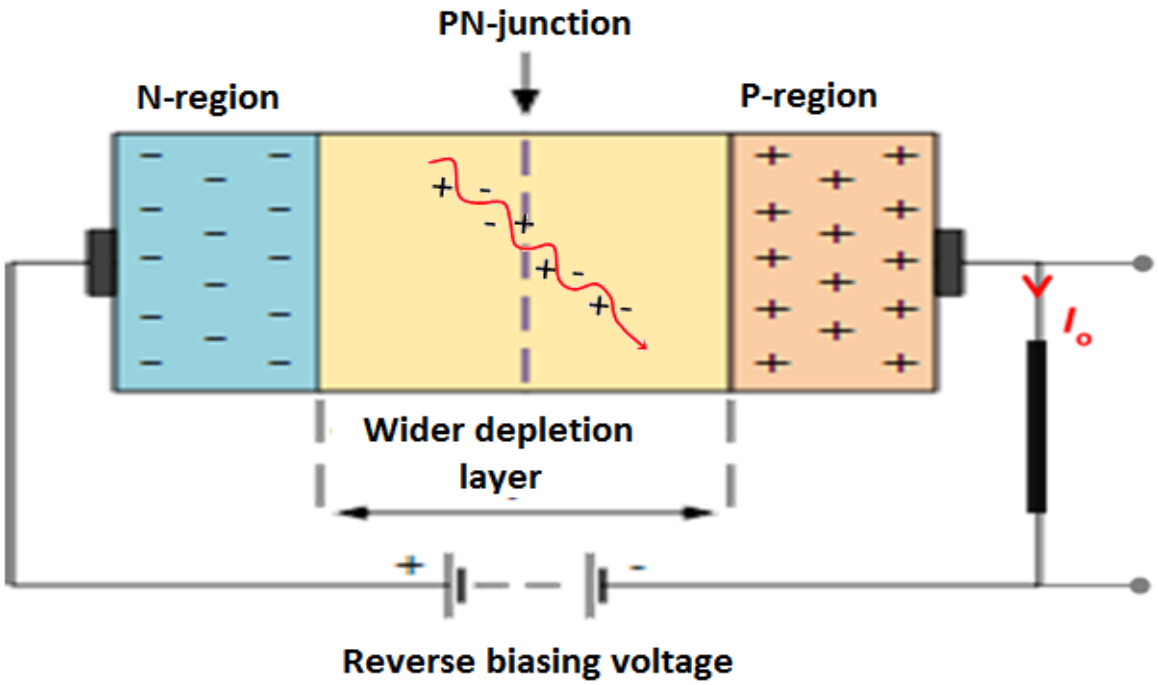

Figure 2.4: Schematic diagram of a semiconductor detector showing ion-pair creation along a radiation particle path [15].

There are two ways of biasing p-n junctions, namely reverse-biasing and forward-biasing. Reverse biasing occurs when a negative terminal of the battery is connected to the p-type material and the positive terminal to the n-type material, while forward biasing occurs when an external voltage is applied to the p-n junction making the p-type material positive with respect to the n-type material. The preferred type of biasing for radiation detectors is reverse biasing. This is because in a reverse-biased junction, when voltage increases the size of the depletion region increases, the junction capacitance decreases, the electric field increases and thus the detection performance is improved [12, 13].

Not all the semiconductors are used as radiation detection media. When selecting a semiconductor for radiation detection purposes, there are several important factors that are taken into consideration and some of these factors include charge mobility, operating temperature and resistivity [3,13]. This is because the material have to generate more charge carriers after interacting with the incident radiation and the functionality of the material should not be affected by any fluctuations in temperature. Most commonly used semiconductors for radiation detection media are silicon (Si) and germanium (Ge) [1, 13]. The fact that silicon has moderate intrinsic charge carrier concentration and intrinsic resistivity, makes it suitable for use as a radiation detection medium [1, 10, 12]. However, silicon-based detectors suffer several drawbacks. The crystal structure of silicon is prone to radiation damage.

When ionizing radiation interacts with a semiconductor material in a detector, it can cause damage to the crystal lattice structure of the semiconductor material. This damage depends on the energy and the type of the radiation incident on the material. Radiation damage to the crystal structure of the semiconductor material produces Frenkel defects, which are vacancy-interstitial pairs, formed when an ion gets excited from a normal lattice point to an interstitial site, leaving a vacancy behind. These defects act as recombination/generation centers since both are able to capture and to emit charge carriers. As a result, trapped signal charge could be released too late, thus producing an incomplete charge collection at the detector electrodes. Thus, the damage can also be explained in terms of charge.

In addition, silicon-based detectors are easily affected by temperature changes. For example, any slight changes in temperature can change the dimensions of the bandgap. Any changes in the size of the bandgap results in non-linearity in the detector response. If the size of the bandgap is

reduced, more electron-hole pairs will be produced with the same deposition energy, while on the other hand if the bandgap is widened, electrons will find it difficult to be excited from valence band to the conduction band, and this will decrease the conductivity of the material [2]. Germanium has a similar crystal structure to that of silicon, but the difference lies in the bandgaps. The bandgap of Ge is roughly 0.7 eV, which is almost half of that of silicon. Low bandgap implies that more charge carriers are produced per MeV radiation. However, low bandgap leads to severe thermal fluctuations at room temperature [2, 12, 13]. Therefore, high purity germanium (HPGe) detectors need to be cooled down to liquid nitrogen temperature to keep the instrument at its optimum performance. Cooling down to liquid nitrogen temperature is an inconvenient process since the detector requires hours to cool down to operating temperatures before using it.

2.3. Advent of polymer-based radiation sensors

Polymer-based radiation detectors are relatively new type of radiation detectors that use CPs as the sensing material. The advent of polymer-based electronics, or organic electronics as it is alternatively known, is characterized by research into application areas previously regarded as the preserve of silicon-based electronics. The use of polymeric films in device applications is becoming more commonplace due to relatively low production and material cost of polymers [16] when compared to conventional semiconductors. Moreover, when compared to radiation sensing materials that are commonly used, CPs are mechanically flexible. Being flexible, polymer radiation sensors can be formed into any shape to measure and monitor radiation levels in complex and compact locations. For example, they can be shaped into a tube and placed around piping to remotely monitor radioactive fluids/steam [17].

In addition, polymers are environmentally stable [18]. This implies that when used as a sensing material, the functionality of the instrument will not be affected by slight changes in temperature, humidity and pressure unlike ionization chambers. Research efforts into polymer-based radiation sensing materials are geared towards modifying the properties of the polymers to improve their quantum efficiency to at least match that of silicon-based detectors. Polymer-metal nano-composites, for example, exhibit distinctive electrical and optical properties in comparison with other nano-sized systems due to the interaction between the metal nanoparticles and the polymer matrix [19].

2.4. Conducting polymers

As mentioned previously, conducting polymers (CPs) are classified as a special class of organic materials that are characterized by a backbone chain consisting of alternating single-double bonds [20]. In their chemical structure, CPs are mainly composed of carbon (C), hydrogen (H) atoms and heteroatoms such as nitrogen (N) and sulphur (S). In their ground state, carbon atoms have six electrons that are arranged as $1s^2\ 2s^2\ 2p^2$, which in total give four electrons from the outer shell of each carbon atom. In a structure whereby, the heteroatoms are bonded to C atom, the arrangement of the electrons may be hybridized into sp, sp^2 or sp^3 orbitals, each having its own spatial character [21]. Hybridized sp, sp^3 and other orbitals are strongly hybridized. In case of sp^2 orbital, there is only one p_z orbital that is not hybridized. The three sp^2 orbitals are orientated 120° to each other, and the unhybridized p_z orbital is orientated 90° to these three sp^2 orbitals [21], as illustrated in Fig. 2.5.

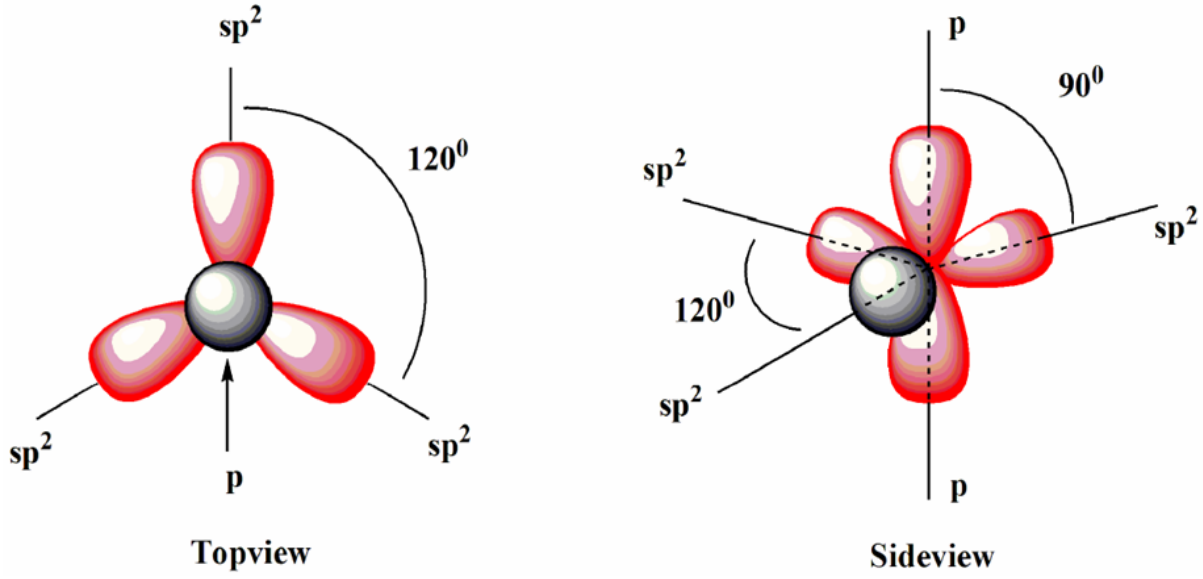

Figure 2.5: Spatial representation of sp^2 hybridized carbon atom from top and side view [21].

When carbon atoms having identical hybridized orbitals with similar orientation are arranged next to each other in a structure, the p_z orbitals will overlap, resulting in the formation of molecular π-bond [21], as shown in Fig. 2.6. Looking at the figure, there is a double bond between the first and second carbon atoms and that double bond is formed because of the presence of π-bonds and σ-bonds (created by two sp^2 orbitals). Stacking of the neighbouring sp^2 hybridized C atoms, together with their unhybridized p_z orbitals result with the formation of alternating single and double bond structure [21] (Fig. 2.6). CPs are distinguished from other polymers by alternating single-double bonds and the presence of σ-bonds between carbons that are sp^2 hybridized [21], i.e. there is one unpaired π-electron from the outer shell of each C atom [21, 23]. These unpaired π-electrons are delocalised and overlap along the polymer backbone which facilitates the possibility of movement of both negative and positive charge carriers [23]. The presence of π-bonds in the structure determine the semiconducting or metallic properties of the CPs.

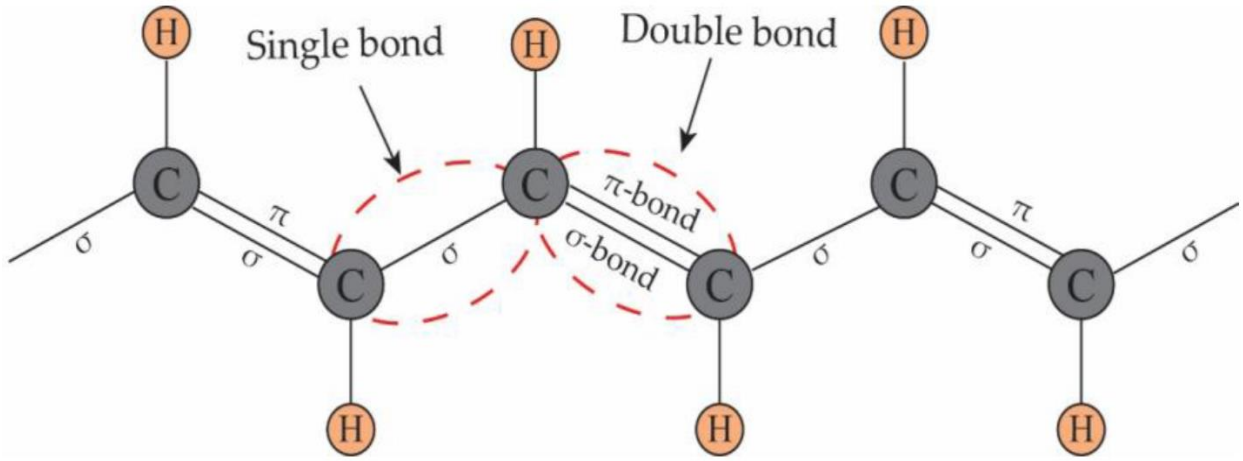

Figure 2.6: Structure of polyacetylene: The backbone containing conjugated double bonds [22].

Conducting polymers find widespread use in a variety of applications such as:

- Light Emitting Diodes (LEDs) [24, 25],
- Thin film transistors [26],
- Corrosion resistant coatings [23],
- Electromagnetic shielding [27],
- Polymer based rechargeable batteries [27],
- Polymer actuators [28],
- Sensors and molecular electronic devices [28], and
- Solar cells [29].

Examples of the most common conducting polymers are polythiophene, polypyrrole, poly (triarylamine), polyacetylene, polyaniline, polyphenyl and poly (phenylene-vinylene) [30, 31]. Fig. 2.7 shows basic chemical structures of some of the conjugated polymers.

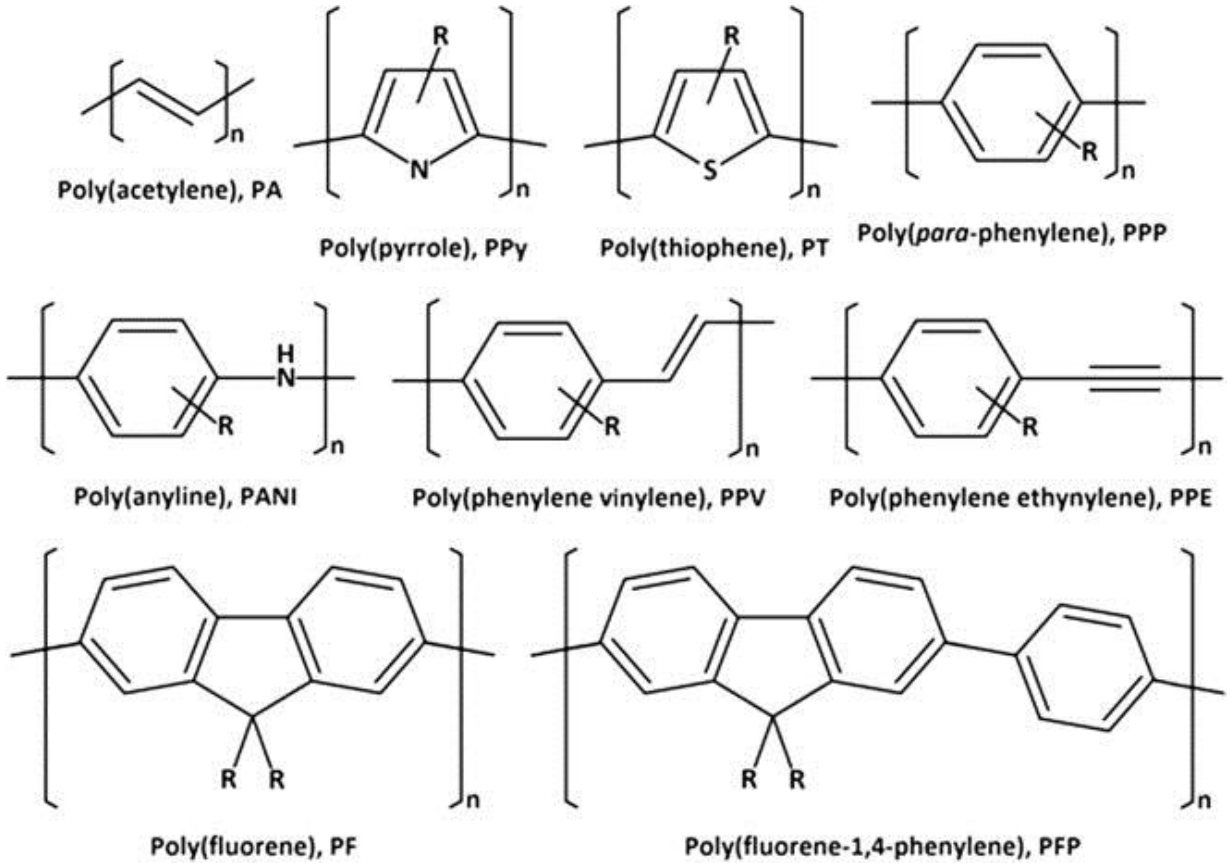

Figure 2.7: Chemical structure of some conjugated polymers [32].

Conducting polymers offer many properties of special interest when compared to other materials in that:

- When compared to conventional semiconductors like silicon, conducting polymers are flexible, easier and relatively cheaper to synthesize [16, 31],
- Conducting polymers are light in weight, have good mechanical properties (flexibility) and tunable electronic properties. Therefore, they have potential to replace semiconductor materials and other materials in variety of applications [33],
- A process called doping can be used to enhance the electrical conductivity of the CPs by several orders of magnitude by changing the structural order of the polymer [34],

- Unlike other materials, optical/electronic properties of CPs are not produced by fabrication or processing techniques but are locked into the molecular structure. For applications in electronics, this means that modifying the structure of the polymers will alter the electronic/ optical properties before the actual device can be fabricated [34], and
- It is possible to make ohmic contacts using different metals on polymers and to fabricate devices such Schottky diodes [34, 35].

2.5. Band theory and classification of conductivity

According to the band theory of solids, the electrical properties of direct gap inorganic semiconductors are determined by their electronic structures, and the electrons move within discrete energy states called bands and these bands are valence and conduction bands. The valence band is the energy band that results from bonding orbitals of a molecule, while the conduction band is a result of the antibonding orbitals of the molecule [36]. The width of individual bands across the range of energy level is called band width. The valence band (VB) represents the highest occupied molecular orbital (HOMO) and the conduction band (CB) represents the lowest unoccupied molecular orbital (LUMO) [36]. The gap between the two bands is called forbidden gap (E_g). This gap represents a range of energies which are not available to electrons [20].

The level of electrons in a system which is reached at absolute zero is called the Fermi level (F_g) [20]. For CPs to allow the formation of delocalized electronic states, the molecular arrangement of these polymers must be conjugated [37]. The size of the band gap depends on the extent of delocalization and the alternation of double and single bonds [36]. Moreover, the size of the band gap will determine whether the CP is an insulator, semiconductor or metal and can be differentiated according to their energy band gaps, as shown in Fig. 2.8.

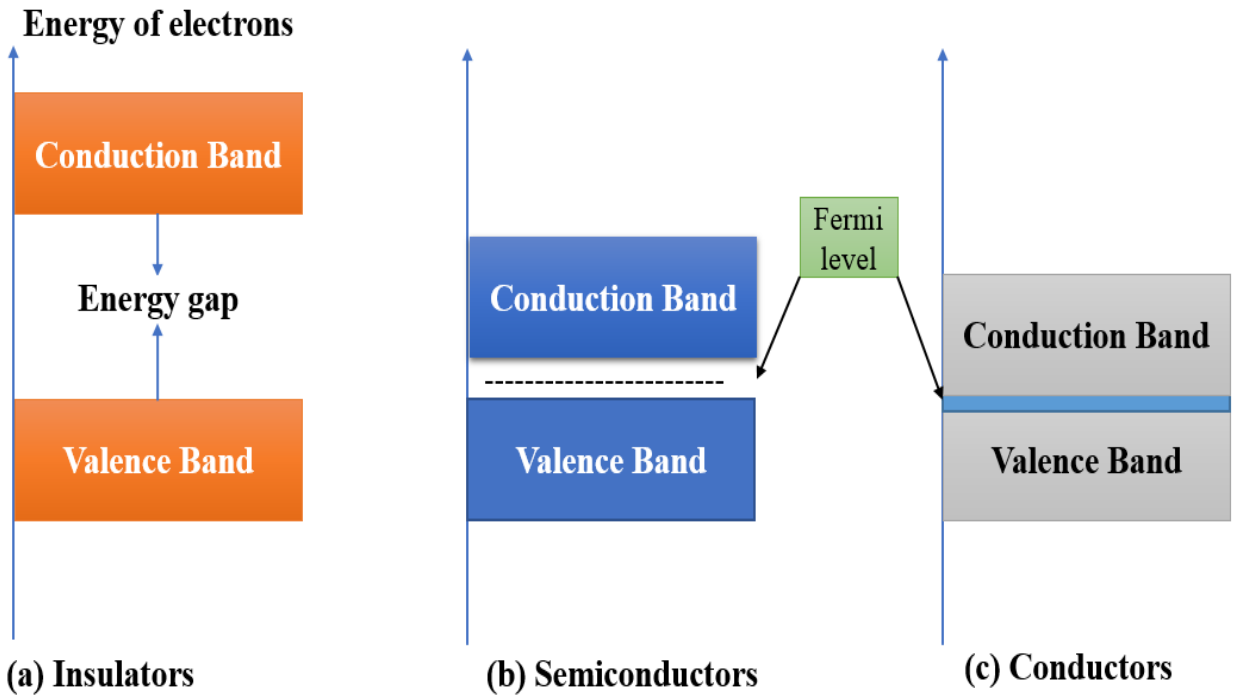

Figure 2.8: Typical energy gap diagrams of (a) insulators, (b) semiconductors and (c) conductors.

Insulators, as shown in Fig. 2.8 (a), are characterized by a wider energy gap between VB and CB. Since the energy gap between these two bands is large (E_g > 3.0 eV) [20], electrons are not able to be excited from VB to the CB, hence they are poor conductors of electricity at ambient temperature. In case of semiconductor materials, as shown in Fig. 2.4 (b), the band gap is small, i.e. E_g = 0.1 to 3.0 eV [38]. Since the band gap is small, electrons can easily be excited from VB to CB to contribute to the electrical conductivity [38]. The holes left behind when electrons excite from VB to CB also contribute to electrical conductivity. In conductors (Fig. 2.8 (c)) there is no band gap, i.e. E_g = 0 eV [20]. Conductors always have a partially filled free-electron band, because the conduction and valence bands overlap. Hence, electrons can readily occupy the conduction band [20]. Table 2.1 lists the band gaps of selected CPs and semiconductors [18, 39].

Table 2.1: Energy gaps of selected CPs and semiconductors.

CPs	Eg (eV)	Semiconductor	Eg (eV)
Polyacetylene	1.7	Silicon	1.1
Polypyrrole	3.2	Germanium	0.7
Polyaniline	3.0	Zinc Oxide	3.3

In nature, conducting polymers are insulators but their electrical conductivity can be varied depending on several factors such as the type of the polymer and impurity type and content. Fig. 2.9 shows conductivity range of conducting polymers.

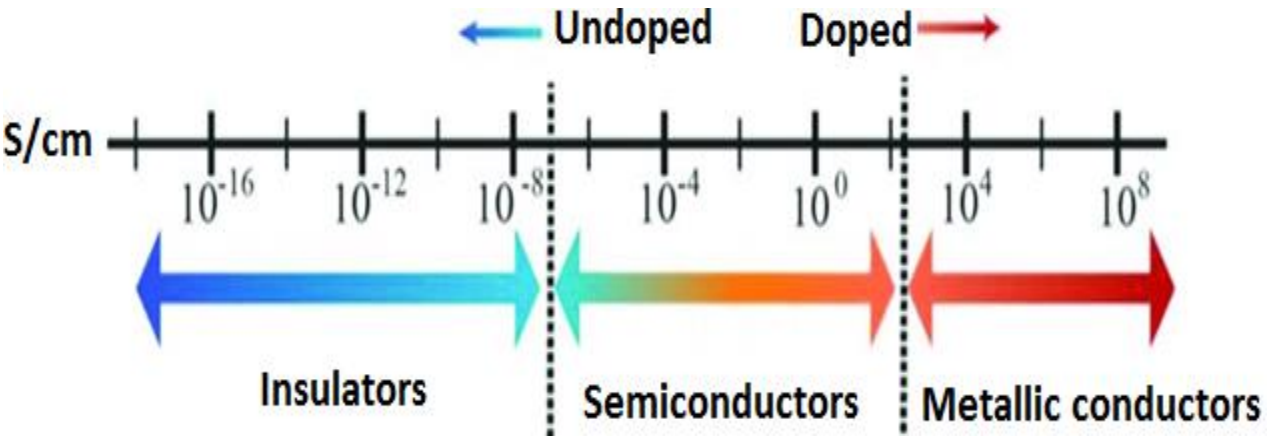

Figure 2.9: General conductivity range of conducting polymers [22].

It is shown from Fig. 2.9 that the conductivity of pristine conducting polymers ranges from 10^{-10} to 10^{-6} S/cm and this conductivity can be increased by several orders of magnitude through doping. For example, Li B et al. [40] reported doping of Poly (p-phenylene vinylene) films with nitrogen ions and achieved a conductivity of $3.2x10^{-1}$ S/cm, which was higher than the conductivity of the pristine films by seven orders of magnitude.

Similarly, Tsukamoto et al. [41, 42] reported doping of polyacetylene with iodine and achieved conductivity of more than 10^4 S/cm, which is comparable to conductivity of lead at room temperature (4.8×10^4 S/cm). The achievement of such high conductivity widens the scope of applications for CPs. Polyaniline, as an example, can have conductivity ranging from 10^{-8} to 400 S/cm [18] and can be used in variety of applications such as light emitting diodes (LED), metallic corrosion resistance layers, organic rechargeable batteries etc. [18].

2.5.1. Doping of polymers

Although the π-electrons in CPs are delocalized along the polymer chain, a pristine conducting polymer is classified as an insulator. However, as mentioned previously, the conductivity of that polymer can be changed from insulating to either semiconducting or metallic by a process called doping. In case of CPs, Bredas et al. [43] defined doping as a redox reaction through which a non-conducting pristine polymer is transformed into an ionic complex made up of a polymeric cation/anion and a conterion, which is the reduced/oxidized form of oxidizing/reducing agent. Upon doping, bond disruption takes place and this results in alteration of the electronic, electrical, optical and structural properties of the polymer. Conducting polymers can undergo p-type or n-type doping, where π-electrons are partially removed (oxidation) or added (reduction) from or to the π-system of the polymer backbone. Upon doping, an insulating or semiconducting polymer having low conductivity range could be transformed into a polymer which is in the "metallic" conducting regime. In addition, doping results in the generation of polarons, bipolarons and solitons (to be discussed in section 2.5.3). Comparing the two types of doping, n-type doping creates negatively charged carries, which are not as stable as positively charged carriers, and this makes p-type doping more reliable [22].

2.5.2. Dopants

Dopants are chemical oxidants or reductants that are incorporated into the polymer matrix through a chemical or electrochemical route, ion implantation or in situ incorporation of NPs into the polymer matrix [34]. Table 2.2 lists selected dopants used to dope conducting polymers.

Table 2.2: Typical dopants for CPs.

Dopants	Structure
Perchlorate	ClO_4^-
Copper	Cu^+
Argon	Ar^+
Hydrochloric acid	HCl
Camphor sulfonic acid	$C_{10}H_{16}O_4S$
Bismuth Oxide	Bi_2O_3

Conductivity of CPs is directly proportional to the doping density (number of dopant ions incorporated into the polymer matrix). When doping level is increased, high conductivity can be achieved due to creation of more charge carriers. Maximum doping level attained is dependent on the polymer type and dopant used. After being incorporated into the polymer matrix, dopants occupy interstitial sites between the polymer chains and undergo redox process in which charge is being donated to or accepted from the polymer backbone [21].

2.5.3. Formation of polarons, bipolarons and solitons

As mentioned previously, introduction of dopants into the chain of a pristine conducting polymer leads to structural distortion of the polymeric structure. These structural distortions lead to the creation of states called polarons and bipolarons, as illustrated in Fig. 2.10. When an electron is removed from the π-system of the backbone chain through doping, a positive polaron (having

single charge +*e*) is formed, while the addition of electron results with the creation of a negative polaron (having single charge -*e*). The polaron can be a cation or a radical and it is associated with a structural distortion in CPs. Furthermore, a polaron carries a half spin [43]. The formation of a polaron gives rise to two localized electronic levels within the band gap (Fig. 2.10-b).

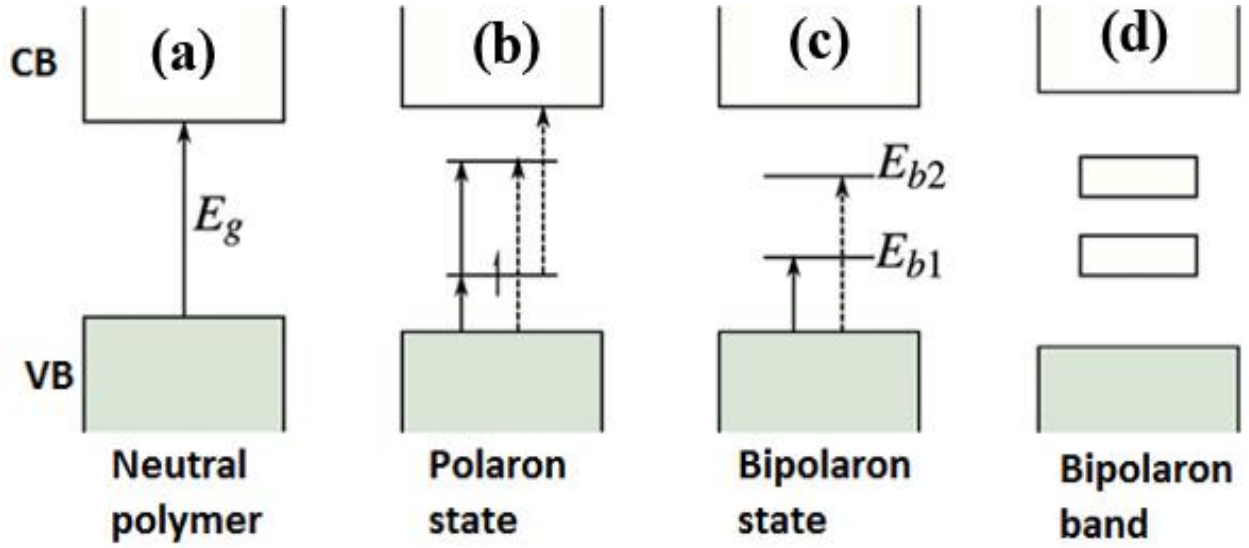

Figure 2.10: Polaron and bipolaron states formation in conducting polymers [29].

When a second electron is removed or added to a pre-existing polaron, a positive (having charge +2*e*) or negative (having charge -2e) bipolaron is formed (Fig. 2.10-c). A bipolaron is spinless and stable, despite Coulomb repulsion of the two similar charges [43]. Comparing the two charge carriers, bipolarons have lower energies than polarons by 0.4 eV [43]. As shown in Fig. 2.10-d, there are empty bipolaron bands located symmetrically within the band gap. At high doping levels, both upper and lower bipolaron bands merge with the conduction and the valance bands, respectively, to produce partially filled bands like that of metals.

At high doping levels, the charged solitons interact with each other to form a soliton band which can eventually merge with the band edges to create true metallic conductivity [22, 44]. This is shown below in Fig. 2.11. Solitons are excitation charge carriers commonly known to be charge

carriers in degenerate polymers (polymers that possess two structures, i.e. alternating C-C and C=C bonds, with equal energy in the ground state) such as trans-polyacetylene [22].

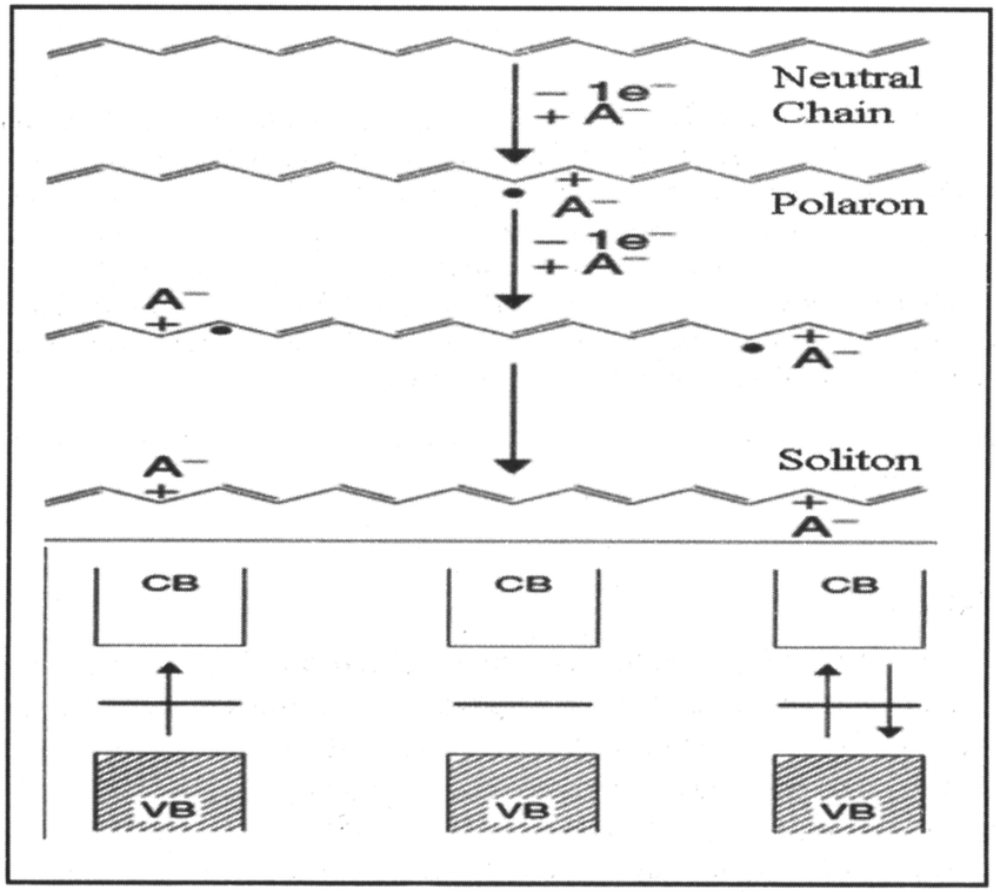

Figure 2.11: Formation of neutral, positive and negative solitons in trans-polyacetylene [44].

If there is an odd number of carbon atoms in the CPs chain, one π-electron remains unpaired, and a neutral soliton is said to occur. This defect can be thought of as $2p_z$ unhybridized orbital of Sp hybridized carbon atom, which is the nonbonding orbital occupied by a single electron [44]. Addition or removal of one electron to the neutral state corresponds to a negative or positive soliton with zero spin as shown in Fig. 2.11. The arrow indicates electron with spin direction. The soliton level can accommodate zero, one and/or two electrons and thus it may also be positively or negatively charged, giving the unusual property of separating spin and charge, with neutral solitons

possessing a half spin with zero charge. Both positive and negative solitons possess charge but no spin. These charge carriers can move along the chain without a distortion [44].

2.6. Doping techniques

Ion implantation is a surface or near-surface doping technique utilized to modify properties of insulating polymers, particularly to turn them into either semiconductors or conductors [45]. A change in conductivity of polymers depends on several factors, namely; the type of polymer, implantation regime (high or low –energy regime) and implantation conditions (ions used, ion fluence, ion current density and implantation temperature and energy). In this technique, a target material in the form a polymer film is bombarded with an energetic beam of positively charged ions (typically from 1 keV to 1 MeV). These ions penetrate through the polymer material, slow down by transferring their energy to the target atoms/electrons and eventually stop at a certain depth (~ 0 – 1 μm). Ion implantation of polymers is different from implantation of conventional semiconductors in that; when ions are introduced into the polymer matrix, they generate defects, which break the chemical bonds. This breaking down of chemical bonds lead to a significant alteration of the electronic structure of the polymers, thus a change of conductivity [46].

When the implanted ions interact with the atoms or molecules of the polymer, reactive intermediates in the form of excited atoms, ions and free radicals are formed. Free radicals are easily attached to the molecules to initiate chemical effects such as carbonization of the polymer matrix, crosslinking and polymerization [45]. Carbonization refers to the process of making the polymer material rich in carbon [45, 47]. Carbon atoms are clustered with Sp^2 hybridization and this type of chemical bonding possess unpaired π-electrons, which become charge carriers in the implanted polymer [45]. In addition, free radicals initiate the creation of conducting islands within

the polymer matrix. These processes are responsible for a change in conductivity of the polymer. Carbon clusters [45, 47] are conducting islands, which allow electron transportation through hopping or tunneling between the islands [48]. The resistivity of CPs can be varied within ca. 20 orders of magnitude starting from pure dielectrics (ca. $10^{15} – 10^{18}$ Ω.cm) and reaching the level of poor conductors ($10^{-1} – 10^{-3}$ Ω.cm), depending on the type of polymer and the implantation parameters [45].

2.7. Polyaniline

Polyaniline is a conducting polymer that was discovered in 1834 by Runge. Back then it was known as aniline black [21]. Twenty-eight years upon its discovery, Letheby conducted research to analyze this material. In his work, he described the synthesis of polyaniline from anodic oxidation of aniline [21]. At that time, the electrical conductivity was not measured. In 1986, MacDiarmid et al. [49] found out that the aniline monomer in an acid aqueous solution can be chemically oxidized by ammonium peroxydisulfate (APS) to obtain a green powder of PANI having conductivity of about 3 S/cm. Since then, several methods such as chemical and electrochemical have been used to synthesize polyaniline [21]. This dissertation will not cover any method of synthesizing polyaniline from its monomer since the polyaniline used was purchased. Among the family of CPs, polyaniline is of great interest in research [50], due to its:

- Easy synthesis and low cost [31],
- High environmental stability [18] ,
- Mechanical flexibility [25],
- Tunable electrical, optical and structural properties through doping [18, 50],

- Ability to switch from the conductive form to insulating to conductive form as a function of pH [18], and
- Special doping mechanism by oxidation as well as protonation [18, 31].

Fig. 2.12 shows the general structure of PANI. As a mixed oxidation state polymer, consisting of benzenoid and oxidized quinoid units, PANI's average oxidation state is denoted as 1-y where: y determines the existence of each oxidation state, as shown below.

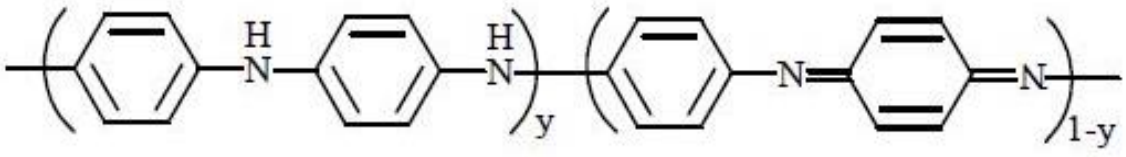

Figure 2.12: Different oxidation states of PANI (y =1: PNB, y = 0: LEB and y = 0.5 EB) [51].

2.7.1. Oxidation states of PANI

Polyaniline exists in four distinctive oxidation states, namely: leucoemeraldine base (LEB), emeraldine base (EB), and pernigraniline base (PNB) [52]. These oxidation states of PANI have different color, stability, electronic, and optical properties [34]. Each state is determined by the fraction of imine (-NH=) nitrogen atoms per 4-ring repeat, which is denoted by 1-y [34]. Where 1-y equals to 1, 0 and 0.5 for pernigraniline base, leucoemeraldine base and emeraldine base, respectively.

Pernigraniline Base (PNB)

PNB is a fully oxidized form of non-doped PANI, where 1-y = 1. It is composed of solely oxidized base units as shown below:

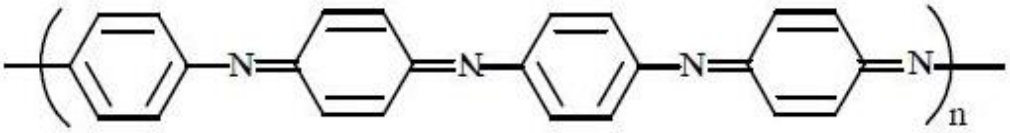

Figure 2.13: Pernigraniline Base structure [51].

PNB has an energy gap (E_g ~ 2.3 eV) that is intrinsic due to electron-phonon interaction [34]. The electronic structure of PNB is characterized in terms of a Pierls ground state that supports soliton and polaron defects [53]. Furthermore, PNB is composed of alternating aminobenzene and quinonediimine fragments. Since quinonediimine group is unstable in water, PNB and its salt readily decompose in air [54].

Leucoemeraldine Base (LEB)

As stated above, LEB is a fully reduced form of un-doped polyaniline denoted by 1-y = 0. It is composed of solely reduced units as illustrated below:

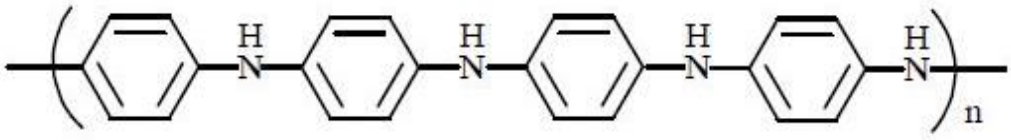

Figure 2.14: Leucoemeraldine Base structure [51].

LEB is an insulator characterized by a large band gap (Eg ~ 3.6 eV) [34, 55], which originates mostly from the difference in energy between bonding and anti-bonding molecular orbitals of benzene involved in the overlapping of molecular orbitals of neighboring phenyl rings and nitrogen atoms [34].

Emeraldine Base (EB)

Emeraldine base is an intermediate oxidation state of PANI with a large energy gap (Eg ~ 3.6 eV) [34] and 1-y = 0.5. EB is composed of equal amounts of alternating reduced and oxidized base units as shown below:

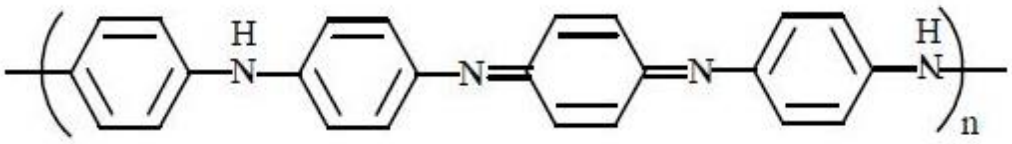

Figure 2.15: Emeraldine Base structure [51].

Emeraldine base is considered to be the most important form of PANI because it can be doped to achieve high conductivities. In addition, this form of PANI (EB) has unique properties when compared to other family of π-conjugated polymers since:

- Its conductivity can be changed from insulating to metallic state by adding protons to the –NH= sites while the number of electrons on the chain are held constant [21, 34, 56],
- It does not display charge-conjugation asymmetry [21, 34],
- It has a structure that contains the same proportions of amines (-NH-) and imines (=N-) sites [21, 34],
- It comprises an alternating ring-heteroatoms backbone structure and it is a generalized "A-B" type polymer where both carbon rings and nitrogen atoms are within conjugation path [21, 34] and
- The C_6 benzenoid rings can rotate or flip, significantly altering the nature of electron – interactions [34, 56].

Emeraldine Salt (ES)

Emeraldine salts is a conducting form of polyaniline that is formed by exposing insulating emeraldine base to protonic acids (a process which is a variation of either the number of protons, electrons or both) [34]. As mentioned in section 2.5.3, EB has structure which consists of equal proportions of amines (-NH-) and imines (=N-) sites and through protonic acids doping, imines sites are protonated by acids HA to the bipolaron (dication salt) form [57].

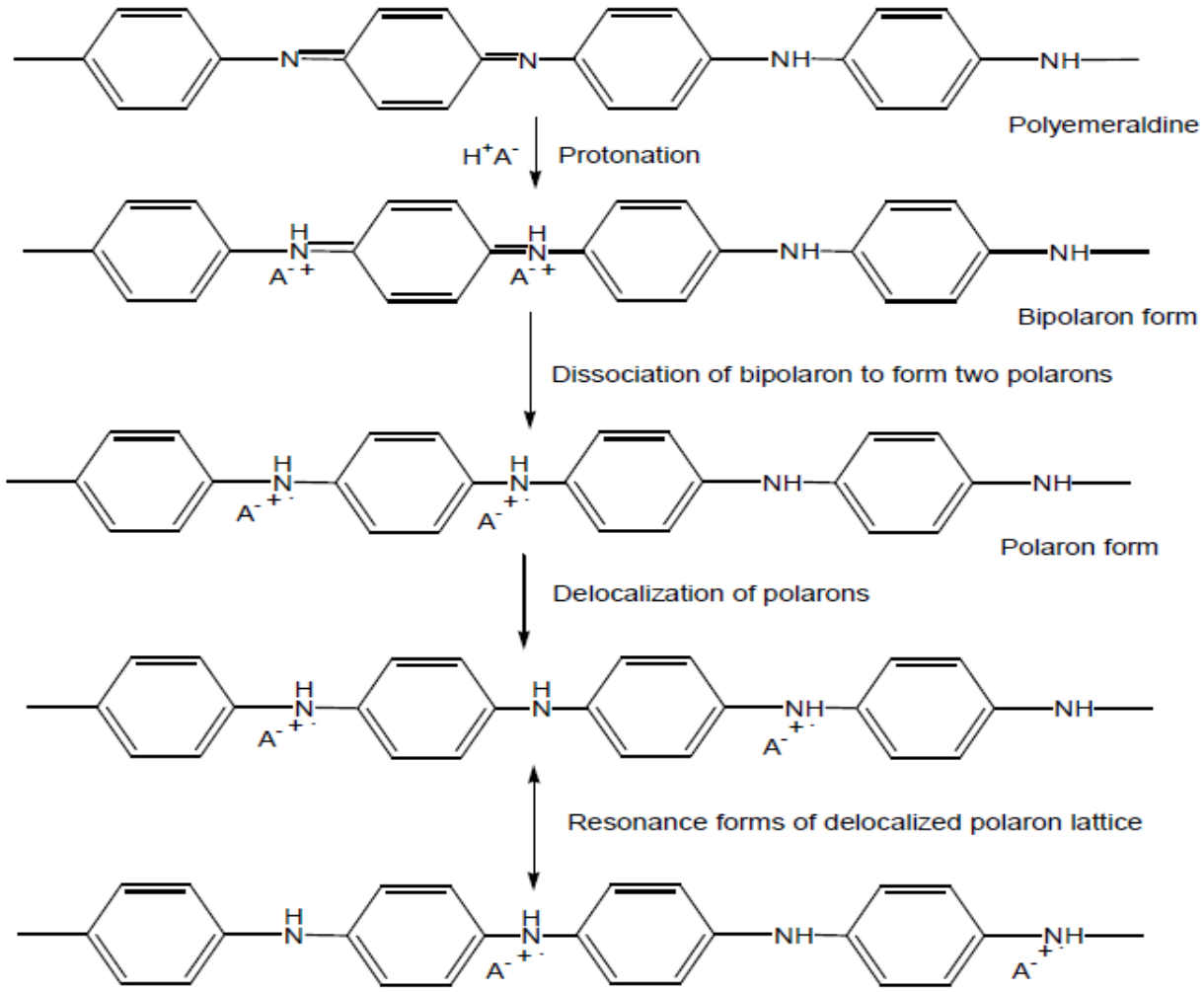

Figure 2.16: Doping of EB with protons to form conducting ES form of PANI (a polaron lattice) [20].

As shown in Fig. 2.16, the bipolaron rearrange further to form delocalized polaron lattice which is a polysemiquinone radical-cation salt. The resulting PANI, now in the form of emeraldine salt has conductivity comparable to that of a semiconductor (100 S/cm), which is many orders of magnitude higher than that of common polymers (< 10^{-9} S/cm) but lower than that of typical metals (> 10^{4} S/cm) [58]. This increase in conductivity, as mentioned previously, is dependent on several factors including dopants used, doping levels and processing in different solvents. Only about 1% of the charge carriers available in the ES contribute to the obtained conductivity and if all the available charge carriers were to contribute, the resulting conductivity at room temperature would ~ 10^{5} S/cm, which is comparable to that of copper [59].

2.7.2. Electrical and optical properties of PANI

Polyaniline has unique electrical properties that distinguish it from other CPs and its conductivity can be enhanced by adding protons to the –NH= sites while the number of electrons on the chain is not affected. The electrical conductivity of PANI is in the range of 10^{-8} to 400 S/cm [18, 20]. Fig. 2. 17 shows different band gaps for different redox state of polyaniline. PANI in ES form exhibits three distinctive characteristic energy bands at 330 nm attributed to π-π* band, and two bands at 430 nm and 800 nm in the region which are attributed to π-polaron band and polaron-π* band transitions, respectively [60].

The EB base form of PANI shows a low wavelength π-π* band and strong absorption band at around 600 nm attributed to a local charge transfer between a quinoid ring and the adjacent immine-phenyl-amine units (intramolecular charge transfer exciton) [20]. The reduced LEB has maximum absorption around 2.3 eV with two bands at around 320 and 530 nm which are assigned to π-π* and Peierl gap transition.

When doping acids or a base that protonates or deprotonates is added to the base –NH= sites, polyaniline changes colors and switches between oxidation states as a function of pH level [18]. For example, when pH > 4 PANI switches from conductive form (emeraldine salt) to insulative form (emeraldine base) [18].

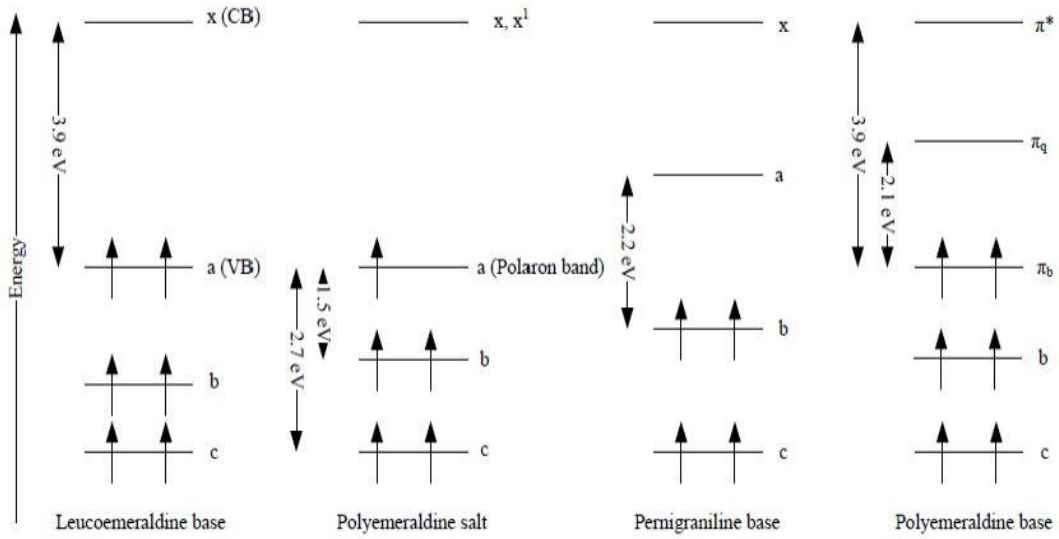

Figure 2.17: The energy gaps for different redox states of polyaniline [20].

2.7.3. Applications of PANI

Polyaniline finds widespread use in a variety of technological applications such as:

- Supercapacitors (as nanofiber composites of Graphene/Polyaniline) [18],
- Organic rechargeable batteries [18],
- Biological and environmental sensors [18],
- Metallic corrosion resistances [18, 34],
- Light Emitting Diodes (LED) [18, 54]
- Bioelectronics medical devices [18],
- Composite structures [18], and
- Membrane gas-phase separations [18].

2.11. References

[1] Knoll G. F. 2000 *Radiation Detection and Measurement*, 3rd edition. (John Wiley &Sons, Inc.: New York).

[2] Ahmed S. N. 2007 *Physics and Engineering of Radiation Detection*, 1st edition. (Academic Press.: Boston).

[3] Krane K. S 1988 *Introductory Nuclear Physics.* (John Wiley & Sons.: New York).

[4] Cooper P. N. 1986 *Introduction to Nuclear Radiation Detectors*. (Cambridge Univ. Press.: Cambridge).

[5] https://www.equipcoservices.com/support/tutorials/introduction-to-radiation-monitors/ [Accessed: September 2018].

[6] Leroy C and Rancoita P. G. 2004 *Principles of Radiation in Matter and Detection*. (World Scientific Pub. Comp.: Singapore).

[7] http://www.conceptualphysicstoday.com/2011/05/how-gm-tube-operates.html [Accessed: September 2018].

[8] https://upload.wikimedia.org/wikipedia/commons/e/e8/PhotoMultiplierTubeAndScintillator.svg [Accessed: October 2018].

[9] Hofstadter R. 1948 *Phys. Rev.* **74** 100.

[10] Deme S. 1971 *Semiconductor Detectors for Nuclear Radiation Measurement.* (Wiley-Interscience.: Hoboken).

[11] Rizzi M. *et al*. 2010. *J. Appl. Sci.* **10 (23)** 3141.

[12] Schlesinger T. E. and James R. B. 1995 *Semiconductor for Room Temperature Nuclear Detector Applications*. (Academic Press.: San Diego).

[13] Lutz G. 2007 *Semiconductor Radiation Detectors*, 2nd edition. (Springer Verlag Berlin Heidelberg.: New York).

[14] Bird J. 2000 *Electrical and Electronic Principles and Technology*, 3rd edition. (Elsevier Ltd.: Burlington).

[15] https://www.electronics-tutorials.ws/diode/diode_3.html [Accessed: October 2018].

[16] Farag A. A. and Rafea M. A. 2010 *Synth. Met.* **160** 156.

[17] Mills C. A. *et. al* 2009 *Proc. of SPIE* **7449** 744911.

[18] Mark J. E. 1999 *Polymer Data Handbook*. (Oxford University Press, Inc.: New York).

[19] Hellborg R. *et al.* 2009 *Ion Beams in Nanoscience and Technology*. (Springer Verlag Berlin Heidelberg.: New York).

[20] Molapo K. M. *et al*. 2012 *Int. J. Electrochem. Sci*. **7** 11859.

[21] Banerjee S. 2011 PhD Thesis, Tezpur Uni. (Tezpur).

[22] Le T. H. *et al*. 2017 *Polymers* **9 (4)** 150.

[23] Bharti M. *et al.* 2018 *Prog. Mater. Sci.* **93** 270.

[24] Ates M. *et al.* 2012 *Curr. Phys. Chem.* **2** 224.

[25] Kumar F. *et al*. 2010 *Synth. Met.* **160** 1507.

[26] Kuo C. T. and Chiou W. H. *et al*. 1997 *Synth. Met*. **88** 23.

[27] Sharma I. D. *et al.* 2013 *Indian J. of Engineering Mater. Sci*. **20** 145.

[28] May T. *et al.* 2003 *Smart Mater. Struct.* **12** 626.

[29] Beverina L. *et al*. 2014 *Chem. Commun.* **50** 5413.

[30] Hall N. 2003 *Chem. Commun.* **7** 1.

[31] Gupta K. *et al.* 2010 *Synth. Met*. **160 (13)** 1566.

[32] Alvarez A. *et al.* 2011 *Trends in Analytical Chemistry* **30 (9)** 1513.

[33] Epstein A. J. 1997 *MRS Bulletin* **22** 16.

[34] Mzenda V. M. 2006 MSc Dissertation, Univ. of Pretoria (Pretoria).

[35] Rusu M. *et al.* 1998 *Appl. Surf. Sci.* **126** 245.

[36] Cheng Y. J. *et al*. 2009 *Chem. Rev.* **109 (11)** 5868.

[37] Heeger A. J. 2001 *Synth. Met.* **125** 23.

[38] Bott A. 1998 *Curr. Sep*. **17** 87.

[39] Rami S. 2015 MSc dissertation, Univ. of South Florida (Florida).

[40] Li B. *et al.* 2010 *J. Polym. Sci. Part B* **48** 2072.

[41] Tsukamoto J. *et al.*1990 *Jpn. Appl. Phys.* **29** 125.

[42] Tsukamoto J. 1992 *Adv. Phys*. **41** 509.

[43] Bredas J. L. and Street G. B. 1985 *Acc. Chem. Res.* **18** 309.

[44] https://www.researchgate.net/publication/241158731_Conduction_mechanism_in_electronic_polymers_Effect_of_morphology [Accessed: November 2018].

[45] Popok V. N. *et al.* 2012 *Rev. Adv. Mater. Sci*. **30** 1.

[46] Loh I. H. *et al.* 1988 *Nucl. Instrum. Meth. Phys. Res*. B **34** 337.

[47] Resta V. *et al*. 2014 *Nucl. Instr. Meth*. B **331** 168.

[48] Rao G. R. *et al*. 1994 *Surf. Coat. Technol*. **64** 69.

[49] MacDiarmid A. G. *et al*. 1985 *Molec. Cryst. Liq. Cryst*. **121** 173.

[50] Shaktawat V. *et al.* 2009 *J. Chem.* **7 (4)** 769.

[51] Yilmaz F. 2007 PhD Thesis, Middle East Technical Univ. (Ankara).

[52] Masters J. G. *et al.* 1991 *Synth. Met.* **41** 715.

[53] McCall R. P. *et al.* 1990 *Phys. Rev.* B **41** 5202

[54] Boeva Z. and Sergeyev V. G. 2014 *Polym. Sci.* C **56** 144.

[55] Fan J. *et al.* 1999 *Solid state communications* **110** 5762.

[56] Jozefowicz M. E. *et al.* 1989 *Phys. Rev.* B **39** 12958.

[57] Stafström S. *et al.*1987 *Phys. Rev. Lett.* **59** 1464.

[58] Bhadra R. S. *et al.* 2009 *Prog. Polym. Sci.* **34** 783.

[59] Kohlman R. *et al.* 1997 *Phys. Rev. Lett.* **78** 3915.

[60] Xia Y. *et al.* 1995 *J. Chem. Mat.* **7 (3)** 443.

CHAPTER 3: EXPERIMETAL TECHNIQUES

3.1. Introduction

Polyaniline films were formed on an ITO/PET substrate using a spin coater. Thereafter, an ion implanter was used to implant the PANI films with 50-keV Cu^+ ions to different fluences of $0.5x10^{16}$, $1.0x10^{16}$, $3.0x10^{16}$ and $5.0x10^{16}$ ions/cm^2 to form Cu^+-PANI nanocomposite films. SEM, XRD, RBS, FTIR, Raman spectroscopy, UV-Vis, PL and I-V techniques were used for the study of structural, optical and electrical characterization of the films before and after ion implantation. This chapter provides a brief discussion of these experimental techniques and how the samples were characterized.

3.2. Thin film preparation

Polymer thin films have been traditionally prepared using the doctor-blading technique if the target thickness is in the millimeter range [1, 2]. Chemical vapor deposition is used to deposit low boiling point organic molecules on various substrates [3]. In the case of ultrathin films, the Langmuir-Blodgett (LB) [4] and spin coating techniques [5] are two of the most frequently used methods. In this study, the spin coating technique was used to prepare the films.

3.2.1. Spin coating

Spin coating technique is widely used for the preparation of polymer thin films on a solid substrate such as glass, wafer and GaAs [6, 7, 8]. For this study, films were prepared on the ITO/PET substrates using a Smart Coater 100TM spin coater. A typical spin coating procedure starts by placing an excess amount of a solution on a substrate, which is then rotated at high speed (typically around 3000 rpm) in order to spread the solution evenly by centrifugal force. Centripetal acceleration makes the solution to spread to, and eventually off the edge of the substrate leaving a thin film on the surface. The final film thickness, coverage and roughness are influenced by factors such as molecular weight and concentration of the film-forming compound, the substrate, solvent type, and parameters (rotational speed and acceleration) chosen for the spin process [9, 10, 11]. For example, the final film thickness will be inversely proportional to the spin time and speed, as shown in Fig. 3.1.

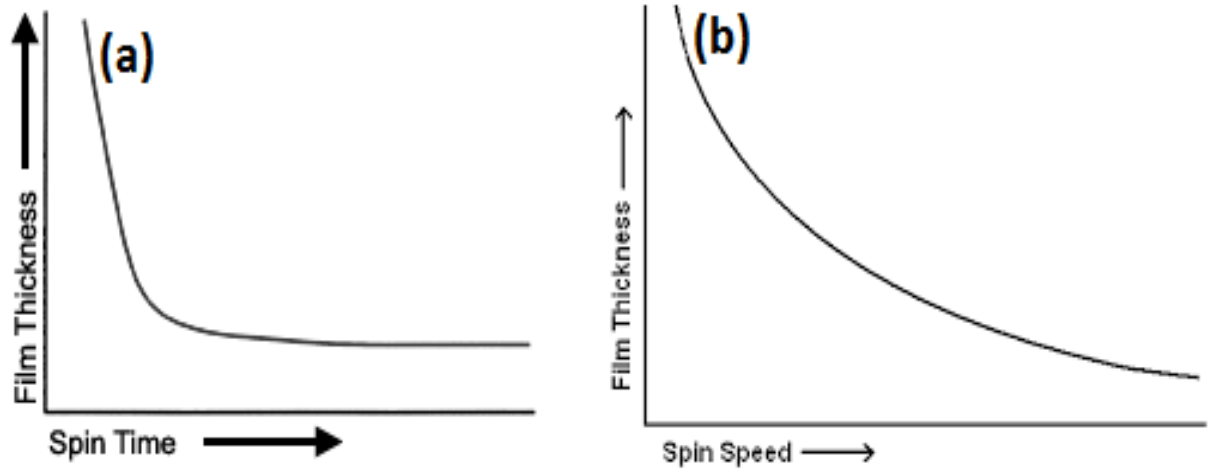

Figure 3.1: Film thickness versus spin time (a) and spin speed (b) [12].

Comparing it with other thin film-forming techniques, spin coating is not complicated, and films with uniform thickness and small surface roughness are produced by selecting proper preparation parameters like rotational speeds, time and solvent combination used. In addition, due to high

rotational speeds, the high flow leads to faster drying times of the films making this technique less time consuming [13].

3.3. Ion implantation

Ion implantation is a powerful surface or near-surface modifying technique used to alter electrical, structural, mechanical, optical and magnetic properties of the polymer films. In this technique, a beam of energetic ions interacts with the atoms/electrons of the polymer. A change in properties of the polymer can be studied as a function of fluence and a type of ions. The energy of the ions can also be varied to investigate a change in properties as a function of depth.

For this study, ion implantation was performed using the Varian-Extrion 200 – 20A2F model ion implanter with ES – 30/25C processing station (Fig. 3.2), located at iThemba LABS, Gauteng Province, South Africa. For dose determination, this instrument is equipped with a dose processor, which takes the electron flow from four corner cups and converts it into a dose.

In this technique, an energetic beam of ions of a particular atomic specie (Cu^+ ions in our case) is generated by making use of a hot cathode arc discharge ion source. These positively charged ions are generated by leaking a gas into a cylindrical chamber. When the gas molecules collide with the electrons, the gas molecules break apart into several different species of positively charged ions. A voltage difference of about 35 keV is applied between the source and extraction electrode (located just outside the chamber) to extract the ions from the chamber through electrical attraction between the two (i.e. source and the electrode). As the ions accelerate through the voltage differential, they gain energy and the energy of each ion equals to the charge of the ion, multiplied

by the voltage difference between the ion source chamber and the electrode. If the ions are doubly charged, the extraction energy will be twice the source voltage, and given [15] by:

$$E = qV \tag{3.1}$$

where E and q are the energy and charge of each ion, respectively, and V is the voltage difference between the ion source chamber and the electrode.

The ions leave the source as an ion beam and are passed through analyzer magnets to separate and select the ions that are desired for the implantation. This process (selection and separation of desired ions) is done by deflecting the beam into circular orbits. The amount of deflection is dependent on the atomic mass of a particular ion. The lighter ions are deflected into tighter orbits than the heavier ions. The selected ions are deflected through an angle of 90°, while the deselected ions are deflected through angles less or greater than 90° and get collected on the magnet chamber walls or on the resolving aperture plate. The ion beam is then passed through a variable slit that is located just after resolving aperture. This variable slit acts as an adjustment and it is used to control the intensity of the beam by opening or closing it. Prior to implantation, the ions are given final energy boost by passing the beam through an accelerator tube, entering the tube at high voltage (0 – 180 kV). Just after the accelerator tube, there are quadrupole lenses used to focus the beam into an oval shaped spot since the ion beam tends to diverge as the ions get attracted towards the exit.

The beam is then converged into an oval shaped spot and directed and scanned on to the surface of the target polymer film using electrostatic beam deflecting plates. This procedure is done such that the ions are implanted evenly across the surface of the implanted polymer in the target chamber. The target chamber is kept at a pressure of about $5x10^{-6}$ Torr. Ion implantation has unique advantages over other doping techniques in that: it is possible to control the depth of dopants by

varying or selecting suitable energy and dose of the implanting ions. In addition, any element in the form of ion can be imported into the polymer material [16].

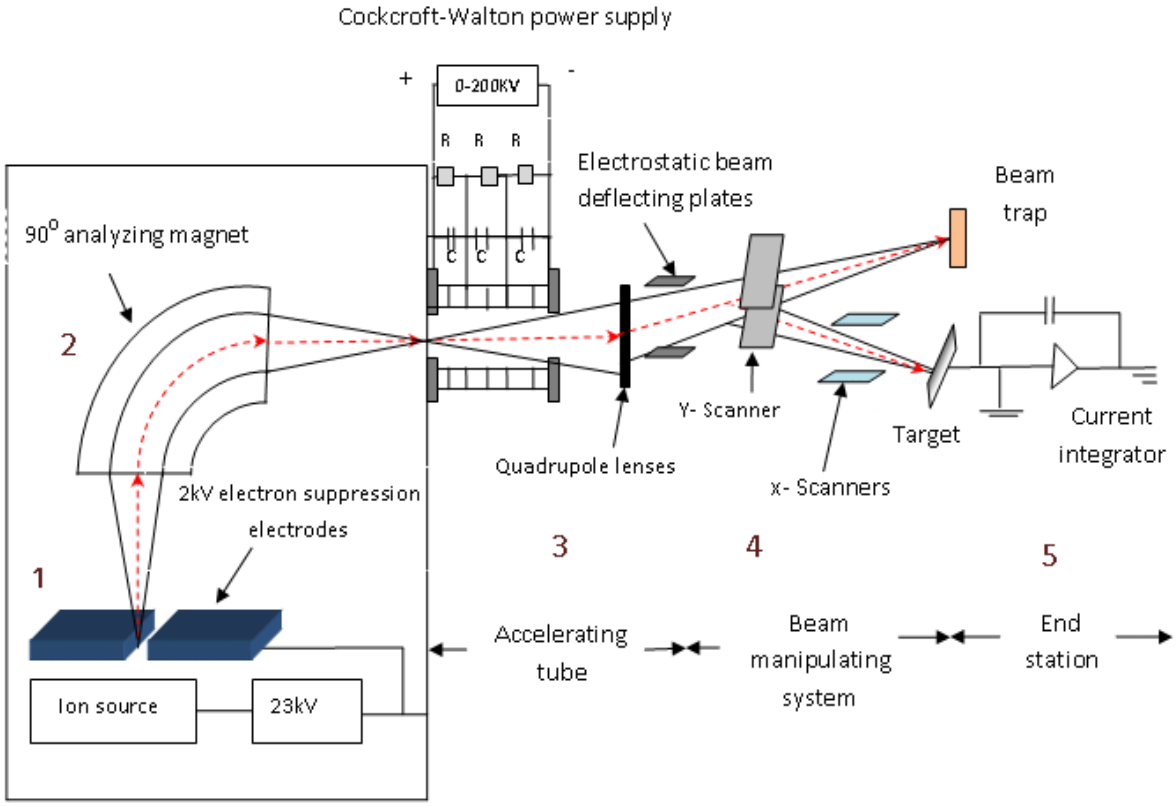

Figure 3.2: Schematic diagram for the Varian-Extrion 200 – 20A2F model ion implanter [14].

3.4. Material characterization techniques

Different material characterization techniques were used to investigate a change in structural, optical and electrical properties of the films due to ion implantation. The experimental set ups to characterize the samples are discussed in this section.

3.4.1. Rutherford Backscattering Spectrometry (RBS)

RBS technique is widely used for the surface or near-surface layer analysis of solid materials. This is a quantitative technique used for depth profiling of elements contained in the surface region of

a sample. In addition, the technique can be used to determine the thickness of thin films and multilayered structures, elemental ratio at any given depth in the film and elemental concentrations [17, 18]. This technique is based on the detection of charged particles that are scattered elastically by the nuclei of the analyzed sample atoms.

In this study, positively charged helium (He^{2+}) ions were used. The basic principle of this technique is that, a helium ion source is used to generate helium ions, which are negatively charged. The negatively charged ions are then accelerated (from ground to the positively charged terminal through electrostatic attraction) to high energies by applying high potential across the accelerator tube using a 6 MeV tandem accelerator (Fig. 3.4). Inside the accelerator, there is a striper gas which serves to remove electrons from the incoming negatively charged ions and change their charge state to positive. The (now) positively charged ions are accelerated to higher energies as they are repelled from the positive terminal voltage and back to ground potential. Just in front of the accelerator, there are dipole magnets that deflect the beam across various beam line.

The microprobe beam line 1 was used, as indicated in Fig. 3.4 for RBS measurements. The beam was focused and directed on to the sample (located inside the scattering chamber) using a combination of vertical and horizontal slits. When the beam (i.e., energy = 2 MeV) hits the target (PANI films in our case), the incident particles get scattered from the scattering centers of the material and the target atoms get recoiled at an angle, θ, with respect to the incident beam (Fig. 3.3). When only elastic collision is considered, the energy of the backscattered ions can be calculated using conservation of energy and momentum, given [15] by:

$$E = E_0 K \qquad (3.2)$$

where E is the energy of the backscattered particles, E_0 is the energy of the incident particles, and K is the kinematic factor, which is the ratio of the energy of incident ions after a collision to the projectile energy before a collision. The kinematic factor K is given [15] by:

$$K = \left[\frac{(M_2^2 - M_1^2 \sin\theta)^{1/2} M_1 \cos\theta}{M_1 + M_2}\right]^2 \quad (3.3)$$

where M_1 and M_2 are the masses of the incident ions and target atom, respectively and θ is the backscattering angle. It can be noticed from equation (3.3) that K is dependent on the mass of the incident ion (M_1), mass of the target atom (M_2) and the scattering angle (θ).

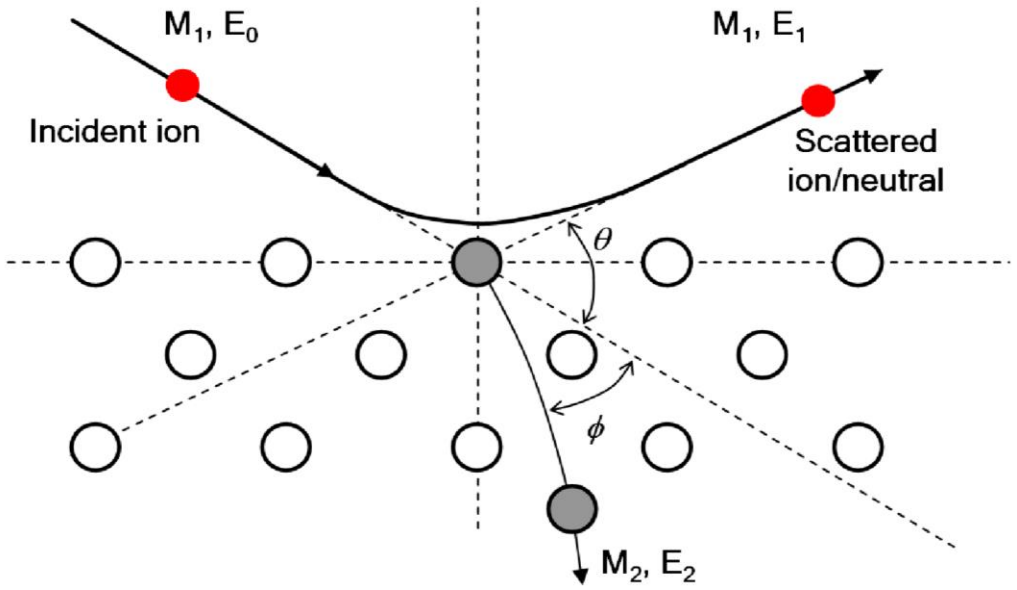

Figure 3.3: Schematic diagram of scattering trajectory of an incident ion [20].

The RBS detector in the microprobe chamber is positioned at an angle of 150^0 from the incident direction, and the beam struck the sample normally, i.e. $\theta = 150^0$ and $\alpha = 90^0$. The output charge signal (which is proportional to the energy of the backscattered ions) is fed into the pre-amplifier, where it is integrated and converted into a voltage signal. The amplifier and ADC (inside MCA) are used to amplify the voltage signal, and then convert it (amplified voltage signal) from analogue

to digital, respectively. On the computer screen, an RBS spectrum of counts (number of backscattered ions registered by the detectors) as a function of channel number (the energy of the detected backscattered ions) is displayed. Fig. 3.4 shows a floor plan of tandem accelerator, with Ion Beam Analysis (IBA) lines.

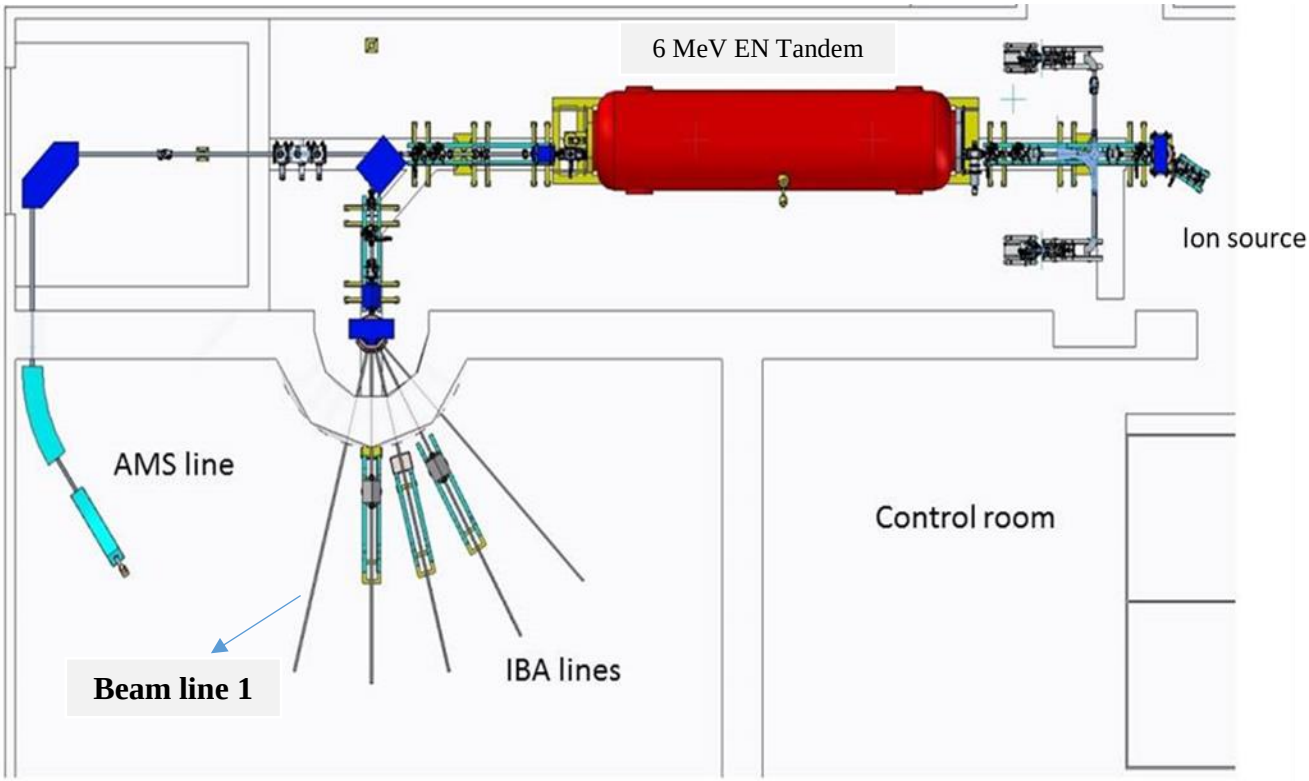

Figure 3.4: iThemba LABS, Gauteng Accelerator Vault floor plan [19].

3.4.2. X-Ray Diffraction (XRD)

X-ray diffraction technique is used for phase identification of crystalline material and to determine the structural properties such as grain size, lattice constants and degree of crystallinity of these phases. In addition, this technique is used to determine the thickness of the films and multilayers and also to determine the arrangements of atoms in amorphous material [15]. This technique is based on constructive interference of monochromatic X-rays diffracted by a crystalline sample. These X-rays are generated in a cathode ray tube by heating a tungsten filament (cathode) to

produce electrons. These electrons are then accelerated toward a target material (anode), usually made of copper by applying a potential difference. When electrons strike the anode, electrons from the K-shell (1s) of the anode material are ionized, resulting in the emission of K_β and K_α Cu X-rays with 1.39 and 1.54 Å wavelengths, respectively. A nickel filament, which absorbs wavelength below 1.5 Å is used to filter out the K_β radiation. The Kα X-rays are collimated and directed on to the sample. When the incident Kα X-rays interact with the sample, interference (both constructive and destructive) occurs [21]. As a result, diffraction occurs when the following conditions are met: (a) the wavelength of the X-rays must roughly be in the same order of magnitude as the atomic spacing in the material and (b) the scattering centers must be spatially distributed in a highly regular way [22]. The X-rays are reflected from a crystal only if the angle of the incident X-rays satisfies the Bragg equation, given [23] by:

$$n\lambda = 2d\sin\theta \tag{3.4}$$

where n is an integer, λ is the wavelength of X-ray used, d is the interplanar spacing between the planes in the crystalline phase and θ is the angle at which the constructive interference of X-ray beam occurs (Fig. 3.5).

The intensity of the X-ray is measured as a function of the diffraction angle, 2θ, and the orientation of the sample [23]. As the sample and detector are rotated, the intensity of the reflected X-rays is recorded, processed and converted into a diffraction pattern. This diffraction pattern is used to identify the crystalline phase and to measure structural properties of the samples. The X-ray diffractometer used in this study was SmartLab X-Ray Diffractometer with Cu-Kα radiation (λ = 1.54 Å) supplied by Rigaku.

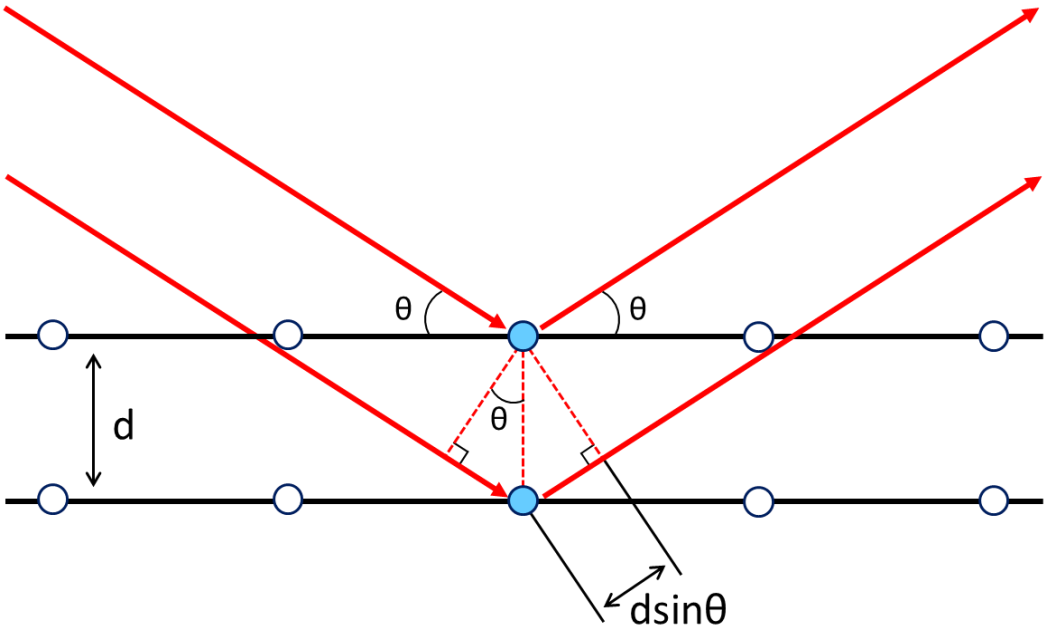

Figure 3.5: Schematic diagram showing diffraction according to Bragg's law [24].

3.4.3. Fourier Transform Infrared Spectroscopy (FTIR)

FTIR technique is used to determine vibrational frequencies of a molecule by measuring the absorption of light of certain energies that correspond to vibrational excitation of the molecules from lower to higher states [25]. This technique is widely used to determine the absence or presence of certain functional groups in a molecule. In addition, this technique is also used to identify unknown materials, to investigate the extent of hydrogen bonding (intra- and inter molecular hydrogen bonding) and conformational orientation of molecules [26].

In this technique, infrared radiation light is directed on to the sample (Fig. 3. 6). Some of the infrared light is absorbed by the sample, while some penetrate through the sample. The resulting signal at the detector is an infrared spectrum representing a molecular "fingerprint" of the sample [26]. The infrared spectrum is a plot of the ratio (between intensity before and after the light interacts with the sample) versus the frequency or wavenumber. The infrared spectrum is

commonly plotted in one of three formats: as transmittance, reflectance or absorbance versus frequency or wavenumber. The absorption peaks represent the frequencies of vibrations between the bonds of the atoms making up the sample material. For this study, the FTIR analysis were carried out using a Vertex 70 Sample Compartment RT-DLaTGS spectrometer supplied by Bruker. Fig. 3.6 shows a simplified layout of FTIR spectroscope.

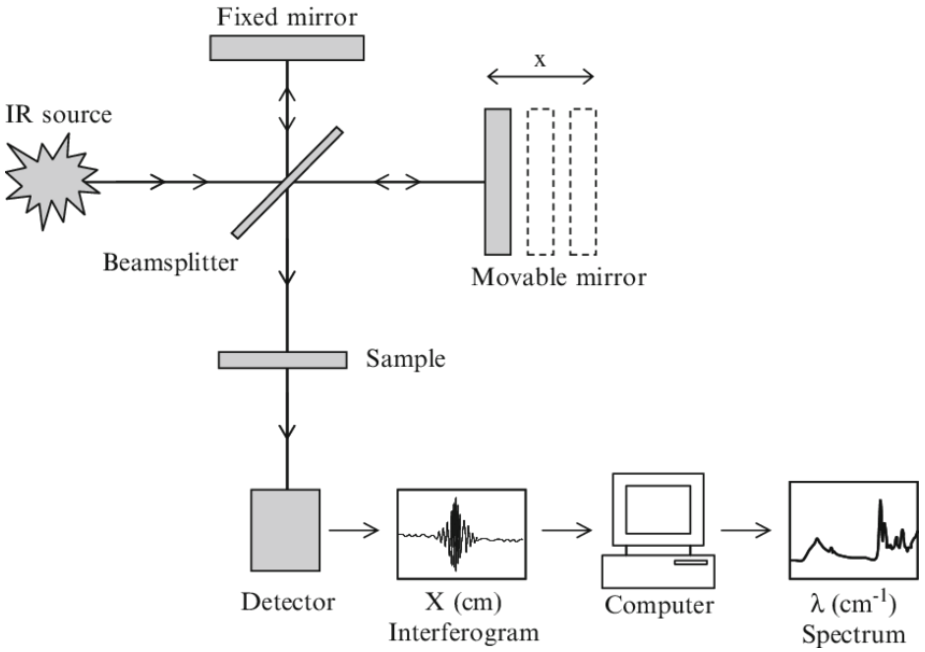

Figure 3.6: Schematic diagram of a typical Fourier-transform-infrared-FTIR set-up [27].

3.4.4. Raman Spectroscopy

Raman spectroscopy is a complementary technique to FTIR technique and is used to determine vibrational frequencies of molecules. However, Raman spectroscopy is different from IR spectroscopy in that: the technique is more sensitive to the lengths, strengths, and arrangement of bonds in a material than it is to the chemical composition like in IR spectroscopy [26, 28]. In addition, Raman spectrum arises from an indirect coupling of high-frequency radiation (usually visible light, also UV and near infrared) with the electron clouds that make up the chemical bonds [26].

In this technique, an intense monochromatic light beam is directed on to the sample. When the light interacts with the sample, the electric field of the beam distorts the electron cloud that makes up the chemical bonds in the sample. As a result, some of the energy of the incident radiation gets stored. When the field reverses as the wave passes, the distorted electron cloud relaxes, and the distorted energy is re-radiated. Most of the stored energy is reradiated at the same frequency as that of the incident exciting light. This component is referred to as Rayleigh scattering [27]. However, a small portion of the stored energy is transferred to the sample itself, leading to the excitation of the vibrational modes. The vibrational energies are deducted from the energy of the incident beam and weak side bands appear in the spectrum at frequencies less than that of the incident beam. These are called Raman lines. Their separation from the Rayleigh lines is a direct measure of the vibrational frequencies of the sample [26, 29]. For this study, all the Raman spectra were collected using the XploRa PLUS Raman Microscope.

3.4.5. Scanning Electron Microscopy (SEM)

SEM is a powerful surface technique used to investigate surface morphology of molecules and mapping. This technique provides a large depth of field, which means, the area of the sample that can be viewed in focus at a time is quite large [30]. The basic principle of SEM is that, an electron gun is used to produce electrons, these thermos-electrons are emitted from a filament (cathode) made of a thin tungsten wire (~ 0.1 mm) by heating the filament to a high temperature (~ 2800 K). These thermo-electrons are gathered together as an electron beam and the beam is accelerated towards a metal plate (anode) by applying a positive voltage (1 – 30 kV) to the anode. The electron beam is then passed through an aperture and a system of lenses (condenser and objectives lenses) to focus and produce a very thin beam of electrons (1 – 5 nm) [31]. Along the path, the deflection

coils inside the objective lens controlled by the scanning generator deflect the electron beam few times. The beam scans over the surface of the sample in a predetermined pattern such as raster pattern. When the primary electrons interact with the atoms on the surface of the sample, secondary electrons (having kinetic energies much lower than the primary incident electrons) are emitted, amplified, collected by the secondary electron detector and converted into an image. The backscattered electrons of the electron beam may also be detected. These backscattered electrons are used for contrasting the sample regions, having different chemical composition on the surface [32].

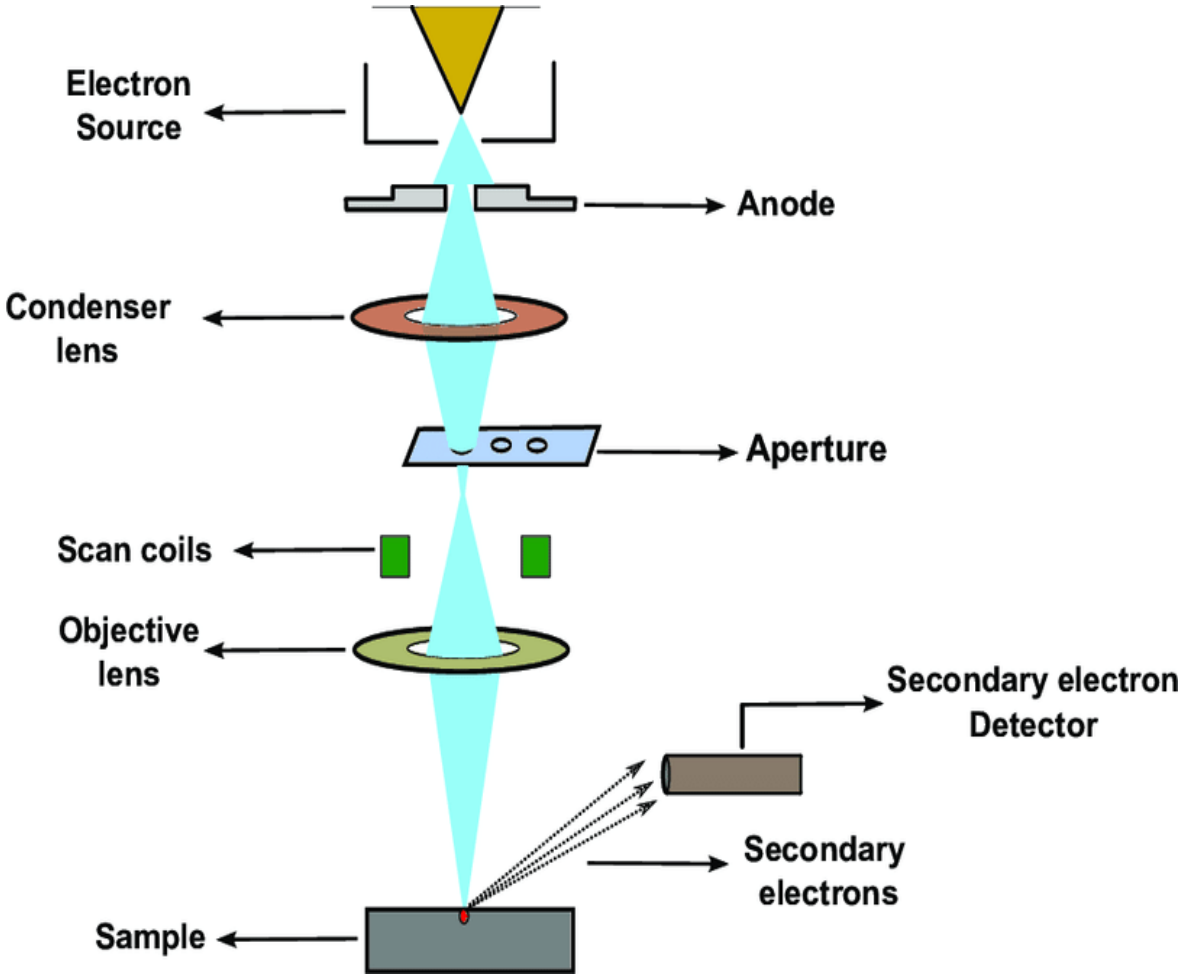

Figure 3.7: Schematic representation of a SEM setup [33].

SEM micrographs of PANI film in this study were obtained using the JEOL JSM 7800F Field Emission Scanning Electron Microscope (FE-SEM) equipped with an Energy Dispersive X-ray spectrometer (EDS) which is used for elemental analysis and to observe how elements are distributed in a microscopic region on the surface of the specimen. Fig. 3.7 shows a simplified layout of SEM instrument.

3.4.6. UV-Visible spectroscopy (UV-Vis)

UV-Vis spectroscopy is a powerful technique used to study the optical properties of a material. For this study, the UV-Vis data were acquired using a double beam Perkin-Elmer Lambda 1050 UV/VIS/NIR spectrometer equipped with an integrating sphere and an interchangeable sampling module. In addition, the spectrometer is equipped with deuterium (D2 lamp) and tungsten halogen (W lamp) light sources, as shown in Fig. 3.8. Comparing the two light sources in terms of their wavelengths, deuterium light has wavelength ranging from 10 to 400 nm, while the wavelength of tungsten halogen light is greater than 3000 nm. These two lamps are used to irradiate the sample, with the deuterium lamp used to irradiate the sample in the ultraviolet region from 200 to 400 nm and then shift to the tungsten lamp, which is a continuous wavelength output from about 400 to 3000 nm.

In this technique, the sample is placed in an integrated sphere, which is used to collect the diffusely scattered light. Prior to sample irradiation, a beam of light from a visible and/or UV light source is split into two beams of equal intensity by a half-mirrored device. One (colored blue) is sent directly to the detector as a reference beam, while the other is directed on to the sample (colored red), as shown in Fig. 3.8. The intensity of the reference and sample beams are defined as $\mathbf{I_0}$ and **I**. When the sample beam passes through a sample, it gets absorbed and its intensity is reduced to

less than that of reference beam (i.e. $\mathbf{I} < \mathbf{I_0}$). The spectrometer is programmed internally to plot a graph of this difference in intensity versus wavelength. Absorption may be presented as transmittance ($\mathbf{T} = \mathbf{I}/\mathbf{I_0}$).

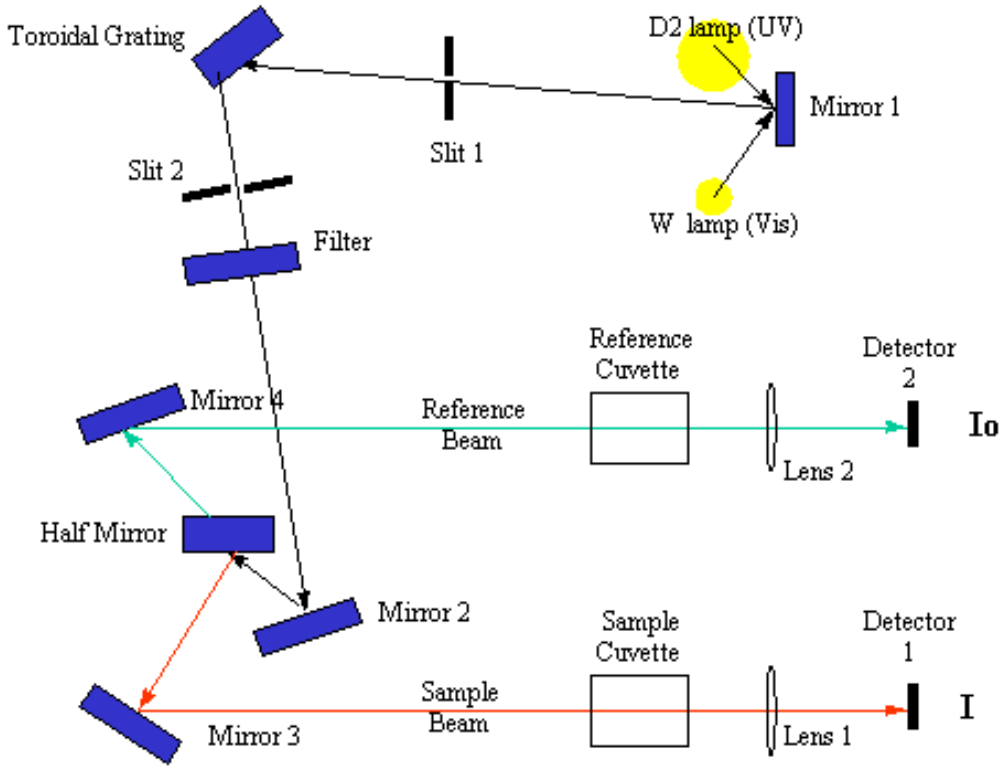

Figure 3.8: Schematic diagram showing components of a typical UV-Vis spectrometer [34].

The data acquired from this technique can be used to calculate bandgaps (direct and indirect band gaps) of the films by plotting a graph of absorption coefficient, α, against the incident photon energy *hv*, which are related by Tauc relation [35, 36] as:

$$(\alpha h\nu) = A\left(h\nu - E_g\right)^n \qquad (3.5)$$

where A is a constant that depends on the properties of the material, E_g is the optical band-gap and n is a constant that can take different values depending on the type of electronic transition. For allowed direct transitions, n = ½; forbidden direct transitions, n = 3/2; allowed indirect transitions,

n = 2; and for forbidden indirect transitions, n = 3 [37]. For this study, n was chosen to be 1/2 since the transition in polyaniline is direct [38]. This means that the transition involves a change in potential energy only. The direct band gap values of the films were estimated by plotting a graph of $(\alpha h\nu)^2$ versus $(h\nu)$, where the values of E_g were obtained by extrapolating the straight-line portion of the graph of $(\alpha h\nu)^2$ against $(h\nu)$. The intercept of the tangent to the *x*-axis gave the values of the indirect band gap of the PANI films.

3.4.7. Photoluminescence Spectroscopy

Photoluminescence spectroscopy technique is used to study the optical and electronic properties of materials. In this technique, a laser, xenon lamp or synchrotron radiation is directed on to a sample, and the sample will absorb this electromagnetic radiation. If the electromagnetic radiation has enough energy to excite electrons from valence band to conduction band, a process called photoluminescence occurs [39, 40]. The system then undergoes a non-radiative internal relaxation involving interaction with crystalline or molecular vibrational and rotational modes. The excited electron moves to a more stable excited level, such as the bottom of the conduction band or the lowest vibrational molecular state. After a system-dependent characteristic lifetime in the excited state (which may last for about picoseconds to many seconds), the electronic system will return to the ground state. In luminescent materials, some or all the energy released during this final transition is in the form of light, in which the relaxation is said to be radiative [26]. The emitted light is then detected as photoluminescence and this PL spectroscopy is based on detecting and characterizing the properties of this light. A photomultiplier tube (PMT) is used to detect the emission of the light, and the light signals get processed and converted into an emission spectrum, which is a plot of PL intensity as a function of wavelength of the emitted light. For this study, all

PL spectra were collected using Fluorolog Horiba Jobin Yvon (model No. FL-1057) equipped with 450W xenon lamp as an excitation source, as shown in Fig. 3.9.

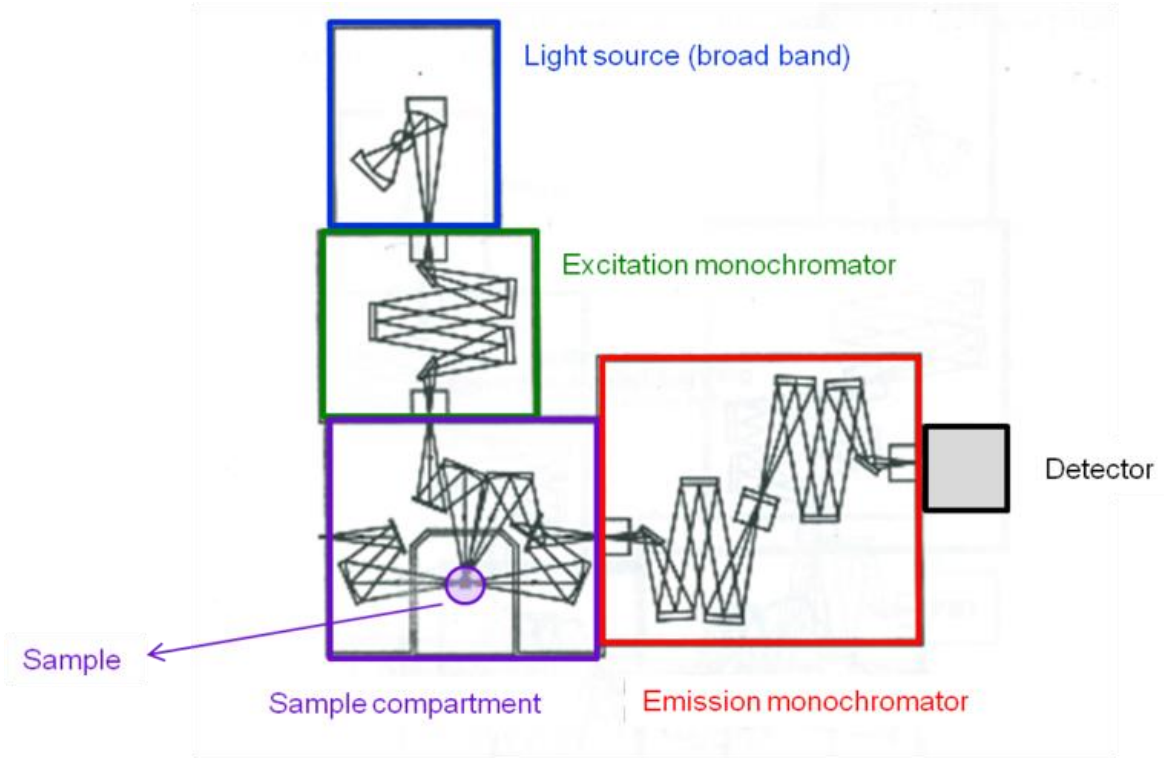

Figure 3.9: Schematic diagram of HORIBA FluoroLog-3 Spectroflurometer [41].

3.5. Device Fabrication and Characterization

3.5.1. Device fabrication

To investigate how doping altered the electrical properties of the films, contacts were made on unimplanted and metal-doped PANI films as follows: one of the electrodes was the anode sitting on the ITO (electrode connected to brown wire), while the other electrode was the cathode, sitting on the polyaniline (electrode connected to green wire), as shown in Fig. 3.9. Each electrode was sitting on aluminium sheet (~ 0.34 x 0.34 cm^2 and thickness of about 0.025 cm) to avoid scratching of the films since the electrodes have sharp ends. The resistance of the sheet was measured using

multimeter to be low (0.35 Ω) to have no impact on the measured current. The separation between the two electrodes was approximately 10 mm and was maintained throughout the measurement. Measurements were carried out at different separations during set-up. The results showed that the separation distance did not affect the data/measurements. The separation of 10 mm was enough to avoid, for instance, the aluminium sheet for cathode to make contact in the ITO (anode). Fig. 3.9 shows (a) the contacts that were made and (b) the schematic diagram of the contacts. It has to be noted that a sample stage shown in Fig. 3.9 (a) was built in-house specifically for our samples.

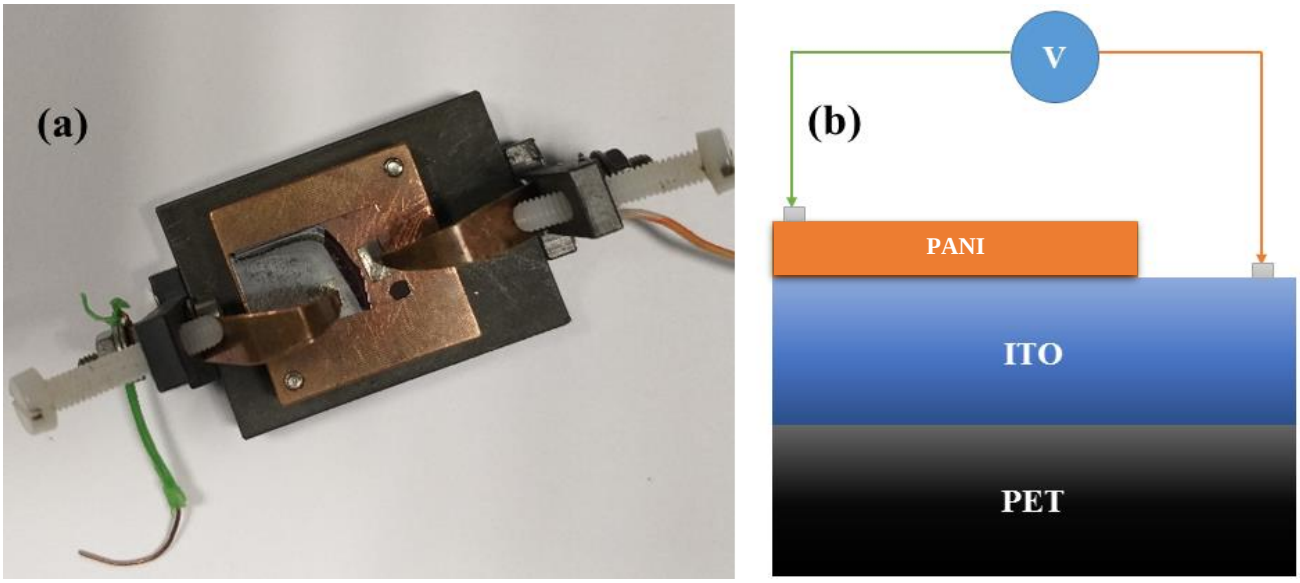

Figure 3.10: Construction of contacts to extract electrical properties of the films, with the sample stage (a) and the diagram indicating composition layer and contacts (b).

3.5.2. Current-Voltage (I-V) measurements

The current-voltage characteristics were investigated using a Keithley 6487 picoammeter with the built-in voltage supply. The experimental setup was as follows: the samples were placed on the sample stage and loaded into the high resistance test fixture. The samples on the stage were enclosed in the fixture in order to minimize the effects of surrounding light. Thus, the measurements were carried out in the dark. A picoammeter was used to apply the voltage to the

ITO electrode (connected to the brown wire) and measuring a resulting current from the PANI/Cu^{+}-PANI electrode (connected to the green wire), as shown in Fig. 3.6. The picoammeter was operated in the remote mode by connecting it to a personal computer through an RS-232 cable. An add-in utility for Microsoft Excel was installed in the computer for control of the picoammeter and for data acquisition [42]. The output signal is then converted and displayed as columns of current (I) and voltage (V).

For this study, the measurements were recorded in the voltage range -0.4 to +0.4 V. The measurements were conducted at room temperature (305 K), with a voltage step of 0.01 V and current limit was set to 2.5 mA. An option of a higher current limit (of 20 mA) that our equipment can reach was not available on the program. The time between the measurements was set at 1 second; a time determined after many trials [43] and intended to allow for the current to settle so that a more realistic value is acquired.

3.6. References

[1] Song H. H. and Wang C. S.1993 *Polym.* **34** 4793.

[2] Goswamy A. 1996 *Thin Film Fundamentals.* (New Age International.: Bristol).

[3] Martin T. P. *et al*. 2007 *Surf. Coat. Technol.* **201** 9400.

[4] Roberts G. *et al.* 1990 *Langmuir–Blodgett Films.* (Plenum Press.: New York).

[5] Lawrence C. J. 1988 *Phys. Fluids* **31** 2786.

[6] Yada T. 1998 *Jpn. J. Appl. Phys.* **37** 2752.

[7] Cecchi M. *et al*. 2001 *Synth. Met.* **121** 1715.

[8] Jeong S. *et al*. 2004 *Thin Solid Films* **466** 204.

[9] Lawrence C. J. 1988 *Phys. Fluids* **31** 2786.

[10] Hall B. D. *et al*. 1998 *Polym. Eng. Sci*. **38 (12)** 2039.

[11] Perlich J. *et al.* 2009 *Macromolecules* **42** 337.

[12] Bartczack Z. *et al*. 1999 *Polymer* **40** 2369.

[13] Song J. *et al*. 2009 *Thin Solid Films* **517** 4348.

[14] https://www.researchgate.net/figure/Block-diagram-for-the-200-20A2F-ion-implanter_fig9_323486262 [Accessed: December 2018].

[15] Verma H. R. 2007 *Atomic and Nuclear Analytical Methods*. (Springer-Verlag Berlin.: Heidelberg).

[16] Li B. *et al*. 2010 *J. Polym. Sci.* **48** 2072.

[17] Tesmer J. R. and Nastasi M. 1995 *Handbook of Modern Ion Beam Analysis.* (Material Research Society.: Pittsburgh).

[18] Feldman L. C. and Mayer J. W. 1986 *Fundamentals of Surface and Thin Film Analysis.* (Elsevier Science Publishing Co.: Amsterdam).

[19] https://tlabs.ac.za/Gauteng_new/RefurbSite/pdfs/iThemba%20Brochure.pdf [Accessed: December 2018].

[20] https://warwick.ac.uk/fac/sci/physics/current/postgraduate/regs/mpagswarwick/ex5/techniques/structural/ionscattering/ [Accessed: January 2019].

[21] Cao G. 2004 *Nanostructures and Nanomaterials: Synthesis, Properties & Applications*, 6th edition. (Imperial College Press.: London).

[22] Cullity B. D. 1978 *Elements of X-Ray Diffraction*, 2nd edition. (Addison-Wesley Publishing Co. Inc.: Boston).

[23] James A. *et al*. 1998 *Residual Stress Characterization of Welds Using X-Ray Diffraction Techniques*.

[24] https://www.researchgate.net/figure/Braggs-law-A-two-dimensional-crystal-lattice-and-a-set-of-imaginary-planes-is_fig10_47418334 [Accessed: February 2019].

[25] Gauglitz G. *et al.* 2003 *Handbook of Spectroscopy.* (WILEY-VCH Verlag GmbH & Co. KGaA.: Weinheim).

[26] Brundle C. R. *et al.* 1992 *Encyclopedia of Materials Characterization*, 1st edition. (Butterworth-Heinemann.: Oxford).

[27] https://www.researchgate.net/figure/Schematic-sketch-of-the-essential-features-of-a-Fourier-transform-infrared-FTIR_fig1_225065938 [Accessed: March 2019].

[28] Harris D. C. *et al.* 1978 *Symmetry and spectroscopy: an introduction to vibrational and electronic spectroscopy.* (Oxford University Press.: Oxford).

[29] Herzberg G. *et al.* 1991 *Molecular Spectra and Molecular Structure II: Infrared and Raman Spectra of Polyatomic Molecules*. (Krieger Publishing.: Florida).

[30] Postek M. T. *et al.* 1980 *Scanning Electron Microscopy: A Student's Handbook*. (Ladd Research Ind., Inc.: Williston).

[31] Eberhart J. P. 1991 *Structural and Chemical Analysis of Materials*. (John Wiley & Sons.: Chichester).

[32] Goldstein J. *et al.* 2003 *Scanning Electron Microscope and X-Ray Microanalysis*. (Kluwer Academic/Plenum.: New York).

[33] https://www.researchgate.net/figure/SEM-probe-movement-model-and-operating-principle_fig26_281499535 [Accessed: March 2019].

[34] https://www2.chemistry.msu.edu/faculty/reusch/virttxtjml/spectrpy/uv-vis/uvspec.htm [Accessed: March 2019].

[35] Das M. *et al.* 2017 *Ceramics International* **43** 11123.

[36] Hossain F. *et al.* 2008. *J. Phys. Chem. Solids* **69** 1820.

[37] Adachi M. *et al.* 2007 *Curr. Nanosci*. **3** 285.

[38] Abdulla H. S. *et al.* 2012 *Int. J. Electrochem. Sci.* **7** 10666.

[39] Fox A. M. 2010 *Optical properties of solids*, 2nd edition. (Oxford University Press.: New York).

[40] Bordo G. V. *et al.* 2005 *Optics and spectroscopy at surfaces and interfaces*. (Wiley-VCH.: Weinheim).

[41] https://biophy.uchicago.edu/fluorescence.php [Accessed March 2019].

[42] Moloi S. J. and McPherson M. 2009 *Physica B* **404** 2251.

[43] Moloi S. J. 2005 MSc Dissertation, University of KwaZulu-Natal (Durban).

CHAPTER 4: FILM PREPARATION AND IMPLANTATION

4.1. Film preparation

4.1.1. Materials

Polyaniline (average M_W = 50, 000 a.m.u) in the form of emeraldine base (EB), Dimethyl Sulfoxide (DMSO) and Indium Tin Oxide coated PET (surface resistivity 60 Ω/sq, L x W thickness 31 cm x 31 cm x 5 mil, sheet) were obtained from Sigma Aldrich and were used as received.

4.1.2. Solution preparation

0.2 gram of powdered polyaniline was dispersed in 19.8 ml of Dimethyl Sulfoxide (DMSO) solvent to make 20 grams of PANI-DMS suspension. The suspension was prepared at room temperature and was then placed in an ultrasonic bath (model: UBM8 and operating voltage: 220 AC, 50 Hz) to further enhance the breakdown of polyaniline and dispersion in the solvent. The following parameters were set on the ultrasonic bath:

- Temperature = 45 °C,
- Power (%) = 100, and
- Time = 60 minutes.

4.1.3. Substrate cleaning

A blue plastic that was used to protect ITO side of the substrate from dust and getting scratched was removed. Thereafter, a pair of scissors was used to cut the polymer substrates into square shapes of about 30 x 30 mm^2. A typical procedure for substrate cleaning was as follows: first, the ITO/PET substrates were immersed in a beaker containing acetone and the beaker was placed in an ultrasonic bath for 15 minutes in order to remove the organics from the ITO side. Thereafter, the substrates were cleaned ultrasonically in a beaker containing methanol for 15 minutes to remove the acetone residues on the substrates. Finally, the substrates were rinsed ultrasonically in de-ionized water (DI) for 15 minutes to remove methanol residues. The substrates were dried using compressed nitrogen.

4.1.4. Deposition of polyaniline on the substrates

Polyaniline thin films were deposited on a well-cleaned ITO-PET substrate using a spin coater, at room temperature. First, a syringe was used to suck out the PANI-DMS solution from the beaker and pass it through sterile syringe filter (Corning, NY 14831, SFCA 0.20 µm) to filter out polyaniline agglomerates. This filter can only allow particle of size 0.20 µm and less to pass through. Then, a large drop of filtered PANI-DMS solution was put on the substrates (ITO side of the substrate, which is conducting) and warmed up to 78.9 °C for 10 minutes using a 0.5 kW lamp in an open heat box, and thereafter placed in the spin coater for coating, as illustrated in Fig. 4.1.

Figure 4.1: Steps followed in preparation of the films.

Table 4.1 gives the parameters that were used to achieve the final polyaniline films. The centering time was kept constant at one second. For spin coating, the rotational speeds were incremented between 100 and 1000 rpm. Finally, a large area of the substrate was covered. Spun films were left for drying at room temperature over night and this further drying process was found not to have effect on the final thickness and uniformity of the films.

Table 4.1: Selected film preparation parameters.

Spin speed (rpm)	Spin time (s)	Acceleration (rpm/s)
100	60	50
150	60	50
200	30	50
300	30	100
400	30	100
500	30	100
1000	30	100

4.2. Implantation of the films

The prepared thin films were implanted with 50-keV Cu^+ ions to different fluences to form Cu^+-PANI nanocomposite films. Implantation was carried out at cryogenic temperature to suppress radiation damage to the films. The current used during implantation was 2μA. Table 4.2 lists the names of the prepared samples and the implantation fluences that were used.

Table 4.2: Names of the prepared samples corresponding to the implantation dose used.

Sample name	Implanting dose (x10^{16} ions/cm^2)
A_1	Unimplanted (control sample)
A_2	0.5
A_3	1.0
A_4	3.0
A_5	5.0

CHAPTER 5: RESULTS AND DISCUSION

5.1. Material characterization

This section presents and discuses the results obtained from the different material characterization techniques. Techniques used to study the structural properties are SEM, XRD, RBS, FTIR, RAMAN spectroscopy while UV-Vis and PL techniques were used for optical properties of the material.

5.1.1. Scanning Electron Microscopy

Fig. 5.1 shows SEM micrographs of spin coated PANI film on ITO/PET substrate at different magnification levels of x16000 (Fig. 5.1-a) and x40000 (Fig. 5.1-b). At lower magnification level, nanoparticles of polyaniline are spherical in shape and are in-homogeneously distributed over the surface. The size of the particles was estimated by the use of ImageJ software. The particles have different diameters, varying from about 7.0 to 269 nm, as shown in Fig. 5.1-c. Large particle size may be attributed to agglomeration between two or more nanoparticles. The average particles diameter “d” was found to be 194 nm and can be compared with the values that are obtained in the literature [1].

The observed spheres coalesced into clusters and are interconnected to each other (Fig.5.1-a). Higher magnification shows that these spherically shaped nanoparticles are agglomerated into the bulk. Since the nanoparticles have relatively large sizes, this suggests that the prepared film could

provide large area for surface related applications. Moreover, since the nanoparticles are not homogenously distributed on to a smooth layer, this could mean that the specific area of the film is high enough to provide the film with more reactive centers to contact with electrodes to facilitate the charge transfer in the bulk of the film [2]. Different types of morphologies has been reported before with similar spherically shaped nanoparticles [1].

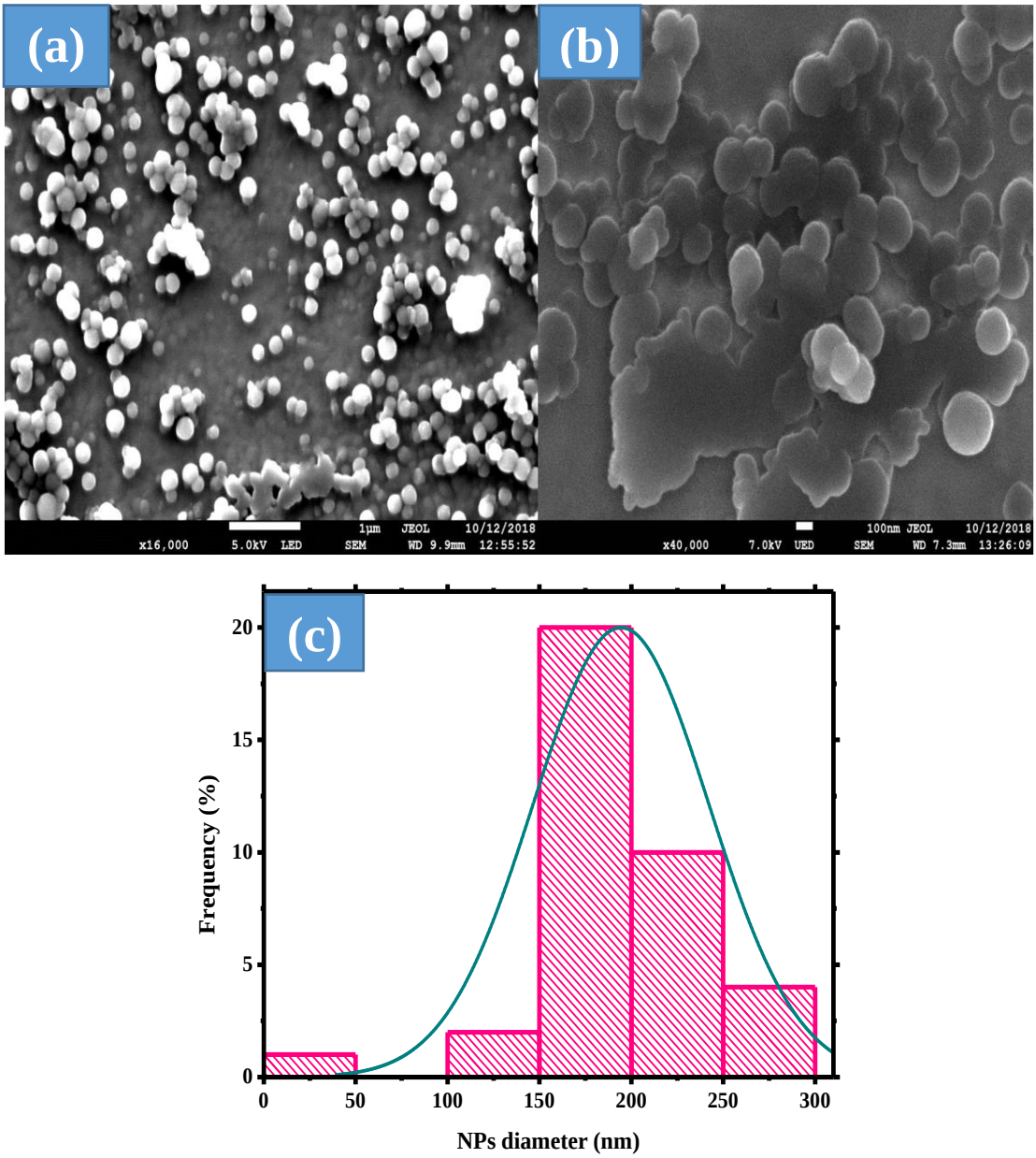

Figure 5.1: SEM micrographs at magnification levels of 16000 (a) and 4000 (b) and particle size distribution histogram (c) of PANI nanoparticles.

Fig. 5.2 shows the energy dispersive X-ray spectroscopy (EDS) spectrum of PANI film spin coated on ITO/PET substrate. The elemental composition of the prepared film is listed in Table 5.1. The spectrum and the table confirm the presence of all the expected elements; (carbon (C) and nitrogen (N)) present in polyaniline, as well as the elements in the ITO/PET substrate. C and N peaks in the EDX spectrum confirm the presence of PANI molecules and the successful preparation of the polymer on the ITO/PET substrate.

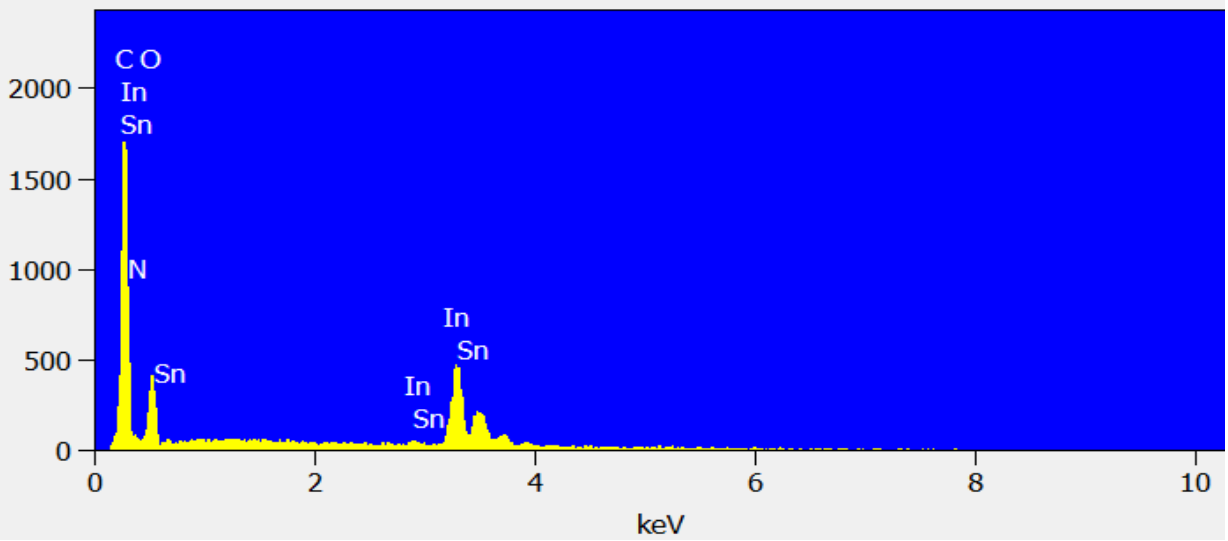

Figure 5.2: Selected area EDX spectrum of polyaniline layer spin coated on ITO/PET substrate.

It is expected that the peak for hydrogen (H) element, present in polyaniline would not appear in the spectrum. This is because hydrogen atom only has one electron in its shell, and therefore ionization results in the depletion of its electronic system. Characteristic X-ray emission therefore is not possible since the ionization of a hydrogen atom only results in the formation of a proton. The lightest element that can be traced using this technique, therefore, is lithium [3, 4]. This is because lithium has three electrons in its orbit, with one being in the upper (L) shell. The ionization of its K-shell therefore allows for a de-excitation process to take place, where characteristic X-ray are produced, and these X-rays are the ones that are being detected by the detector used in EDX.

Table 5.1: Selected area EDX results of the prepared PANI film.

Element Line	Weight %	Norm. Wt.%	Atom %	Formula	Compnd %	Norm. Compnd%
C K	38.4	38.4	66.0	C	38.4	38.4
N K	3.2	3.2	4.7	N	3.2	3.2
O K	11.9	11.9	15.3	O	11.9	11.9
In L	16.8	16.8	8.8	In	16.8	16.8
Sn L	29.7	29.7	5.2	Sn	29.7	29.7
Total	100.0	100.0	100.0		100.0	100.0

The analyzed volume gives 38.4% C, 3.2% N, 11.9% O, 16.8% In and 29.7% Sn elemental compositions (Table 5.1). As observed from Fig. 5.2, the peak of carbon has higher intensity than other elements. This high intensity of carbon peak may be due to the combination of carbon from polyaniline, carbon from the PET on the substrate and the carbon from the carbon tape that was used for sticking the films on the sample holder during EDX measurements. The main limitation of EDX here is that there is no depth profile information accessible.

5.1.2. X-ray Diffraction

XRD pattern of spin coated polyaniline film is presented in Fig. 5.3, in the 2θ range of 15° - 90°. The figure shows the XRD pattern of PANI with a broad characteristic peak centered at around 2θ = 18^0 - 25°. The observed broad peak may be attributed to the diffraction from planes resulting due to periodicity parallel and perpendicular to the direction of polyaniline chain, indicating the predominant amorphous structure of the polyaniline chain [5]. The observed pattern is in good agreement with the XRD pattern of polyaniline, which is reported in JCPDS number 53 – 1891 [2]. The absence of a sharp peak indicates that the prepared PANI films are amorphous in nature. Similar observation has also been reported by other workers [6] for PANI before.

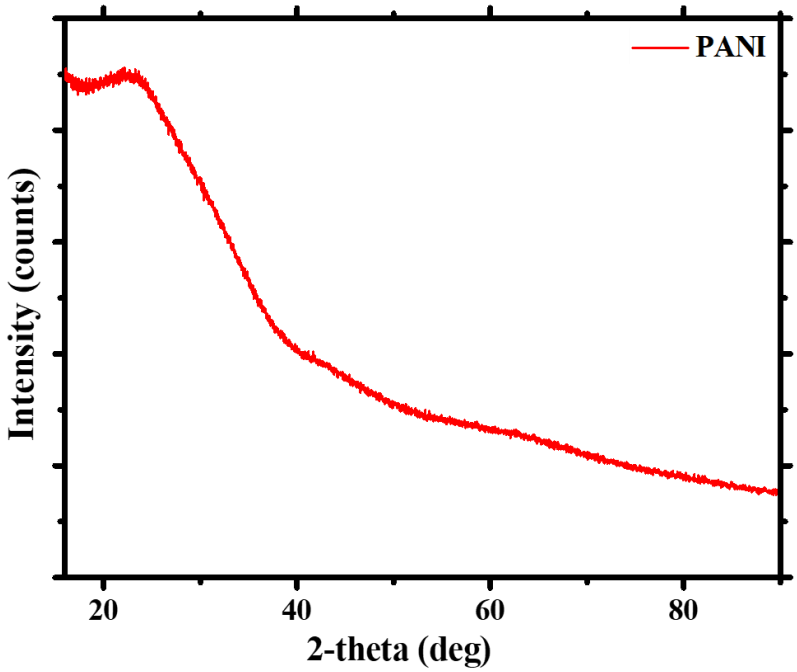

Figure 5.3: XRD pattern of unimplanted PANI.

5.2.3. Rutherford Backscattering Spectroscopy

Rutherford Backscattering Spectroscopy has been used to determine the thickness of the unimplanted PANI layer on the substrate and establish the presence of other elements in the sample. The spectrum was analyzed using SIMNRA simulation software [7]. Calibration was performed using a standard sample made of carbon as a substrate, containing oxygen, aluminum, nickel and gold. For standard sample, energy of the scattered ions was calculated using known kinematic factors from SIMNRA [7]. A graph of energy of scattered ions as a function of channel numbers was plotted and the graph was found to be linear, as shown in Fig. 5.4. When simulating the experimental RBS spectrum, the best fit (Fig. 5.5) was obtained with the following fitting parameters:

- y-intercept/calibration offset = -15.3 keV
- Slope/energy per channel = 5.70 keV/ch

- Number of incident particle = 1.3×10^{11}

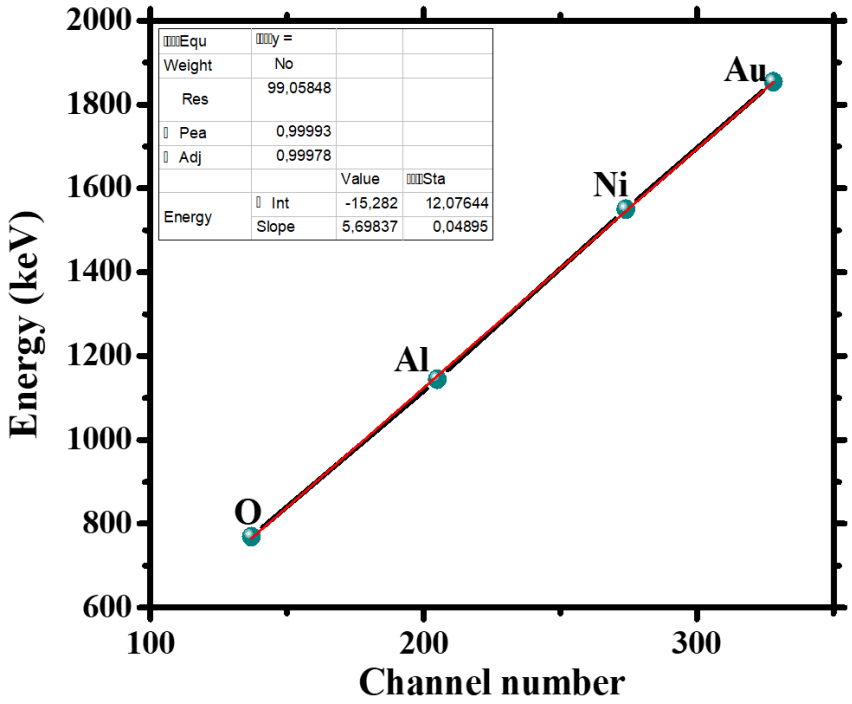

Figure 5.4: Energy of scattered ions as a function of channel numbers.

Fig. 5.5 shows experimental RBS spectra for 2 MeV He^{2+} ions scattered from the unimplanted PANI sample. As can be seen from the figure, simulated spectrum (blue) has been successfully overlapped on experimental spectrum (red). As shown from the figure, peak of Indium and Tin is well pronounced and broad. This is an indication that layer 2 (ITO) is quite thick. It is expected that Hydrogen peak would not appear on the spectrum because of the relatively low value of the backscattering cross-section for Hydrogen element and the fact that the energy of a particle will be low when it is backscattered from the Hydrogen atom [8]. Moreover, polyaniline consists of relatively small concentration of Nitrogen, hence the peak is not pronounced. From fitting the experimental RBS spectrum, the thickness of PANI layer deposited on an ITO/PET substrate is found to be approximately 532×10^{15} atoms/cm^2, which is about 52 nm. To convert from thickness units of atoms/cm^2 to nm, the film density of the PANI layer is assumed to be the bulk density of

0.85 g/cm^3, with the following atomic concentrations H (34%), C (56%) and N (10%). The thickness value obtained through RBS analysis is at variance with the nanoparticle size distribution measured via SEM (Fig. 5.1). The film is, on the nanometer scale, fairly inhomogeneous, and so this could be a consequence of the small spot size (< 4µm) of the He^{2+} beam used for RBS measurements, compared to the much larger SEM scan size used.

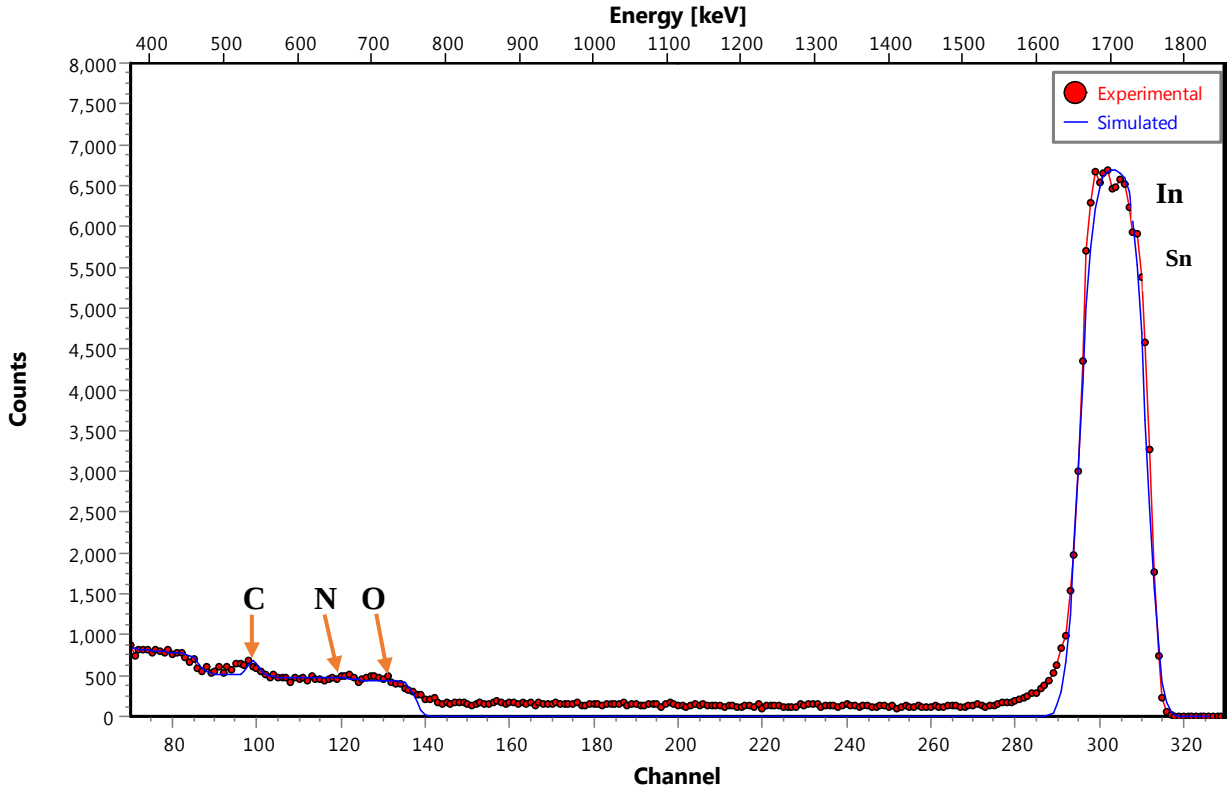

Figure 5.5: RBS spectra of unimplanted PANI for thickness measurement.

Rutherford Backscattering Spectroscopy has also been used for depth profiling of copper ions and the data is presented in Fig. 5.6. The figure shows experimental RBS spectra for implanted polyaniline samples, with an inset of simulated RBS spectrum of Cu implanted samples to the highest fluence of 5.0x10^{16} ions/cm^2. From the figure, it is expected that copper peak should appear between the channel number 260 – 285 for all implanted samples and that did not happen. This

could mean that the counts for copper ions were too low. Low counts may be attributed to the implanted ions being buried deep into the sample, the minimum detection limit and/or implantation current used [9, 10]. When the implanted ions penetrate deep into the sample, backscattering from these buried ions will be drastically reduced since these ions are shielded from the He^{2+} beam by the elements on the surface [8, 9]. The elements on the surface (In, Sn and O in our case) masked the copper ions from the beam, thus resulting in fewer backscattering events and low counts.

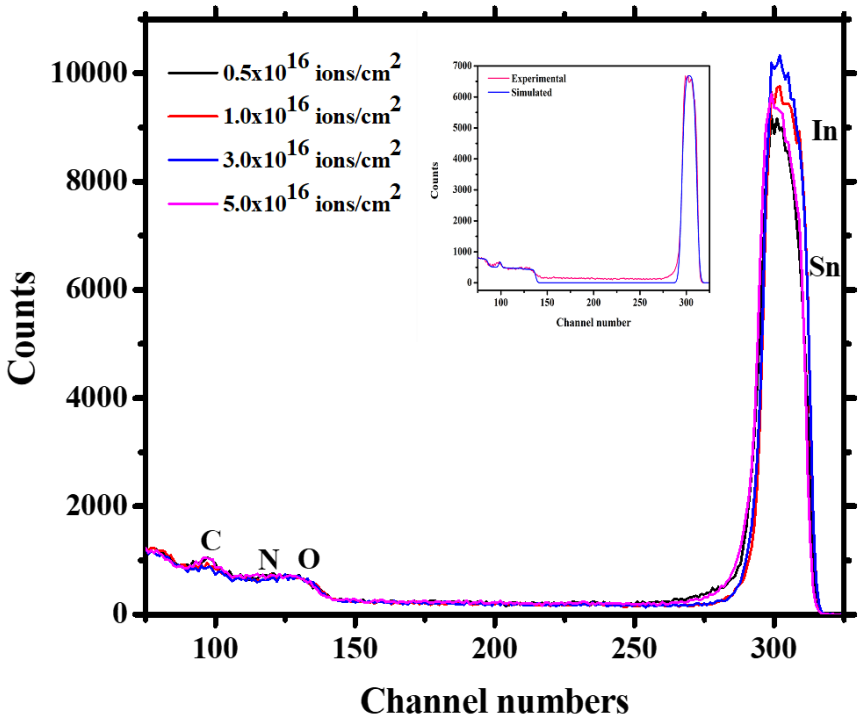

Figure 5.6: RBS spectra of implanted polyaniline on ITO/PET substrate by 50 keV Cu^{+} ions.

SRIM-2008 [11] code was used to approximate the depth of copper ions into the prepared samples. It was found that copper ions penetrated 69.2 nm into the prepared samples. This means that some of the ions were embedded below the surface of layer 1 (PANI), some on the surface of layer 2 (ITO) and the rest into layer 2, as shown in Fig. 5.7. At that depth (69.2 nm), it is still possible for scattering from copper ions to occur and for the detector to detect the energy of the backscattered ions, where the resultant copper peak is not visible on the RBS spectra.

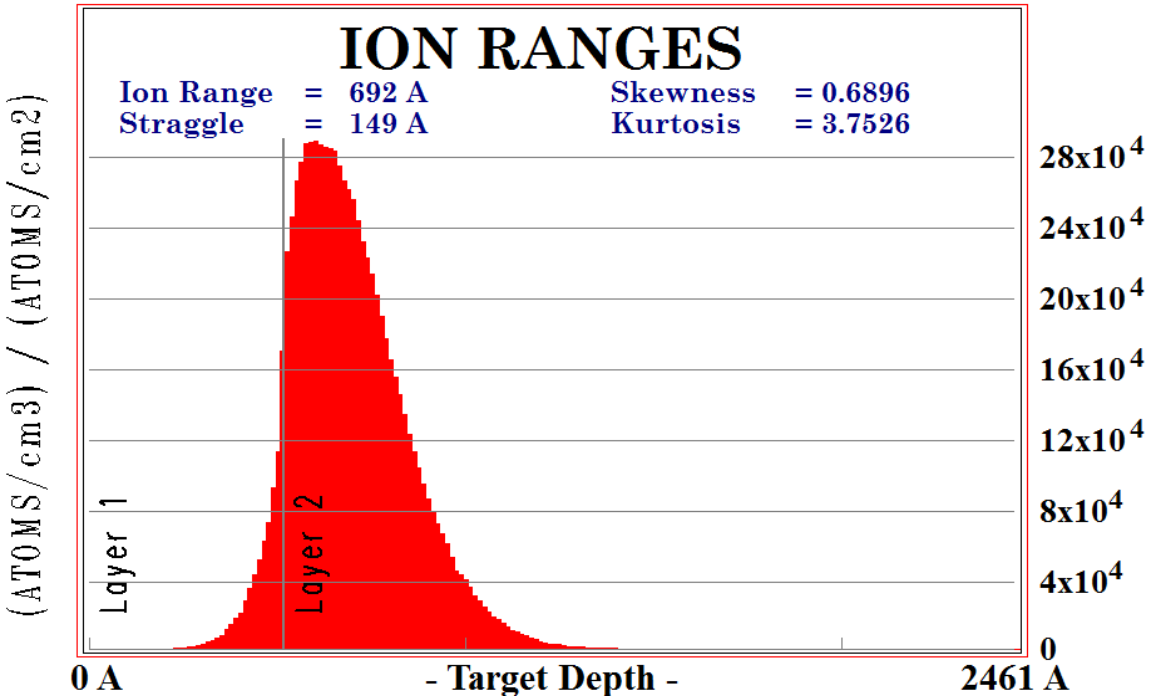

Figure 5.7: SRIM simulation results for 50-keV Cu^{+} beam on polyaniline deposited on an ITO/PET, demonstrating the depth of copper ions.

Additionally, it is noted that some of the copper ions are imbedded between layer 1 and 2, while the rest penetrated into the layer 2, which contains heavy elements Tin and Indium. As shown in Fig. 5.7, there is less concentration of copper ions on the surfaces of both layers 1 and 2 and the rest is embedded into the layer 2. Therefore, the concentration of copper ions on the surface of layer 1 and 2 combined is so low such that it is below the minimum detection limit. Hence, the count for copper peak is so low such that it does not appear on the spectra for all implanted samples. Moreover, the reason of copper peak not showing in the spectra could be the current (2 µA) which was used to accelerate He^{2+} ions during RBS measurements. It has been shown that low current makes peaks for implanted species in the spectrum not to be visible [10]. Though the ions were different from our case, the fluence was in the same range as the one used in this work.

5.1.4. Fourier Transform Infrared Spectroscopy (FTIR)

FTIR spectra of unimplanted and Cu^{+} implanted polyaniline films were recorded in the wavenumber range 2500 - 400 cm^{-1} under absorption mode and are shown in Fig. 5.8. The measurements were carried out to study chemical structure and formation mechanism of new chemical bonding after ion implantation. The following observations are made: There are two bands positioned at around 1504 and 1408 cm^{-1}, which are characteristic bands of C=C stretching vibration of quinoid and benzenoid ring, respectively [12]. The two absorption peaks indicate that the prepared polyaniline films consist of amine and amine nitrogen units in its polymer chains [13]. Bands at 1338 and 1238 cm^{-1} may be assigned to C-N stretching modes of benzenoid rings [14, 15]. A shoulder positioned at 1117 cm^{-1} is assigned to N=Q=N stretching and is a measure of the degree of electron delocalization and is a characteristic peak of PANI conductivity [6, 16]. The peak at 1095 cm^{-1} is assigned to C-N stretching of secondary aromatic amine due to charge delocalization over the polymer backbone [17, 18]. Peaks at around 845 and 501 cm^{-1} bands are related to C-H out-of-plane bending vibration in the 1, 4 disubstituted benzene ring [19] and C-H out-of-plane bending vibration [20], respectively. The main peaks conform to the PANI structure as shown in the previous works [21-24].

Upon ion implantation, an overall minor decrease in the FTIR peak intensities associated to the functional groups present in polyaniline is observed. This minor decrease in the peak intensities could be due to implantation temperature. The ions were introduced into the polyaniline matrix at cryogenic temperature, and this temperature might have been so low such that the formation of free radicals, cross-linking, carbonization and degradation of the polymeric chains due to implantation was highly suppressed and it was our intensions to do so in order to protect the films

from radiation damage. As mentioned in section 4.2, cryogenic implantation minimizes radiation damage to the polymeric films more especially when the films are implanted to higher fluence (such as in our case).

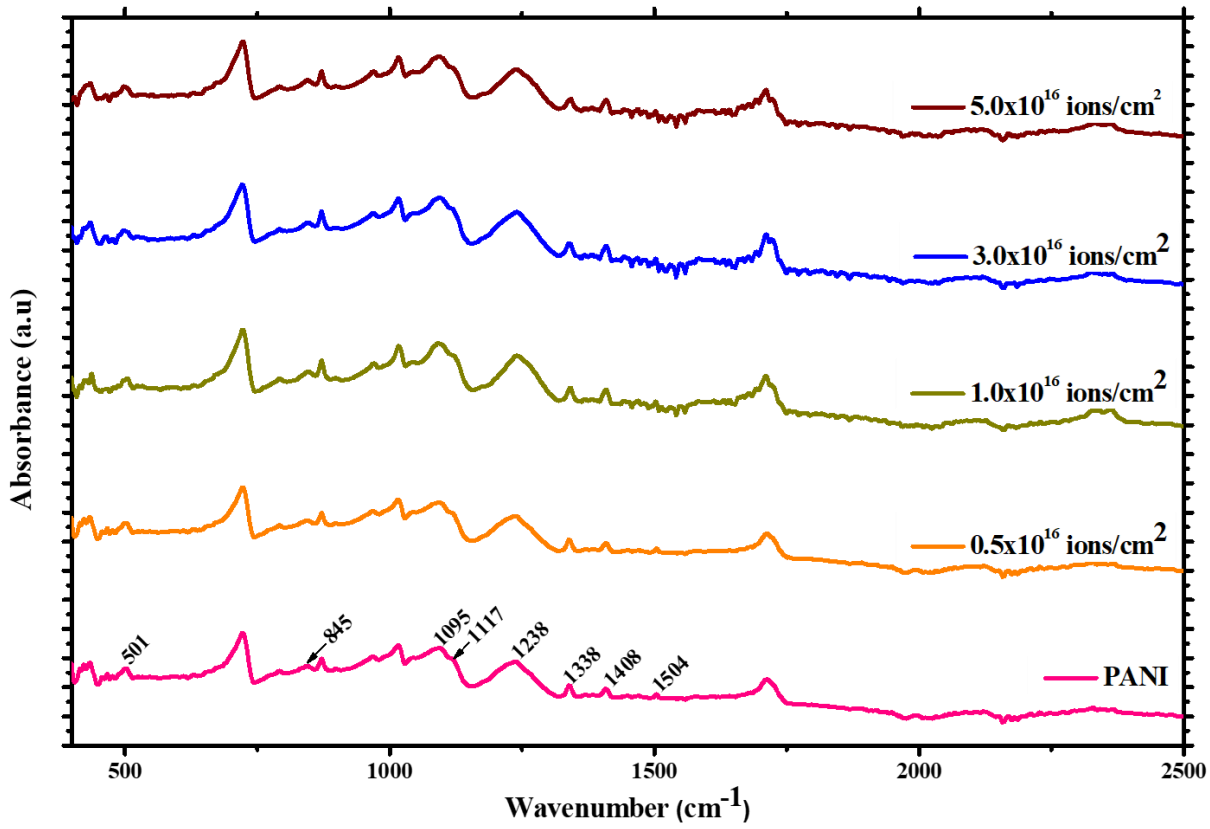

Figure 5.8: FTIR spectra of unimplanted and Cu^+ implanted PANI films.

5.1.5. Raman Spectroscopy

The RAMAN spectra of unimplanted and Cu^+ implanted PANI films were recorded using 532 nm exciting wavelength and the results are presented in Fig. 5.9. For unimplanted PANI, a number of bands have been observed and the bands appearing in the wavenumber range of 1100–1600 cm^{-1} correspond to the stretching modes of different bonds. The intense Raman band observed at 1614 cm^{-1} is assigned to the C-C stretching vibration of benzene ring [25]. The band appearing at 1285 cm^{-1} is assigned to the stretching mode of C-N*$^+$ delocalised polaronic structure, which is

characteristic of the protonated imine form of polyaniline [25]. The bands at 1184 and 1093 cm^{-1} may be attributed to C-H bending vibrations in benzenoid rings and C-N stretching mode of polaronic unit [26, 27], respectively.

The band observed in the wavenumber range of 1000 - 400 cm^{-1} gives the information about the deformation vibrations of the benzene rings. The band at 859 cm^{-1} is out of plane vibrations of protonated emeraldine form of PANI, while the band observed at 630 cm^{-1} is related to the deformation of the benzene ring in the PANI backbone [28, 29]. Most of the observed bands are in good agreement with the known chemical structure of EB form of PANI. However, for ion implanted films, RAMAN spectrum is different from that of unimplanted PANI films in that most of the bands are not observed and there is only one weak peak located at around 1614 cm^{-1}. This peak was observed in the spectrum for unimplanted PANI at that position and it was quite intense [29].

The observed differences between unimplanted and implanted PANI films may be attributed to several factors such as formation of free radicals, cross-linking, and cleavage of chemical bonds such as C-H and formation of more compact carbonaceous structure in the implanted PANI films. The observed structural changes in FTIR spectroscopy were relatively small, while in RAMAN spectroscopy were appreciably visible. As mentioned in section 3.4.4, this is because the RAMAN spectroscopy technique is more sensitive to the lengths, strengths, and arrangement of bonds in a material than FTIR technique [30]. The structural and chemical modifications after ion implantation are most probably responsible for the observed changes in optical and electrical properties of Cu^{+} implanted PANI, which are described next.

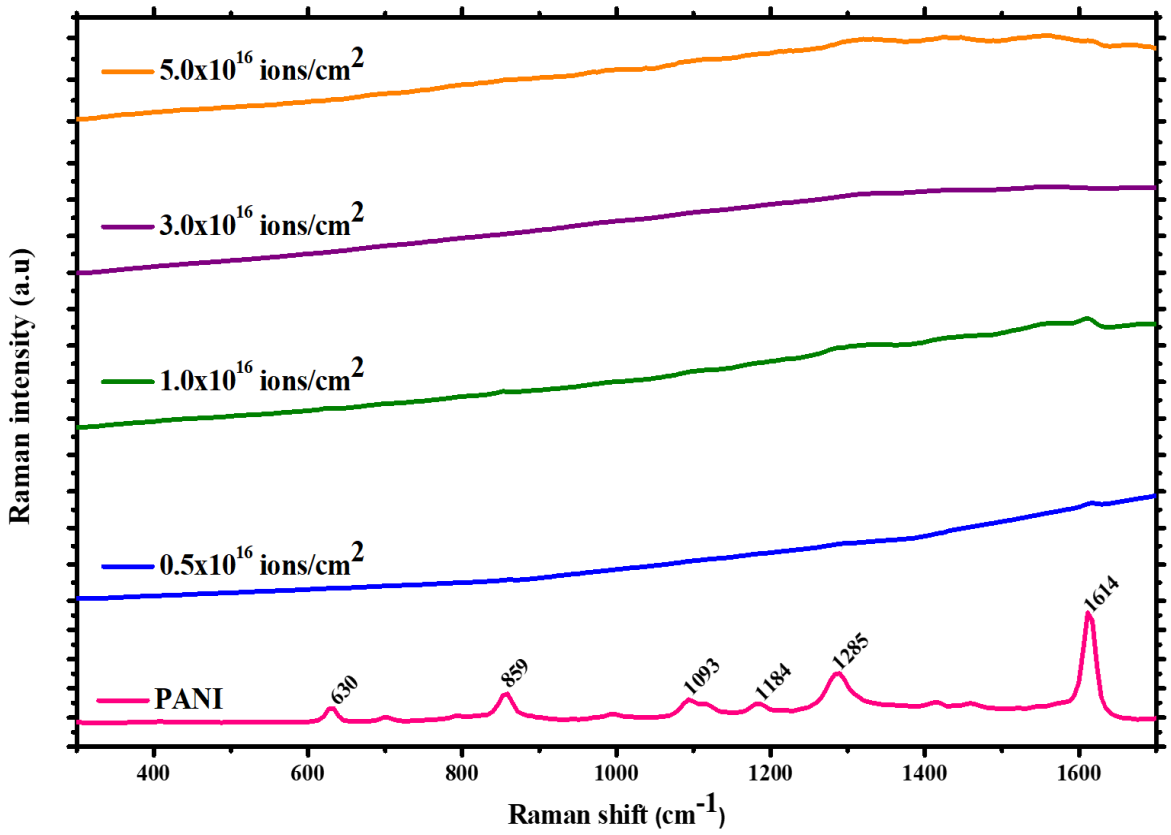

Figure 5.9: RAMAN spectra of unimplanted and 50-keV Cu^{+} implanted PANI films.

5.1.6. UV-Visible spectroscopy

UV-Vis absorption spectra of unimplanted and implanted PANI films are reported in Fig. 5.10. The wavelength ranged from 320 to 700 nm under absorption mode. In case of unimplanted PANI, two distinctive absorption peaks at 340 and 565 nm were observed (Fig. 5.10-a). The observed peaks coincide with the EB form of PANI reported in the literature [31]. The presence of these peaks is another confirmation of the formation of PANI on the ITO/PET substrate. The lowest wavelength absorption peak (340 nm) is attributed to π-π* electron transition of benzenoid rings [32]. The broad peak around 565 nm is assigned to exciton transition of the quinoid rings [33].

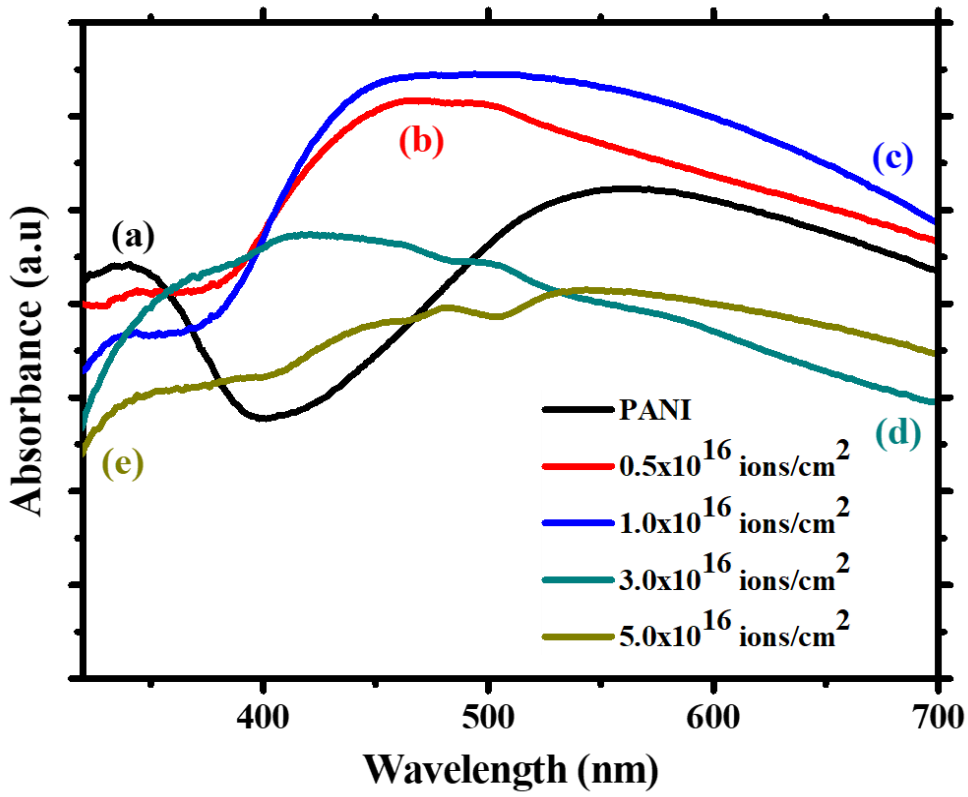

Figure 5.10: UV-Vis Spectra of unimplanted and Cu^{+} implanted PANI films.

Upon implantation to fluences of $0.5x10^{16}$ and $1.0x10^{16}$ ions/cm^2, a prominent increase of the absorbance as a function of fluence is observed (Fig. 5. 10-b and c). In addition, a shift in the absorption peaks to lower wavelength is observed. For higher fluences of $3.0x10^{16}$ and $5.0x10^{16}$ ions/cm^2, two absorption peaks in the unimplanted PANI almost coalesced to form one broad peak with a continuous decrease in its absorption intensity with increasing fluence is observed, as shown in Fig. 5.10-d and e.

Additionally, there is detection of new peaks positioned at around 490 and 480 nm (Fig. 5.11), respectively. The detected peaks may be attributed to SPR characteristic peaks for copper NPs [31]. The presence of these peaks is a good indicator of the formation of copper nanoparticles

inside the polyaniline matrix. All the observed changes may be attributed to carbonization of the polymer subsurface layer and/or may be explained considering the Surface Plasmon Resonance (SPR), which is related to the collective oscillation of conduction electrons in metal NPs in response to optical excitation [34-37]. As explained elsewhere, the fraction of the implanted Cu^+ ions are still in atomic state and they do not participate in the formation of metal and/or metal-oxide aggregates, as it is indirectly confirmed by the background signal intensity in the extinction spectra [38. 39].

The position of the SPR peak of copper NPs observed in this study at fluences of $3.0x10^{16}$ and $5.0x10^{16}$ ions/cm^2 have not been reported before. However, Niranja *et al.* [40] reported that SPR peaks for copper NPs appear in wavelength ranging from 350-800 nm. Therefore, we can confidently assign the new detected peaks to SPRs for copper NPs since the peaks appear within the reported range. It can be noted from Fig. 5.11 that the SPR peaks shift to higher wavelength with increasing fluence. The wavelength of SPR peak depends on the size, shape of metal NPs and dielectric properties of metal NPs together with surrounding medium leading to either red or blue shift [41, 42].

When fluence is increased beyond the surface threshold (i.e. fluence at which the surface of the film is completely filled with ion tracks [43]) two or more NPs could aggregate leading to the formation of NPs having relatively larger sizes and different shapes. Therefore, the observed shifting in SPR peak to higher wavelength in this study can be attributed to an increase in average size, presence of different shapes of Cu^+ NPs. Similar shift in SPR peak for copper NPs has been reported before [44, 45].

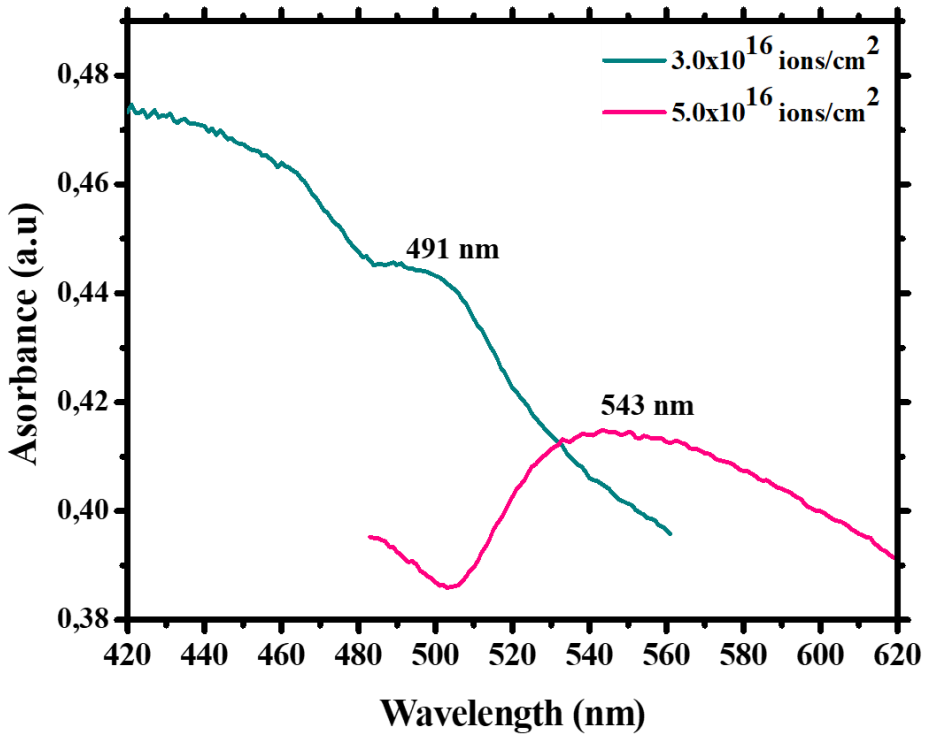

Figure 5.11: Comparison of SPR characteristic bands for copper NPs at ion fluence of $3.0x10^{16}$ and $5.0x10^{16}$ ions/cm^2.

Fig. 5.12 shows the relation of $(\alpha h\nu)^2$ versus photon energy ($h\nu$) for unimplanted PANI film. It is observed from the figure that the direct optical band gap is 3.12 eV. This value is slightly lower than 3.38 eV and 3.80 obtained by Yadov et al [46] and Bhattacharya et al [47], respectively, but higher than 3.04 eV obtained by Mathai et al [48]. All these values were determined on the data acquired from relatively "defect free" or unimplanted polyaniline (EB). The energy gap obtained here falls within the acceptable range since it is similar to the ones reported in the literature. This indicates that the samples were successfully prepared and indeed it is polyaniline (EB) that was deposited on the ITO/PET substrate. It is expected, however, that this value will change after implantation since the defects would be induced in the material.

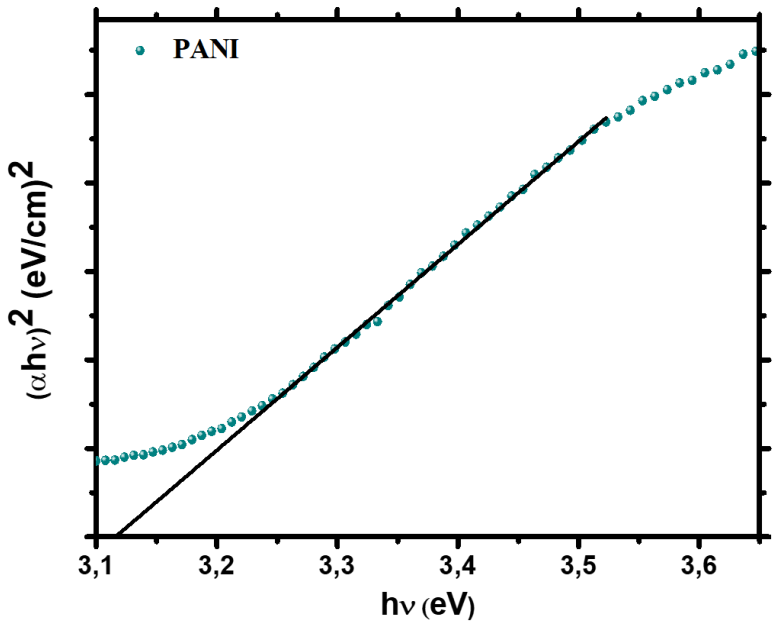

Figure 5.12: Plot of $(\alpha h\nu)^2$ against photon energy ($h\nu$) of pure PANI film.

Fig. 5.13 shows plots of $(\alpha h\nu)^2$ versus photon energy ($h\nu$) for Cu^+ implanted PANI films. From the figure, it is observed that the direct optical band gap blue shifts as a function of the ion fluence from 3.12 eV value of the unimplanted PANI to 1.84, 1.52, 1.50 and 1.41 eV, respectively. The observed decrease in optical band gap with increasing ion fluence has also been reported by [39] for copper, gold and silver into a polycarbonate (PC) matrix. The reduction in the bandgap may be correlated with the generation of defect levels within the band gap [49], carbonization of the polymer subsurface layer and the formation of carbon clusters [38, 39]. The generation of defects is probable since ion implantation imparts energy and momentum on the host atoms. As the implanted Cu^+ ions impart energy and momentum, they displace the host atoms from its lattice site, hence generating vacancies and interstitials. Depending on the energy of the incident copper ions, the imparted atom may interact with other host atoms, thereby further generating vacancies and interstitials as it comes to rest. These defects, vacancies and interstitials, result into different energy levels with different properties in the band gap of polyaniline, depending on the density of

the dopants. These defect levels are responsible for a change in optical and electrical properties of the material. A change in electrical properties due to ion implantation is presented in the next chapter.

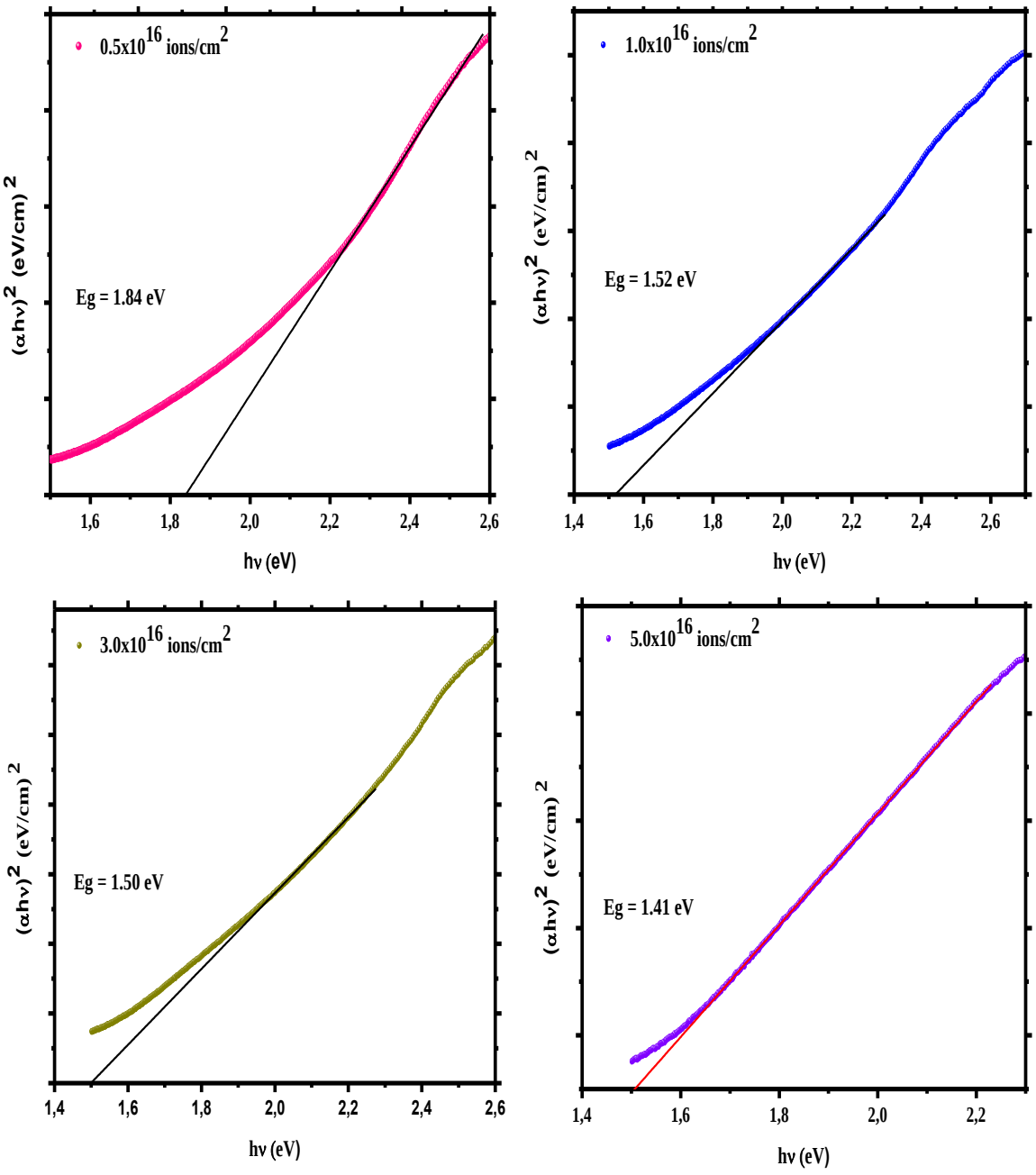

Figure 5.13: Plots of $(\alpha h\nu)^2$ against photon energy ($h\nu$) of Cu^+ implanted PANI films.

Fig. 5.14 shows the graph of optical band gaps of polyaniline films as a function of ion fluence. It is observed from the figure that the value of the band gap decreases drastically at the initial stage of ion implantation. This sudden decrease indicates that the effect of Cu^+ implantation on the optical properties of the material is high at this low fluence. As the fluence increases, the effects of Cu^+ on the optical properties become reduced hence the trend becomes horizontal, indicating that the band gap is now independent of ion fluence after the fluence of $0.5x10^{16}$ ions/cm^2. The reason for this trend can be explained either in terms of the defects induced by copper or in terms of surface threshold fluence. In any case, the results are such that the material become stable and resistant to change. This resistance starts at the fluence of about $1.0x10^{16}$ ions/cm^2, the fluence that is believed to be important for studies on modification of polyaniline for radiation sensing applications.

The results presented in Fig. 5.14 could be indicating that in PANI, copper generates defects with different properties, perhaps, at different levels within the band gap. Of all generated defects, there are two types showing their activities at different fluences. The first is active at low fluences, at the region where the energy gap decreases drastically. The decrease in energy gap as a function of fluence is an indication that the number of charge carriers generated increases with fluences. The generated carriers are increased because the induced defects are responsible for generation of charge carriers.

At the fluence higher than $0.5x10^{16}$ ions/cm^2, the trend becomes horizontal since another type of defect becomes active. This type of defect recombines charge carriers in the same rate as it generates them. As a result, it makes properties of the material independent of the ion fluence. Similar explanation was given based on the semiconductor that was irradiated by 1 MeV neutrons

to the highest fluence of $1.0x10^{17}$ neutrons/cm^2 [50]. The results in that case were explained in terms of "midgap defect", which is the defect level situated at the center of the energy gap of the material and is responsible for radiation-hardness of the material [51].

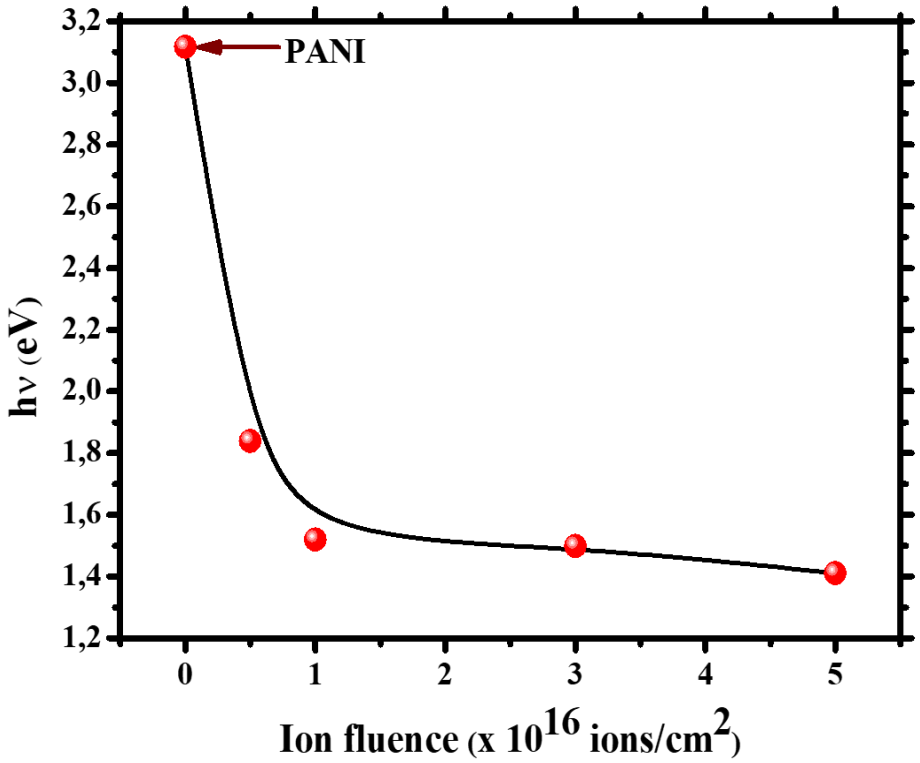

Figure 5.14: Variation of the optical band gap as a function of the ion fluence.

It can, therefore, be postulated that in PANI, copper also generates defect levels that are responsible for radiation hardness of the material. This postulation is reached because irradiation is similar to ion implantation (doping), both generate defect levels in the energy gap of the material [52]. This data generally indicates that Cu^+ implantation has altered the material such that optical properties become altered. The results also show that implantation to higher fluence would result in negligible changes. Thus, the material would be resistant to change and this makes them very ideal for detector applications.

According to the relation [53] $N = \frac{34.3}{Eg}$, the energy gap value decreases linearly with the number of Carbon atoms (N) in the cluster. Since N increases with fluence, it was expected to observe E_g decreases with N. This conjecture has been presented and is in good agreement with the data acquired to fluence lower than $1x10^{16}$ ions/cm^2 [54]. The results obtained in this work indicate that the above linear relation holds only for the fluence equals to and/or lower than $0.5x10^{16}$ ions/cm^2. The results clearly explain the link of the crystal structure and defect level properties in the energy gap of the material.

The trend can also be explained in terms of surface threshold fluence, which indicate that any increase in fluence results in lower rate of decrease. For this study, the surface threshold fluence was found to be $0.5x10^{16}$ ions/cm^2. Different surface threshold fluences for different implanting species and polymers were reported before [39, 43, 55]. The stability of the band gap values indicates an intermediate saturation process of the carbon-cluster agglomeration and cross-linking since the clusters are the main absorption centers in the implanted polyaniline. This change in optical band gaps of the films is in good correlation with the decrease in conductivity (reported later in section 5.2) of the films since optical band gap and electrical conductivity are strongly connected to the chemical and structural alteration of the polymer under implantation.

The concept of surface threshold fluence explains the generated crystal defects in terms of structural properties while that of defect levels explains the defects in terms of electrical properties (charge carriers) of the material. A thorough explanation of change in electrical properties of the material due to implantation is explained later in the section.

5.1.7. Photoluminescence spectroscopy (PL)

The room temperature photoluminescence spectra of unimplanted and Cu^+ implanted polyaniline thin films in the range of 320 – 900 nm are presented in Fig. 5.15. In this study, the wavelength of excitation chosen for all the samples is 315 nm. This is because of π-π* transition of benzenoid units is responsible for PL in polyaniline [56]. The PL spectra for unimplanted and Cu^+ implanted PANI films all show one high intense and one broad, fairly weak emission peaks centered at around 374 – 398 and 756 – 760 nm (shown in the inset), respectively. The band at 374 – 398 nm may be attributed to polaron band transition of PANI and the band at 756 – 760 nm may be attributed to transition of electrons from conduction band to valence band [56].

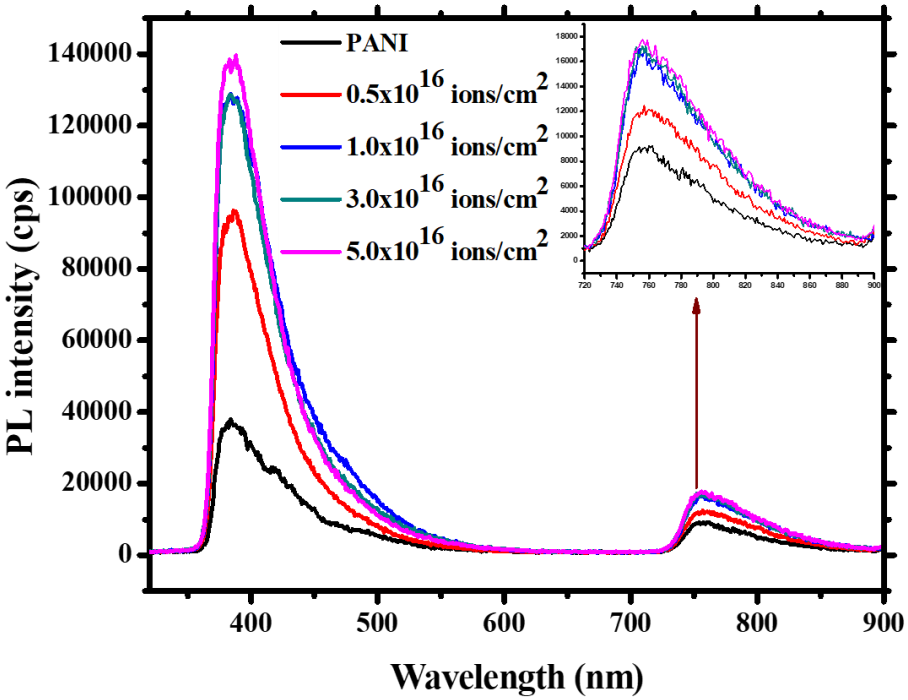

Figure 5.15: Photoluminescence spectra of unimplanted and Cu^+ implanted PANI films.

From the Fig. 5.15, it is observed that the PL spectra for unimplanted PANI film has less intensity when compared to that of Cu^+ implanted films. In Fig 5.16, it is observed that the emission peak intensities for Cu^+ implanted films, increasing gradually with increasing ion fluence. This is

attributed to an incorporation of Cu^{+} ions into polyaniline. The ions change the structure of polyaniline by making the benzenoid and quinoid units (which are responsible for PL) to be more orderly arranged. This rearrangement of benzenoid and quinoid units favors the formation of singlet excitons. When these singlet excitons decay to ground state, light is emitted. It is noted that the formation of singlet excitons increases with an increase in the conjugation length of the polymer chain [57].

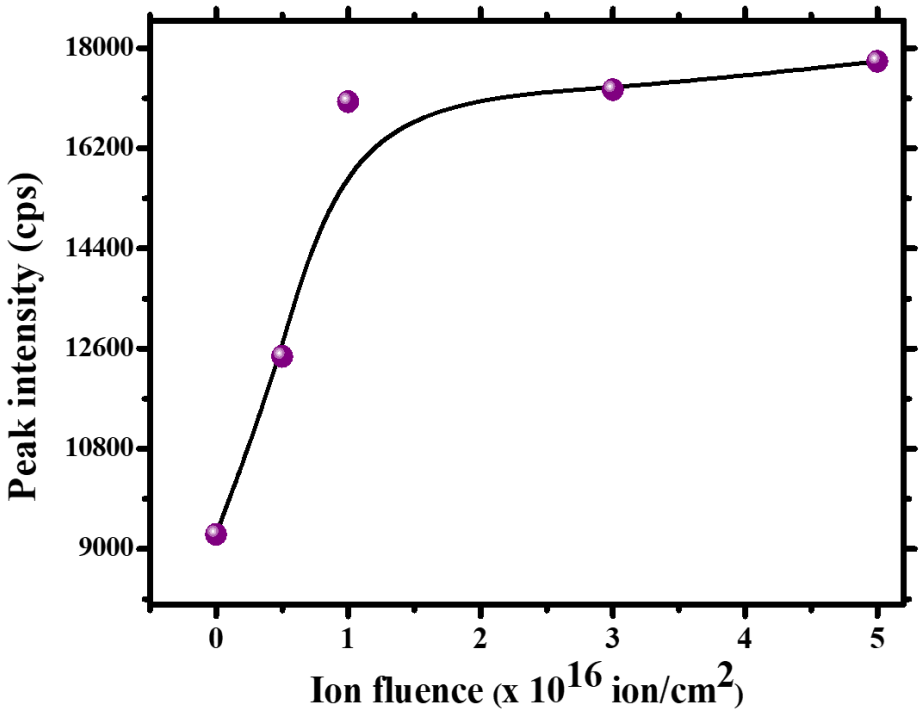

Figure 5.16: Variation of the PL peak intensities as a function of the ion fluence.

This may be attributed to the fact that the delocalization length of singlet exciton in conjugated polymers is comparable to its conjugation length [5, 57]. The triplet exciton of the conjugated polymer is confined [57]. In conjugated polymers, singlet excitons are mostly responsible for PL emission because conjugated polymers cannot produce the spin flip which is necessary for an optical transition [5, 58]. Hence, one should expect higher emission PL from Cu^{+} implanted PANI films, which has a higher extent of π-conjugation than unimplanted PANI.

A trend in Fig 5.16 is similar to that of Fig 5.14 and Fig. 5.18 in opposite direction, showing that the techniques, UV-Vis, PL and I-V, complement each other. Based on the results from these techniques, a decrease in the energy gap due to implantation results in an increase in the number of charge carriers which are responsible for the decrease in resistance of the films. This corresponding decrease in resistance is shown later in the chapter, in Fig. 5.18.

5.2. Device characterization

This section presents and discusses the results obtained from current-voltage (I-V) measurements carried out on unimplanted and Cu^{+} implanted PANI. The measurements were carried out at room temperature to investigate a change in electrical properties of the material due to ion implantation.

5.2.1. Current-Voltage measurements

Fig. 5.17 shows I-V characteristics of the device fabricated with unimplanted and Cu^{+} implanted PANI films. It can be seen from the figure that the current varies fairly linearly with voltage for all the films. Linear behavior of implanted polymer as a function of applied voltage was also reported by [39, 59, 60]. It can, however, be observed from Fig. 5.17 that the magnitude of current increases fairly with ion fluence for the same voltage, indicating that the resistance of the films has decreased. The observed decrease in resistance may be attributed to carbonization of the polymer subsurface layer and the formation of carbon clusters which, which in turn form conducting networks or metal "islands" [61, 62, 63]. Carbonization process makes the polymer rich in carbon atoms and it is known that carbon atoms are clustered with Sp^2 hybridization and this type of chemical bonding possess more unpaired π-electrons, which become charge carriers in the implanted polymer, thus reducing resistance of the polymer. Carbon clusters are conducting

islands which are also rich in charge carriers, provide path for the charge transfer within the polymer chain, and thus influence the hopping or tunneling mechanism between the islands. The formation of these clusters in the films may have resulted in the reduction of their resistance [64, 65]. Another reason for this decrease in resistance could be the introduction of defect levels within the forbidden band, which are responsible for the generation of charge carriers [66-68].

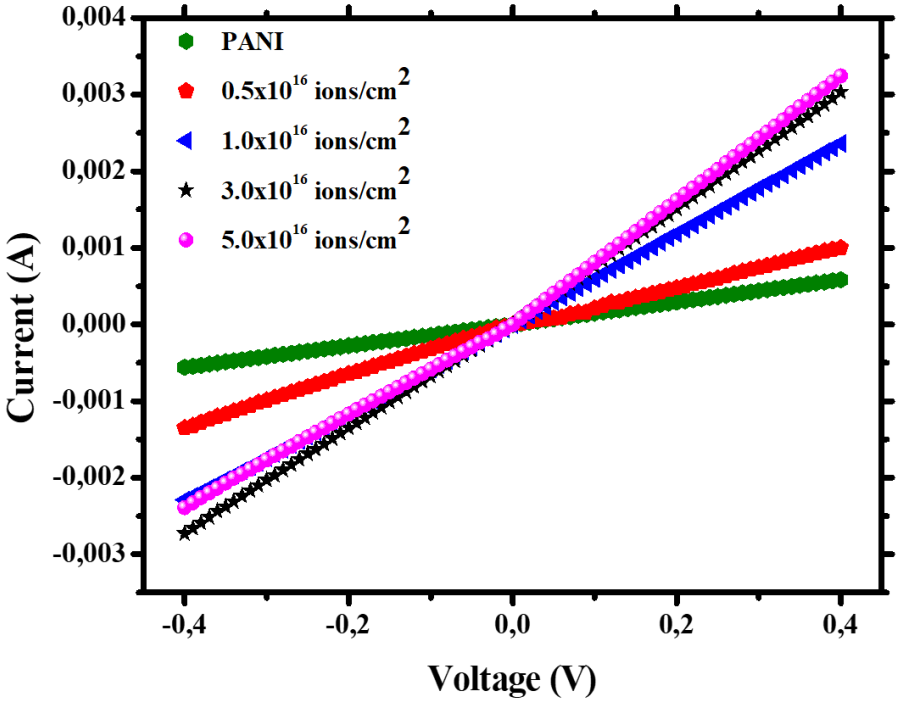

Figure 5.17: The I-V characteristics of unimplanted and Cu^{+} implanted PANI films.

To investigate the variation of the material resistance with fluence, the evaluated resistance was plotted as a function of ion fluence, as shown in Fig. 5.18. It can be seen from the figure that the resistance of the material decreases with ion fluence. As mentioned above, this decrease in electrical resistance may be correlated with the carbonization of the polymer and possible introduction of defect levels within the forbidden gap. I-V data complements that of UV-Vis, both indicating that the energy required to generate considerable number of charge carriers to contribute to the measured current has decreased. The trend similar to that in Fig. 5.18 was reported before

[68] for Cu, Au and Ag implanted into polycarbonate (PC) and was explained in terms of surface threshold fluence.

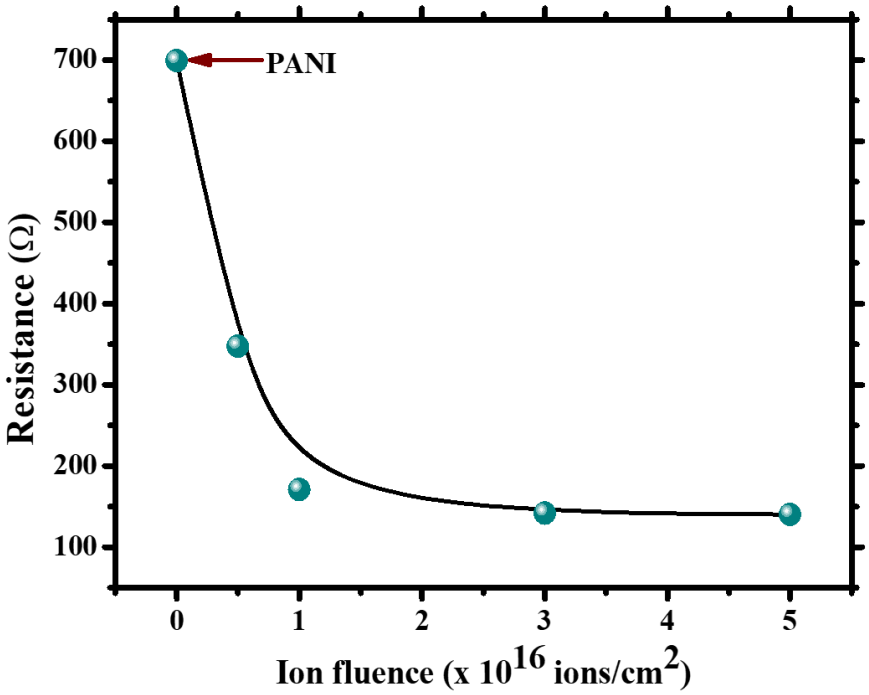

Figure 5.18: Plot of resistance against ion fluence for unimplanted and Cu^+ implanted PANI films.

5.3. Overview

It is observed from the acquired data that ion implantation led to a change in structural, optical and electrical properties of polyaniline. The changes are due to crystal defects that are induced by ion implantation in polyaniline matrix [39, 40]. These structural changes, though not so evident from FTIR, are confirmed through RAMAN spectroscopy. A change in optical properties of the material was confirmed by a decrease in optical band gaps as a function of ion fluence. The band gap has been found to decrease drastically at the initial stage (low fluence) of ion implantation. This drastical change indicates that the effect of Cu^+ implantation on the optical properties of the material is high at low fluence. As the fluence increases, the effects of Cu^+ on the properties

become reduced hence the trend becomes horizontal, indicating that the energy gap is now independent of the ion fluence.

This is an indication that the films are getting damaged at the initial stage (low fluence) and become resistant to damage as the fluence increases. In general, this is an indication that implantation by copper ions to high fluences can be used as an effective tool to tailor properties of the material so that it becomes resistive to change. Thus, the material is stable, and this stability is suitable for the material to be used for fabrication of radiation sensors. Sensors fabricated on this modified polymer would operate under high radiation environment without losing its functionality.

Moreover, the observed trends may be attributed to the incorporation of structural changes as an effect of ion implantation. For example, as the ion fluence increases, more ions are introduced into the polymer matrix, and as a result, the surface of the implanted films become richer in carbon through carbonization process. As mentioned in section 2.6, carbon atoms are clustered with Sp^2 hybridization and this type of chemical bonding possess more of unpaired π-electrons, which become charge carriers in the implanted polymer [6]. When more ions are introduced into the polyaniline matrix, ions tend to form more carbon clusters. These carbon clusters are conducting islands, which are also rich in charge carriers, provide path for the charge transfer within the polymer chain, and thus influence the hopping or tunneling mechanism between the islands [68, 69]. As a result, a drastical decrease in electric resistance becomes gentle as fluence increases, resulting in reduced opposition to current flow on the surfaces of Cu^+ implanted films. Thus, at high radiation fluence, the structure somewhat becomes stable indicating that the material is resistant to further damage.

5.3. References

[1] Etorki A. M. *et al.* 2017 *J. Environ. Toxicol*. **7** 471.

[2] Amaechi I. C. *et al.* 2015 *Eur. Phys. J. Appl. Phys.* **69** 30901.

[3] Tesmer J. R. and Nastasi M. 1995 *Handbook of Modern Ion Beam Analysis*. (Material Research Society.: Pittsburgh).

[4] Verma H. R. 2007 *Atomic and Nuclear Analytical Methods*. (Springer-Verlag Berlin.: Heidelberg).

[5] Rania E. *et al*. 2015 *American J. Polym. Sci*. **5** 10.

[6] Gupta K. *et al*. 2010 *Synth. Met*. **160** 1566.

[7] Mayer M. 1997 *SIMNRA User's Guide, Technical Report IPP9/113*. (Max – Planck Institute für Plasmaphysik.: Garching).

[8] Bird J. R. and Williams J. S. 1989 *Ion Beams for Materials Analysis.* (Academic Press.: Samford Valley).

[9] Feldman L. C. and Mayer J. W. 1986 *Fundamentals of Surface and Thin Film Analysis.* (Elsevier Science Publishing Co.: Amsterdam).

[10] Marin N and Serruys Y 1997 *Nucl. Instrum. Meth. B* **131** 3109.

[11] Ziegler J. F. 2008 *SRIM-2008 Computer code*: http://www.srim.org [Accessed: March 2019].

[12] Beckerle P. *et al*. 2000 *Nucl. Instrum. Meth A.* **449** 302.

[13] Zhang J. 2007 *Appl. Surf. Sci.* **253** 5436.

[14] Ratier B. *et al*. 2000 *Synth. Met.* **115** 103.

[15] Trchova M. *et al.* 2004 *Polym. Degradation and Stability* **86** 179.

[16] Vladu M. I. *et al.* 2006 *Synth. Met*. **156** 1401.

[17] Khalid M. *et al.* 2009 *Synth. Met.* **159** 119.

[18] Prabhakaran T. *et al.* 2008 *J. Polym. Sci.* **46** 2418.

[19] Xu G. H. *et al.* 2013 *J. Colloid Interface Sci*. **411** 204.

[20] Sharma I. D. *et al*. 2013 *Indian J. Eng. Mater. Sci*. **20** 145.

[21] Zhang L. J. *et al*. 2003 *Adv. Funct. Mater*. **13** 815.

[22] Lei X. P. *et al*. 2007 *Polym. Adv. Technol.* **18** 472.

[23] Karim, M. R. *et al.* 2008 *Reactive & Functional Polymers* **68** 1371.

[24] Jacek N. *et al*. 2011 *Polymer Bulletin* **66** 761.

[25] Ashwini B. *et al.* 2014 *High Performance Polymers* **26** 641.

[26] Mazzeu M. A. C. *et al*. 2017 *J. Aerosp. Technol. Manag*. **9** 39.

[27] Moravková Z. *et al.* 2012 *Thin Solid Films* **520** 6088.

[28] Nascimento G. M. *et al*. 2008 *J. Raman spectroscopy* **39** 772.

[29] Ward Y *et al*. 1999 *Polymer* **40** 2465.

[30] Brundle C. R. *et al.* 1992 *Encyclopedia of Materials Characterization*, 1st edition. (Butterworth-Heinemann.: Oxford).

[31] Du X. *et al.* 2012 *Nanoscale Research Letters* **7** 111.

[32] Dong Y. *et al*. 2007 *Nanotechnology* **18** 455603.

[33] Abdulla H. S. *et al.* 2012 *In. J. Electrochem. Sci.* **7** 10666.

[34] Sharma T. *et al.* 2007 *J. Appl. Phys*. **102** 63527.

[35] Shekhawat N. *et al.* 2011 *J. Appl. Phys.* **109** 083513.

[36] Jana J. *et al.* 2016 *RSC Adv*. **6** 86174.

[37] Liang A. *et al.* 2012 *Trends in Analytical Chemistry* **37** 32.

[38] Popok V. N. *et al.* 2012 *Rev. Adv. Mater. Sci.* **30** 1.

[39] Resta V. *et al*. 2013 *Nucl. Instrum. Meth. B* **312** 42.

[40] Niranjan M. K. *et al*. 2012 *Physicochem. Eng. Aspects* **407** 58.

[41] Yeshchenko O. A. *et al*. 2007 *Materials Science and Engineering* **137** 247.

[42] Yeshchenko O. A. *et al.* 2009 *Physical Rev*.**79** 235438.

[43] Popok V. N. *et al*. 2004 *Appl. Phys.* **78** 1067.

[44] Doremus R. *et al.* 1992 *Appl. Opt*. **31** 5773.

[45] Yoon K. Y. *et al.* 2007 *Science of the Total Environment* **373** 572.

[46] Bhattacharya P. *et al.* 2014 *RSC Adv*. **4** 17039.

[47] Yadov J. B. *et al*. 2007 *J. Non-Cryst. Sol.* **353** 4691.

[48] Mathai C. J. *et al.* 2002 *J. Phys.* **35** 2206.

[49] Mallick K. *et al.* 2007 *J. Phys. Condens. Matter*. **19** 196225.

[50] Moloi M and McPherson M 2009 *Physics B* **404** 3922.

[51] Litovchenko P. G et al. 2006 *Nucl. Instr. Meth. A* **568** 78.

[52] Moloi S. J and McPherson M. 2014 *Vacuum* **104** 51.

[53] Atta A. *et al*. 2013 *Nucl. Instrum. Meth. B* **300** 46.

[54] Drozdziel A et al. 2017 *Acta Physica Polonica A* **132** 264.

[55] Popok V. N. 1999 *Surf. Invest*. **14** 843.

[56] Shimano J. Y. *et al.* 2001 *Synthetic Metals* **123** 251.

[57] Wohlgenannt M. *et al.* 2003 *J. Phys. Condens. Matter*. **15** 83.

[58] Kohler A. *et al*. 2002 *Adv. Mater.* **14** 701.

[59] Popok V. N. *et al.* 1999 *Nucl. Instrum. Meth. B* **148** 1106.

[60] Wang W. M. *et al.* 1991 *Nucl. Instrum. Meth. B* **61** 466.

[61] Fink D. 2004 *Fundamentals of Ion-Irradiated Polymers*. (Springler Verlag Berlin.: New York).

[62] Tóth A. *et al.* 2011 *Appl. Surf. Sci.* **257** 10815.

[63] Wu Y. *et al.* 2001 *Sci. China E* **44** 493.

[64] Döbeli M. *et al.* 1991 *Radiat. Eff. Defects Solids* **118** 325.

[65] Wang Y. *et al.* 1993 *J. Mater. Res.* **8** 388.

[66] Radwan R. M. *et al*. 2008 *Nucl. Instrum. Meth. B* **266** 3588.

[67] Rao G.R. *et al.* 1994 *Surf. Coat. Technol.* **64** 69.

[68] Resta V. *et al.* 2014 *Nucl. Instr. Meth. B* **331** 187.

[69] Kumar V. *et al.* 2012 *Radiat. Phys. Chem.* **81** 652.

CHAPTER 6: CONCLUSION

6.1. Material characterization

Polyaniline films were successfully prepared on ITO/PET substrate using a spin coater. The structure of polyaniline formed on the ITO/PET substrate was investigated and found to be in good agreement with the PANI structure reported in the literature. Thereafter, the prepared polyaniline films were implanted with copper ions to different fluences. A change in structural, optical and electrical properties with fluence was also studied. The results were explained in terms of the crystal defects induced by implantation in polyaniline matrix.

The prepared films were amorphous in nature, with nanoparticles that were spherical in shape. The size of the nanoparticles varies from 7.0 to 269 nm with mean particle size of 194 nm. In addition, the thickness of PANI films on the substrate was found to be 51.8 nm.

FTIR measurements indicated that implantation at liquid nitrogen temperature caused little bonding disruption in the molecular structure of implanted polyaniline films.

The optical band gap was found to decrease with fluence from 3.12 to 1.41 eV. It was observed that ion implantation led to an enhancement in the emission peak intensities of the implanted films because of higher extent of π-conjugation coupled with the more orderly arrangement of the benzenoid and quinonoid units (responsible for PL in PANI) as a result of implantation.

6.2. Device characterization

The results reveal that ion implantation led to a decrease in resistance of the polyaniline. This decrease in resistance indicates that implantation generates defects responsible for generation of charge carriers to decrease the resistance of the polyaniline films.

In general, UV-Vis, PL and I-V techniques complement each other indicating that the material gets damaged at initial stage (low fluence) of implantation and becomes resistant to damage as the fluence increases. Thus, a heavily copper ion implanted polyaniline is a promising material for fabrication of efficient radiation sensors.

6.3. Possible future work

The work presented here serves as an initial investigation of the implanted PANI. The results that were obtained in the present study raised more interesting questions about the crystal defects in PANI matrix for radiation sensing applications. To extend the study further, topics such as effect of light and temperature on electrical properties of the sample will need to be covered to predict the behavior of the detector when operating at different conditions. Other measurements like Hall effect and capacitance-voltage (C-V) would also be performed to determine the carrier type and concentration of the material. It would also be interesting to characterize samples with deep level transient spectroscopy (DLTS) technique to catalogue defects that are induced by copper implantation in the material.

Possible future work would also involve investigation of the effect of implantation by other metal ions such as gold, iron and silver. Further to this, work would be done on other polymers to arrive at a holistic view of the stability of metal-implanted polymer for radiation sensing applications. The samples will be irradiated with neutrons and protons to establish their radiation hardness.

APPENDIX

Ion implanted polyaniline for radiation sensing applications

M Maloba[1], S J Moloi[1 (a)] and M Msimanga[2]
[1] University of South Africa, Department of Physics, Private Bag X 6, Florida, 1710, South Africa.
[2] Tshwane University of Technology, Department of Physics, Private Bag X 680, Pretoria 0001, South Africa.

Email: matomemiz@yahoo.com

Abstract: Polyaniline film was formed on an ITO/PET substrate using spin coater. The films were then implanted at cryogenic temperature with 20-keV Cu+ ions to a fluence of $5x10^{15}$ ions/cm2 to form Cu+-PANI nanocomposite material. Different material characterisation techniques were used to investigate the effect of implantation on the structural, optical and electrical properties of the films. It was observed that that a surface Plasmon absorption band for copper appeared around 502 nm, and this is an indication that Cu+ ions are present in the polymer matrix. Furthermore, the optical band gap was found to decreases from 3.08 to 1.32 eV due to implantation. Current-Voltage measurements confirmed that ion implantation led to a slight increase in electrical conductivity of the films. This data indicates that ion implantation can be used as an effective tool to alter electrical properties of polymers for fabrication of the devices for various applications such as radiation sensing.

1. Introduction

Polymers are classified as a special class of organic materials with an alternate single-double bond conjugation [1]. Examples of the mostly known polymers are polythiophene, polypyrrole, polyacetylene and polyaniline [2, 3]. Polymers offer special properties of interests when compared to other materials since are mechanically flexible and affordable and have controllable electrical and optical properties [4]. These polymers find widespread use in variety of applications such as light emitting diodes (LEDs), thin film transistors, corrosion resistance, electromagnetic shielding, batteries, and sensor technology [5, 6]. Among these polymers, polyaniline exhibits unique properties and is chemically and environmentally stable with good redox properties [7, 8]. Furthermore, when suitable dopants are used, polyaniline exhibits good electrical and optical properties and it is easier to prepare using techniques such as spin coating [9, 4].

In nature, polymers are poor conductors and are not being used for fabrication of detectors. In improving their conductivity, polymers are being doped inorganic metal oxides such as ZnO and positively charged

[1] Corresponding author: Tel.: +27 116709067

metal ions such as copper, silver and gold using various doping methods like in situ growth of nanoparticles (NPs) in a polymer matrix and ion implantation [10].

In this work, polyaniline was spun cast on an ITO/PET substrate to obtain polyaniline films. The films were then implanted with Cu+ ions to form Cu+-PANI nanocomposite material. Optical band gaps of both pure polyaniline and implanted polyaniline were calculated using UV-visible absorption spectroscopy. FTIR of the films was also recorded to study the effect of ion implantation on the structural properties of the films. Current-Voltage (*I-V*) characteristics of the films was studied in order to investigate the effects of implantation on the electrical properties of the films.

2. Experimental Details

Polyaniline films were deposited on a transparent ITO/PET substrate using spin coater (Smart coater 100). The details of the solution preparation and substrate cleaning have been explained elsewhere [11] and would be repeated here. The films were implanted at iThemba LBAS, Gauteng at cryogenic temperature with 20-keV Cu+ ions to a fluence of $5x10^{15}$ ions/cm^2. Fourier transformation infrared (FTIR) spectroscopy was performed in absorption mode using Vertex 70 Sample Compartment RT-DLaTGS. An optical absorption study was carried out using UV/VIS/NIR Spectrometer by Perkin Elmer Lambda 1050). *I-V* measurements were carried out using a Keithley 6487 picoammeter with a voltage source. The contacts were such that the anode was ITO and the cathode was top side of polyaniline. The measurements were performed at room temperature (300 K). The experiment set up was similar to that of Thebe *et al* [12] for niobium-doped silicon detectors.

3. Results and discussion

3.1 FTIR spectral analysis

FTIR spectra for both pure and ion implanted polyaniline are shown in figure 1. The measurements were carried out to study chemical structure and formation mechanism of new chemical bonding after ion implantation. It can be seen from the figure that wavenumber ranges from 390 to 2900 cm^{-1} under absorption mode. The results also indicate that the chemical structure of polyaniline is not changed after ion implantation. This is due to the temperature at which the Cu+ ions were introduced into the polyaniline matrix. The temperature was low to cause bond disruptions in the implanted polyaniline. There are two characteristic peaks at 2966 and 2905 cm^{-1} bands correspond N-H present in aromatic amines [13]. Peaks around 1456 and 1578 cm^{-1} are characteristic bands of C=C stretching vibration of quinoid and benzenoid ring, respectively [14]. The two absorption peaks indicated that the prepared polyaniline samples consisted of the amine and amine nitrogen unites in its polymer chains [15]. Peak at 1242 cm^{-1} may be assigned to C-N stretching modes of benzenoid ring [16]. Peak at 1119 cm^{-1} is assigned to C-N stretching, this is due to the charge delocalization over polymer backbone [17]. Peaks at around 793cm^{-1} and 503 cm^{-1} bands are related to C-H out-of-plane bending vibration in the 1, 4 disubstituted benzene ring [18] and C-H out-of-plane bending vibration [19], respectively. The main peaks conform to the PANI structure in the previous works reported by [20].

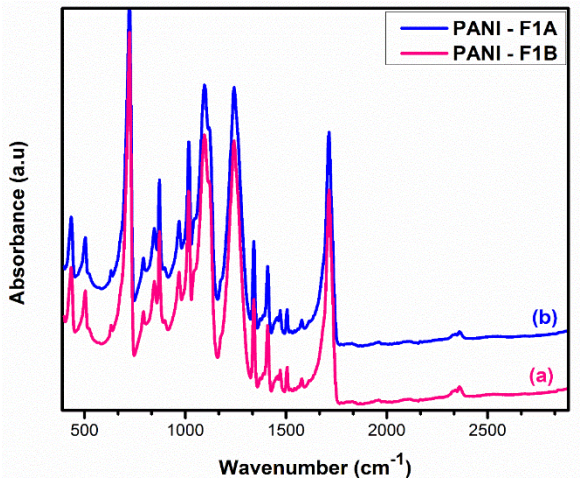

Figure 1*: FTIR spectra of unimplanted PANI (a) and Cu^{+} implanted PANI (b).*

3.2 UV-VIS spectral analysis

Figure 2 shows UV-Vis spectra of spin coated polyaniline on an IT/PET substrate. The wavelength ranged from 325 to 800 nm under absorption mode. Figure 2 (a) shows two characteristic absorption peaks of polyaniline. The first absorption peak around 333 nm is attributed to π-π* electron transition of benzenoid rings [21]. Peak around 616 nm is attributed to the excitation of an electron from highest occupied molecular orbital (HOMO) of benzenoid rings to the lowest unoccupied molecular orbital (LUMO) of the quinoid rings [22]. The implanted polyaniline (Fig. 2 (b)) shows two absorption peaks at around 460 and 590 nm, the two peaks almost combined to form one broad peak. This may be caused by the reduction in the energy bandgap/or the effect of implanted Cu+ ions on the conjugated structure of the conducting PANI [23; 24]. Furthermore, a sharp absorption peak appeared around 502 nm, which may be attributed to absorption band for copper. The formation of this new peak can be explained in terms of Surface Plasmon Resonance (SPR) which is related to the collective oscillation of conduction electrons in metal NPs in response to optical excitation [25].

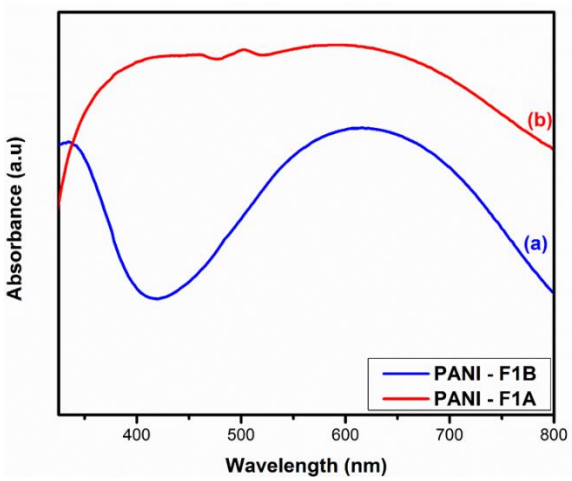

Figure 2*: UV-Vis spectra of unimplanted PANI (a) and Cu^{+} implanted PANI (b).*

For this study, indirect transition optical band gap of the spin coated polyaniline was estimated by plotting graph of absorption coefficient α) is against the incident photon energy (hv) which are related by Tauc relation [23] as:

$$(\alpha hv) = \left(hv - E_g\right)^n \quad (1)$$

where E_g is optical band gap and n denotes the nature of transition and n = ½ for direct allowed transition energy gap and n = 2 for indirect allowed transition energy gap [25]. The other parameters have usual meaning. E_g is estimated by extrapolating the straight-line portion of $(\alpha\, hv)^2$ vs (hv), where the graphs change the concavity. The intercept of the tangent to the x-axis gave the band gap of the films [23], as shown in figure 3.

The optical bad gap for pure polyaniline was found to be 3.08 eV, whereas implanted polyaniline exhibits a low band gap of 1.32 eV. Similar band gap value for spin coated pure polyaniline was reported by [26]. The reduction in the band gap for implanted polyaniline may be due to two reasons. First, the introduction of Cu+ ions into the polyaniline matrix may have extended the density of states of the polyaniline. As a result, the spectrum is shifted more into the visible region of the electromagnetic spectrum for implanted polyaniline as compared to that of pure polyaniline [25, 27]. This is because copper has a broad absorption band in the visible region of the electromagnetic spectrum [26]. Secondly, the introduction of Cu+ ions into the polyaniline matrix might have produced defect levels within the energy band gap [28] making the energy required to generate high charge carriers reduced. The generation of high number of charge carriers with low energy indicates that the resistivity of the material has reduced. This decrease of resistivity (increase of conductivity) is confirmed by current-voltage result presented in Section 3.3.

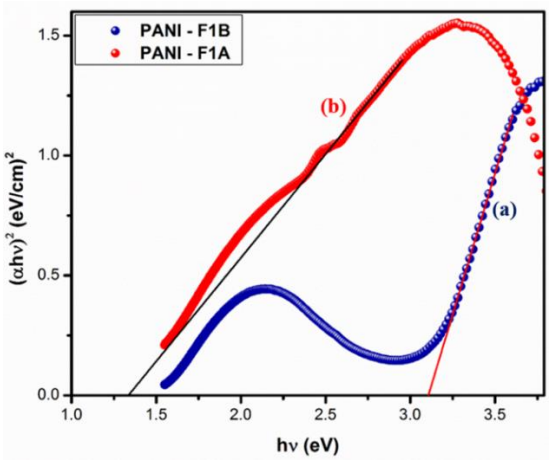

Figure 3: *UV-Vis spectra of unimplanted PANI (a) and Cu+ implanted PANI (b).*

3.2 Current-Voltage measurements analysis

Figure 4 shows *I-V* characteristics of unimplanted and implanted polyaniline. In both cases the trends are linear indicating an ohmic behaviour of the material. The current for the implanted material is found to be higher than that of unimplanted material in both voltage directions. An increase in current indicates that the resistivity (conductivity) of the material had decreased (increased) due to implantation. Thus, the voltage

(energy) required to pass considerable amount through the implanted material is less than that unimplanted material.

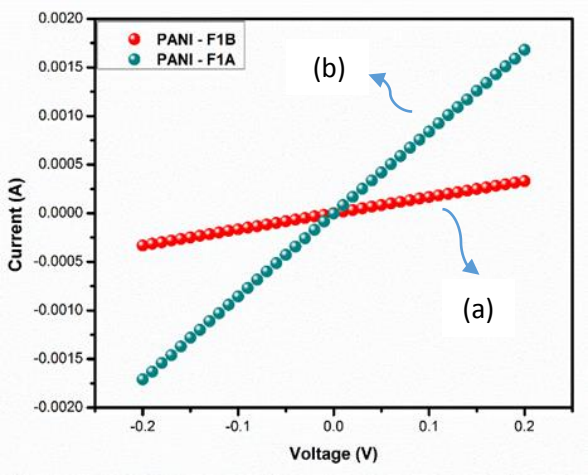

Figure 4*: Current-voltage characteristics of unimplanted PANI (a) and Cu+ implanted PANI (b).*

A decrease in resistivity indicates that the density of charge carriers has increased due to introduction of Cu^{+} in polyaniline matrix. Thus, in the energy gap of polyaniline copper generates defect levels that are responsible for the generation of carriers charge in the energy gap of polyaniline. This data complements that of UV-Vis measurements, both indicating that the energy required to generate considerable number of charge carriers to contribute to the measured current has decreased.

4. Conclusion

Polyaniline (EB) was successfully prepared on an ITO/PET substrate using a spin coater and this was confirmed by the characteristic chemical bonds that were observed on FTIR spectra. The results also indicate little bonding disruption in the pristine PANI molecular structure due to Cu^{+} implantation. It has, however shown that the implantation changes the crystal structure of the polyaniline resulting in a decrease in optical band gap of the polymer from 3.08 to 1.32 eV. A decrease in optical bang gap can be interpreted in terms of generation of charge carriers by copper induced defect levels in the energy gap of polyaniline. This generation of charge carrier is confirmed by a decrease (increase) in resistivity (conductivity) of polyaniline. A control of the conductivity indicates that electrical properties polyaniline can be tailored to be suitable for fabrication of electronic devices for various applications such as photo cells and radiation sensing.

We are currently preparing to irradiate unimplanted and Cu^{+} implanted polyaniline films with 1 MeV neutrons to establish resistant of the material to radiation.

Acknowledgments

The financial assistance of the National Research Foundation (NRF) of South Africa (Grant Number: 105292) towards this research is hereby acknowledged. Opinions expressed and conclusions arrived at, are those of the authors and are not necessarily to be attributed to the NRF.

References

[1] Kerileng M *et al*. 2012 *Int. J. Electrochem. Sci*. **7** 11859 – 11875.
[2] Gupta K *et al*. 2010 *Synthetic Metals* **160** 1566-1573.

[3] Liu Z et al. 2013 *Current Organic Chemistry* **17** 2256-2267.
[4] Farag A. A *et al*. 2010 *Synthetic Metals* **160** 156-161.
[5] Ates M. *et al*. 2012 *Current Physical Chemistry* **2** 224-240.
[6] Kumar F *et al*. 2010 *Synthetic Metals* **160** 1507-1512.
[7] Babu. *J. et al*. 2013 *Mater. Sci. Appl*. **4** 1-10.
[8] Saikia J P and Sarmah P C 2011 *Mater. Sci. Appl*. **2** 1022-1026.
[9] Li B et al. 2010 *J. poly Science: Part B: Polymer Physics* **48** 2072-2077.
[10] Kango S *et al*. 2013 *Review, Progress in Polymer Science* **38** 1232-1261.
[11] Maloba M. 2018 MSc Thesis, Univ. of South Africa (Johannesburg).
[12] Thebe M.J. Moloi S.J and Msimanga M 2015, *Electrical characterization of undoped and niobium-doped n-type silicon diodes* (Proc.: The 60th annual conf. of the South African Institute of Physics), Port Elizabeth, South Africa.
[13] Mark J E 1999 *Polymer Data Handbook*, 1st edition. (Oxford University Press, Inc.: New York).
[14] Beckerle P and Strobele H 2000 *Nucl. Instrum. Methods Phys. Res.* **449** 302.
[15] Zhang J 2007 *Appl. Surf. Sci.* **253** 5436-5441.
[16] Ratier B *et al*. 2000 *Synth. Met.* **115** 103-107.
[17] Zhang L J *et al*. 2004 **14** 693-698.
[18] Xu G H *et al*. 2013 *J. Colloid Interface Sci.* **411** 204-212.
[19] Sharma I D *et al*. 2013 *Indian J. Eng. Mater. Sci.* **20** 145-149.
[20] Zhang L J *et al*. 2003 *Adv. Funct. Mater*. **13** 815-820.
[21] Dong Y *et al*. 2007 *Nanotechnology* **18** 455603.
[22] Nur H *et al*. 2007 *Malaysian Polymer Journal* **2** 12-21.
[23] Mallick K *et al*. 2007 *J. Phys.: Condens. Matter* **19** 196225.
[24] Kaya M *et al*. 2007 *J. Phys.: Condens. Matter*. **19** 406205.
[25] Mu J *et al*. 2013 J. Power Sources **242** 797-802.
[26] Lu x *et al*. 2011 *Electrochima Acta* **56** 9224-9232.
[27] Kumar S A *et al*. 2012 *J. Mater. Sci*. **47** 246-2471.
[28] Mathai C J *et al.* 2002 *J. Phys. D: Appl.* 32 2206-2210.